Title
The shock response of periodically layered active and reactive composites

Author
Roberts, Christopher

Publication Date
2017

Peer reviewed|Thesis/dissertation

UNIVERSITY OF CALIFORNIA

Los Angeles

The shock response of periodically layered active and reactive composites

A dissertation submitted in partial satisfaction of the requirements for the degree
Doctor of Philosophy in Materials Science & Engineering

by

Christopher Charles Roberts

2017

ABSTRACT OF THE DISSERTATION

The shock response of periodically layered active and reactive composites

by

Christopher Charles Roberts

Doctor of Philosophy in Materials Science & Engineering

University of California, Los Angeles, 2017

Professor Christopher S. Lynch, Co-Chair

Professor Jenn-Ming Yang, Co-Chair

The propagation of shock waves through layered heterogeneous materials is fundamentally different than that of homogeneous materials. The shock front is reflected at the impedance-mismatched interfaces, creating multiple scattering events that alter the shock propagation characteristics. These effects can be utilized in shock mitigation systems, but are inherently passive. Incorporation of active materials such as piezoelectric/ferroelectric ceramics holds promise for tailoring the shock response of layered composites in real time. Mechanical energy from the shock wave is converted into electrical energy, which can then be propagated ahead of the shock front to power additional active or reactive layers.

This dissertation explores the shock response of active and reactive composites through a combination of experimental and computational work. High-strain rate testing of ferroelectric PZT 52/48 and 95/5 ceramics and periodically layered brass/ferroelectric composites were

performed using a load frame, split Hopkinson pressure bar, and flyer plate impact experiments. Computational modeling of these systems was performed using the multiphysics shock code ALEGRA-FE. Additionally, a laser-driven shock compression system was used in combination with electron microscopy to study the shock response of periodically layered aluminum/nickel reactive materials deposited onto copper nanopillars.

The computational results of this work indicate that the electromechanical coupling of piezo/ferroelectric materials and their composites hold promise in tuning their shock response in real time. However, the experimental results indicate that the shock response is dominated by impact conditions such as impact velocity and composite geometry. The electrical power released by the transient loading of PZT 52/48 and 95/5 was dependent on the loading rate, and the wave speed and rise time within periodically layered active composites was dominated by impact velocity. The laser-driven shock compression system enabled the microstructure of reactive material nanopillars to be studied pre- and post-shock loading. The results indicate that laser-driven shock compression initiated layer interdiffusion, a precursor to ignition. This suggests that the laser-driven shock compression system can serve as a high throughput, low cost test bed for reactive and energetic material systems and their composites.

This dissertation of Christopher Charles Roberts is approved.

Vijay Gupta

Jenn-Ming Yang, Committee Co-Chair

Christopher S. Lynch, Committee Co-Chair

University of California, Los Angeles

2017

This dissertation is dedicated to everyone who has lent me a helping hand along my journey.

To my parents, grandparents, aunts, uncles, teachers, advisors, and friends, thank you.

Without your support, none of this would have been possible.

I am very appreciative of my committee members, Prof. Vijay Gupta, Prof. Gregory Carman, Prof. Jenn-Ming Yang, and Prof. Christopher Lynch. It was a pleasure working under Prof. Lynch and collaborating with fellow lab mates in the Lynch, Carman, and Gupta laboratories. In addition, I'd like to thank Kit Neel for his help and expertise in shock physics.

Table of Contents

List of Figures and Tables

Acknowledgements

This research was supported under the Air Force Office of Scientific Research Center of Excellence: High-Rate Deformation Physics of Heterogeneous Materials. The work described in Chapters 2 and 4 with the ferroelectric modeling would not have been possible without the assistance of Sandia National Laboratories* under a No-Fee-Agreement, providing authorization to use the Sandia software ALEGRA and Sandia computing systems, along with helpful insight from Sharon Petney, Mike Wong, and Wen Dong. The split Hopkinson pressure bar experiments were performed at the California Institute of Technology with the assistance of Dipankar Ghosh and Thibaud Talon of Professor Radhakrishnan's research group. The plate impact experiments were performed at the Air Force Research Laboratory's High Pressure Particulate Physics Facility located at Eglin Air Force Base with the assistance from Christopher 'Kit' Neel, Warren 'Russ' Maines, and the rest of the HP3 facility. The load frame experiments were carried out at the Mechanical Engineering Department at the University of California, Los Angeles with assistance from John Domann. The laser-driven shock experiments were performed with assistance from Ryan Crum, Brian Ramirez, and Carlos Gamez.

Much of the experimental work in Chapter 3 was performed equally with Peng Lv, utilizing assistance with the split Hopkinson pressure bar from Dipankar Ghosh and Thibaud Talon, and with Professor Christopher Lynch as the principle investigator. Chapter 3 contains elements from the following publications:

C. C. Roberts *et al.,* "Intermediate strain rate energy harvesting from the impact of PZT 52/48 and 95/5," *J. Comp. Mater.*, vol. 49, pp. 1863 – 71, 2015.

* Sandia National Laboratories is a multi-mission laboratory managed and operated by National Technology and Engineering Solutions of Sandia, LLC., a wholly owned subsidiary of Honeywell International, Inc., for the U.S. Department of Energy's National Nuclear Security Administration under contract DE-NA0003525.

Vita

Christopher Charles Roberts

Education

2013 Master of Science, Materials Science & Engineering
University of California, Los Angeles

2010 Bachelor of Science, Physics
University of California, Santa Barbara

Experience

2013 – Present: Graduate Student Researcher at the Center for Multiferroic Materials & Systems
Mechanical Engineering, University of California, Los Angeles
Ferroelectrics, Reactive Materials, & Shock Mitigation

2012 – Present: Teaching Assistant for Multiple Departments
University of California, Los Angeles
Math, Mechanical Engineering, & Materials Science & Engineering

2014 – 2016: Technology Fellow at the Office of Intellectual Property
University of California, Los Angeles
Technology Transfer, Invention Assessment, & Marketing

2012 – 2014: Independent Consultant for Munger Tolles & Olsen LLP
Los Angeles, California
Technical Assessment & Drafting

2014: Visiting Research Scholar at the High Pressure Particulate Research Facility
AFRL/RW, Eglin Air Force Base, Florida
Plate Impact Experiments

2013: Visiting Research Scholar in the Amano Laboratory
Electrical Engineering, Nagoya University, Japan
Gallium Nitride LEDs

2011-2013: Graduate Student Researcher in the Electronic Materials Group
Materials Science & Engineering, University of California, Los Angeles
Wafer Bonding, X-ray Diffraction, Transmission Electron Microscopy

2009-2011: Undergraduate Student Researcher, Computational Materials Group
Materials Science, University of California, Santa Barbara
Optoelectronic Device Simulations

Publications

C. C. Roberts, P. Lv, D. Ghosh, T. Talon, and C. S. Lynch, "Intermediate strain rate energy harvesting from the impact of PZT 52/48 and 95/5," *J. of Comp. Mater.*, vol. 49, pp. 1863 - 1871 2015.

B. Beekley, C. C. Roberts, M. S. Salazar and M. S. Goorsky, "Large Area Plan-View Transmission Electron Microscopy Sample Preparation for Direct-Bonded Interfaces," *ECS Trans.*, vol. 64, pp. 161-166, 2014.

K. Yeung, J. Mc Kay, C. C. Roberts and M. S. Goorsky, "Electrical Conductivity of Direct Wafer-Bonded GaAs/GaAs Structures for Wafer-Bonded Tandem Solar Cells," *ECS Trans.*, vol. 50, pp. 99-108, 2013.

C. C. Roberts, Q. Yan, M. Miao, and C. G. Van de Walle, "Confinement effects on valence-subband character and polarization anisotropy in (11$\underline{2}$2) semipolar InGaN/GaN quantum wells," *J. Appl. Phys.*, vol. 111, pp. 073113, 2012.

Presentations

C. C. Roberts, P. Lv, and C. S. Lynch, "The potential for smart materials for shock mitigating systems," Gordon Research Conference, Ventura, CA, Jan. 1 - Feb. 5, 2016.

C. C. Roberts, P. Lv, and C. S. Lynch, "Altering shock response using active metamaterials," International Materials Research Conference, Cancun MX, Aug. 17-21, 2015.

1 Introduction

1.1 Shock Mitigating Systems

Shock mitigation is important to many fields. In civil engineering, shock absorbers and isolation strategies have been employed to reduce repetitive pounding that buildings and bridges are often subjected to during earthquakes.[1] In manufacturing, impact welding utilizes the extreme heat and pressure induced during shock impact to weld materials or create entirely new phases.[2] The most obvious applications of shock mitigation are related to the defense industry, where blast mitigation of persons, vehicles, and structures are of the utmost importance. The shock wave that accompanies the impact of a projectile or the blast from explosive devices can often be more dangerous than the projectile/shrapnel that accompanies it. Shock wave-induced tissue damage can lead to hemorrhaging, edema, and pseudoaneurisms.[3] Mitigation techniques have often produced unexpected and sometimes unwanted results. For example, early research into a shock mitigation system incorporated a low impedance foam on the outside of a higher impedance armor layer, however the wave reflection dynamics resulted in a shock enhancement on the protected side.[4] During the 1980's, after considerable shock studies undertaken by groups such as Sandia National Laboratories, the concept of impact engineering was coined and significant interest into shock mitigating systems was established with the first International Symposium on Impact Engineering in 1992.[5] Since then, a variety of techniques to mitigate shock damage have been investigated The high-rate deformation physics of heterogeneous and smart material systems have recently been of particular interest.

1.2 Shock Response of Piezoelectric and Ferroelectric Materials

The ferroelectric ceramic lead zirconate titanate (PZT) under shock loading has been investigated extensively since the 1950's due to its role in pulsed power devices.[6] Once poled,

these ceramics exhibit piezoelectric and ferroelectric behavior. Under axial shock compression, their polarization reorients and the surface charge that is initially trapped on the poling electrodes is released. There are two popular compositions of ceramic PZT based on the zirconium/titanium ratio; PZT 52/48 and PZT 95/5. Many characteristics, including the crystal structure, dielectric response, and piezoelectric response, are a direct result of the zirconate/titanate ratio. PZT 52/48 resides on the morphotropic phase boundary,[7] where many of the electromechanical properties are enhanced. PZT 95/5 lies on a phase boundary between a ferroelectric (FE) phase and an antiferroelectric (AFE) phase, allowing for a pressure-induced FE to AFE phase transition.[8]

The effect of the electrical boundary conditions on the shock response of PZT 52/48 has been minimally investigated. For a common commercial type of PZT 52/48 (PZT-5A), the elastic modulus reduces from 147 GPa to 111 GPa simply by shunting the two electrodes.[9] When a shock wave is traversing a shunted ferroelectric, secondary tensile stresses develop in the yet-unshocked region due to piezoelectric effects.[10-12] At higher pressures, the shock compression reorients the domains within the ferroelectric. Mock & Holt noticed a significant difference in transmitted shock wave structure and depoling currents when altering the electrical boundary conditions across shock-compressed PZT 56/44 (a similar composition to PZT 52/48).[13] They attributed the driving force for these differences to the internal electric fields, with higher fields acting to hold the domains in their original orientation.

For systems close to the FE-AFE phase boundary, such as PZT 95/5, shock depoling primarily occurs due to phase transformation from the ferroelectric rhombohedral phase to the antiferroelectric orthorhombic phase.[8] This FE-AFE phase transformation occurs around 330 MPa under hydrostatic compression,[14] and starts at pressures above 500 - 600 MPa[15] for uniaxial shock compression. There have been few efforts into elucidating the effect of the electrical boundary

conditions on the shock response of PZT 95/5. Dick and Vorthman reported a 12% reduction in final particle velocity in shock loaded, normally poled PZT 95/5 under high field conditions.[16] They suggested that the presence of an electric field could hinder the phase transformation by the enforcing long-range ferroelectric order. Dai et al. also saw a change in transformation pressure for various shock-compressed PZT 95/5 samples under varying electrical boundary conditions and came up with a linear model relating the transformation pressure to the internal electric field.[17] Jiang et al. reported on the suppressive effect of the self-generated electric field on the phase transformation under shock compression and provided an explanation from the perspective of soft mode theory.[18]

Despite the lack of direct research involving altering the shock propagation behavior in PZT 95/5 through electrical means, considerable work has gone into characterizing the shock response and depolarization. Early studies such as those of Linde[19] and Doran[20] demonstrated the capability of poled ferroelectric materials to generate a large pulse of current and voltage if abruptly depoled by shock loading. Halpin[12,21] examined the combined effect of stress on remnant polarization, polarizability and conductivity and provided a model to describe the current output including the effect of conductivity. Lysne[8,22] explored electric energy generation and the dielectric properties of PZT 95/5 through normal mode depoling. Dick and Vorthman[16] continued with studies of normal mode shock depoling by varying the initial electric state of the ferroelectric phase and presented the effect on the mechanical and electrical response of PZT 95/5. Mock and Holt[13] used gas-gun impact techniques to pulse charge nanofarad capacitors from shock depoling of PZT 95/5 and PZT 56/44 ferroelectric ceramics. Chhabildas[23] obtained a good dynamic mechanical description of the shock response of PZT 95/5 ferroelectric ceramic. By using a gas gun and velocity interferometry techniques, the shock loading and unloading, and the pressure-shear response were determined up to 4.6 GPa. Results indicated that the unpoled

samples undergo a phase transformation at 0.5 GPa and stay in a mixed phase over the stress region 0.9 to 2.6 GPa, with the concentration of the FE phase diminishing with increasing stress. The kinetics of pore compaction and crush-up behavior dominate the mechanical material response above 2.6 GPa, resulting in a three-wave structure.

An extensive experimental study was initiated by Setchell et al.[24] in conjunction with efforts to improve available models for the response under shock loading. Zeuch et al.[25] conducted uniaxial shock compression experiments on PZT 95/5 to provide the evidence for an orientation-dependent criterion for onset of the phase transformation. The effects of phase transformations in PZT 95/5 under combined loadings of hydrostatic and triaxial compression stresses were also investigated by Zeuch et al.[26] This led to the observation that the hydrostatic stress required for phase transformation decreased as triaxial compression increased. Zeuch et al.[27] continued the research on PZT 95/5 to quantify the effect of nonhydrostatic stress and electric field bias on the electromechanical behavior during phase transformation. More recently, Valadez et al.[14] experimentally investigated the coupled effects of hydrostatic pressure and electric field on the phase transition in PZT 95/5.

Sandia National Laboratories made significant progress into the insight of the shock response of PZT 95/5 by using plate impact experiments. Furnish et al.[15] characterized axially poled PZT 95/5 to investigate the dynamic electromechanical behavior. Furnish et al.[28] characterized unpoled samples of PZT 95/5 using plate impact and compared them with the mechanical response of poled samples. Setchell et al.[29,30] varied the resistance of the external circuit across normally poled samples of PZT 95/5 to examine the shock response as a function of the peak electrical field generated in the sample. In addition, they measured the Hugoniot states to examine the constitutive mechanical[31] and dielectric properties[32] during shock propagation. They also investigated the depoling characteristics[33] and the effects of porosity on the

electromechanical response.[34-36] This research serves as a foundation for analyzing the shock response of PZT 95/5.

1.3 Shock Mitigation Utilizing Impedance-Mismatched Layered Composites

With the advent of acoustic metamaterials and phononic crystals, some researchers have proposed engineering novel heterogeneous materials that do not support shock propagation.[37] One such promising material is a periodically layered composite consisting of highly impedance-mismatched constituents. Zhuang et al. characterized periodically layered soft/hard composites via shock loading using a 36 mm powder gun. The soft layer consisted of polycarbonate, while the hard layer consisted of glass, steel or aluminum. The impedance-mismatched interfaces caused the shock front to reflect or 'scatter' multiple times, reducing the wave speed and spreading the shock front.[38] They found that the shock front strain rate increased with the square shock stress, compared to the fourth power as seen in most homogeneous materials. This increase in effective shock viscosity was found to increase with interface impedance mismatch, and decrease with larger interface density and loading amplitude. The periodic layered structure also resulted in an oscillatory late-time shock profile, possibly contributing to shock energy dissipation.

An analytical solution to shock loading heterogeneous composites was derived by Chen et al. using Floquet's theory of ordinary differential equations with periodic coefficients.[39] They found that the mean stress decreased with time, attributed to some time-dependent dissipation mechanism.[40] An increase in impedance mismatch was found to increase the rise time, increase the late-time oscillations, lower the effective wave speed, and lower the oscillation frequency. Increasing interface density was found to lower rise time, increase oscillation frequency, and resulted in a higher peak stress.

Tsai & Prakash also provided an analytical solution for elastic-elastic systems and elastic-viscoelastic systems.[41] They performed plate impact experiments on aluminum-polycarbonate and iron-titanium composites and compared their analytical solutions to experimental results. They found that increasing the impedance-mismatch between layers resulted in a reduction of the elastic precursor wave amplitude and a reduction in the wave speed. The wave front was also spread with increasing impedance mismatch.

Additional work regarding the shock response of heterogeneous composites motivated Volger to investigate the scaling of shock waves in heterogeneous materials.[42] Swegle and Grady observed a relationship between the strain rate and stress amplitude in homogeneous materials, $\delta\varepsilon/\delta t = S\sigma^4$, now known in the shock literature as the fourth power law.[43] Here S is a material parameter that describes the material's effective shock viscosity. One of the main results from Zhuang's work was an apparent break from the fourth power law, where the relationship followed more closely to a second power law, $\delta\varepsilon/\delta t \propto \sigma^2$. Volger used equation 1.1 to find the strain rate within the layered composites based on the strain ε, density ρ_0, particle velocity u_p, stress σ, and change in time Δt. He varied layer thicknesses and material combinations to find strain rate/stress amplitude relationships with varying exponent coefficients from 1.0-2.4.

$$\dot{\varepsilon} = \frac{\rho_0 u_p^2}{\sigma \Delta t} \qquad \text{(Eq. 1.1)}$$

In each of the aforementioned studies on shock propagation in layered composites, the impedance-mismatch ratio was a key factor in increasing the effective shock viscosity. For shock waves, there exists a shock impedance, Z_{shock}, which is a product of the density ρ and shock wave speed U_S (Eq. 1.2). However, the acoustic impedance, Z, can be used to approximate the impedance mismatch (Eq. 1.3). The acoustic impedance is a product of the density and

longitudinal acoustic wave speed, C_L, which itself can be written in terms of the elastic modulus and the density.

$$Z_{shock} = \rho|U_S| \quad \text{(Eq. 1.2)}$$

$$Z = \rho C_L \quad \text{(Eq. 1.3)}$$

Once the impedances are known the transmission (T) and reflection (R) coefficients can be computed using equations 1.4 & 1.5 to find the amplitude of the transmitted and reflected waves in relation to the incident wave.

$$T = \frac{2Z_2}{(Z_2 + Z_1)} \quad \text{(Eq. 1.4)}$$

$$R = \frac{(Z_2 - Z_1)}{(Z_2 + Z_1)} \quad \text{(Eq. 1.5)}$$

The transmitted and reflected wave fronts interact with themselves as well as the impedance-mismatched interfaces. Thus, increasing the impedance-mismatch ratio increases the wave scattering of the shock front, more effectively spreading the front and dissipating the shock energy.

1.4 Proposed Active Composite

The premise of this research was to investigate what effects, if any, incorporating active layers of ferroelectric ceramic into impedance-mismatched composites has on the shock mitigation behavior. A number of benefits may arise from incorporating such layers. Electrical power can be released from an initial shock-depoled ferroelectric layer and then transferred ahead of the shock front in order to power subsequent layers. The electromechanical behavior of the ferroelectric layers may enhance some of the shock mitigating mechanisms described in section 1.3. The electrical boundary conditions across the ferroelectric layers may alter the shock

impedance-mismatch between layers and thus influence the wave scattering within the composite. To investigate these effects, a composite of brass and PZT was constructed and characterized under high strain rate loading and various electrical load resistances. Prior to the high strain rate composite testing, material characterization of two common compositions of PZT (52/48 and 95/5) was performed under low and intermediate strain rates in order to identify any strain rate dependence. This was done to ensure that a composition with low rate dependence was chosen for the ferroelectric layer of the composite, so that any changes in shock response could be better attributed to the electrical boundary conditions. Additionally, computational simulations using a multiphysics shock hydrocode were performed to elucidate the effects of piezoelectricity on the shock response. The experimental loading methods include uniaxial loading via load frame, split Hopkinson pressure bar, and plate impact from a single stage gas gun. The characterization methods include electrical monitoring of the ferroelectric and velocimetry measurements via both the velocity interferometer system for any reflector (VISAR) and photon Doppler velocimetry (PDV).

1.5 Experimental Methods

1.5.1 Load Frame

For electromechanical characterization under uniaxial, low loading rate compression, an MTS biaxial load frame was utilized in conjunction with a megahertz oscilloscope. An alignment fixture was used to ensure uniaxial compression, and the ferroelectric samples were insulated from the rest of the load frame using Kapton tape. A current viewing resistor monitored the voltage across the ferroelectric samples.

To ensure that the driving signal for compression produced the appropriate response, the load frame was tuned using the suggested procedure from the manufacturer's website.[44] The

ultimate goal of tuning is to reduce the error signal between input command and output response. Usually, the load frame is run with a square wave at the frequency that the experiments will be carried out at. The waveform is then compared between command and output. The first property to tune is the proportional gain (P). It amplifies the error signal by an appropriate amount through altering the power output, and can be described as the acceleration of the servo loop. Increasing the gain increases the input to the servovalve, moving more oil into the actuator. However, too much gain can result in the system becoming unstable. The next property to tune is the integral gain (I). Integral gain is the integral of the error signal over time, such that small errors become apparent. The result is that integral gain boosts the low frequency response of the servovalve command. For these reasons, integral gain is sometimes called reset gain. Too much integral gain can result in oscillations in the system. Derivative gain (D) reduces the error signal when its rate of change is the greatest, reducing overshoot and ringing. Too much derivative gain can cause instability at high frequencies, while too little can result in a rumbling sound. The final tuning property is the feed forward gain (F). This property analyses the command summing function, and returns the derivative of the command. The faster a command is changing, the more the feed forward gain responds.

1.5.2 Split-Hopkinson Pressure Bar

The Kolsky bar, or split Hopkinson pressure bar (SHPB), is an experimental apparatus for material characterization under strain rates in the range of 10^2-10^3/s.[46] The device is comprised of three bars; a 'striker' bar, an 'input' or 'incident' bar, and an 'output' or 'transmitted' bar. The bars are comprised of a material that remains elastic throughout the experiment, even though the sample may undergo significant plastic deformation. The sample is placed between the input and output bars, and the striker bar sends a stress pulse down the system whose duration is

determined by the striker bar's length. Strain gauges on the input bar record the incident and reflected pulses, while gauges on the output bar record the transmitted pulse. The shape of the incident pulse can be altered using pulse shapers between the striker bar and input bar. The nominal stress σ within the sample can be estimated by the transmitted strain ε_T, the elastic modulus of the bar material E_B, and the ratio of the bar and sample cross sectional areas A_B/A_S (Eq. 1.6).[45]

$$\sigma(t) = \frac{E_B A_B}{A_S} \varepsilon_T(t) \qquad \text{(Eq. 1.6)}$$

The nominal strain rate $\delta\varepsilon/\delta t$ and nominal strain ε can be found using the bar's wave speed c_B, the sample thickness l_0, and the reflected strain ε_R (Eq. 1.7 & 1.8). [45]

$$\dot{e}(t) = -\frac{2c_B}{l_0} \varepsilon_R(t) \qquad \text{(Eq. 1.7)}$$

$$\varepsilon(t) = \int_0^\tau \dot{\varepsilon}(\tau) d\tau \qquad \text{(Eq. 1.8)}$$

There are some basic requirements for performing valid SHPB experiments. In order for the calculated stress to be accurate, the stress must have the opportunity to equilibrate within the sample. This is achieved by ensuring the loading time is long compared to the characteristic time of the sample $t_S=c_S/l_0$, where c_S is the wave speed within the sample and l_0 is the sample thickness. Friction effects at the sample/bar interface can result in clamping which invalidates the uniaxial stress assumption. Keeping the sample thickness/diameter ratio small reduces this effect. In addition, lubricant can be used between sample and bar to allow for radial expansion. Dispersion effects must be taken into account when shorter stress pulses are used due to their higher frequency components. Pulse shapers placed between the striker bar and input bar elongate the stress pulse and reduce dispersion effects.[46]

1.5.3 Plate Impact Experiments

For high strain rate testing, plate impact experiments are used. Plate impact consists of launching flyer plate down a large diameter (typically 30-100 mm) gun barrel towards a stationary target plate. Single and two stage gas guns usually facilitate the launch, however powder guns can also be used. The impact event sends a shock wave into the target plate, creating a state of uniaxial compression. This strain state persists until release waves from the free surfaces arrive. The state of the material ahead and behind the shock front can be found in accordance with the Rankine-Hugoniot jump conditions. These conditions use the density ρ, shock wave speed U_S, particle velocity u_p, stress σ, energy E, and specific volume v to describe the conservation of mass (Eq. 1.9), momentum (Eq. 1.10), and energy (Eq. 1.11).[47]

$$\rho_0 U_S = \rho_1 (U_S - u_p) \qquad \text{(Eq. 1.9)}$$

$$\sigma_1 - \sigma_0 = \rho_0 U_S u_p \qquad \text{(Eq. 1.10)}$$

$$E_1 - E_0 = \tfrac{1}{2}(\sigma_1 + \sigma_0) \cdot (v_0 - v_1) \qquad \text{(Eq. 1.11)}$$

Here the subscript '0' describes the state of the material ahead of the shock, while the subscript '1' denotes the state of the material behind the shock front. In typical plate impact experiments, the target plate usually incorporates pins and sensors to capture the impact speed and tilt of the flyer plate with respect to the target. The normal and transverse stress states within the material can be captured using manganin, PVDF, or carbon stress gauges. The particle history of the back surface of the target is usually captured using laser interferometry.

The shock response of a material can be described by the material's Hugoniot curve, which represents the locus of all possible final states of shock compression. Hugoniot curves can be used to estimate the state of pressure and particle velocity within a material subjected to shock loading. Figure 1.1 shows the Hugoniot curves for a brass/brass symmetric impact event.

The Hugoniot with the negative slope represents the brass impactor. Initially it is in a state of zero pressure and an initial particle velocity equal to the impact velocity of 100 m/s. The Hugoniot with the positive slope represents the stationary brass target. Its initial state is one of zero pressure and zero particle velocity. Upon impact, the pressure at the brass/brass interface must be equal, and since the Hugoniot curves represent all possible final states of a shock event, both materials must be in a final state of ~1.7 GPa pressure and 50 m/s particle velocity. This method of predicting the shock state between multiple interacting materials is known as the impedance matching technique.[48]

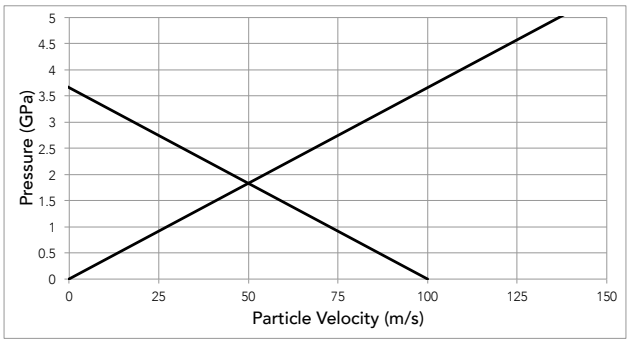

Figure 1.1: Hugoniot curves for brass utilized to predict the pressure and particle velocity in a symmetric impact event. The Hugoniot with the negative slope represents a brass impactor with initial impact velocity of 100 m/s, while the Hugoniot with the positive slope represents a stationary brass target.

1.5.4 Velocity Interferometer System for Any Reflector (VISAR)

The velocity interferometer system for any reflector (VISAR) is based on the design of a wide-angle Michelson interferometer (WAMI) and was developed at Sandia National Laboratories for the purpose of measuring the particle velocity in shock compression experiments. Two parameters are needed to obtain a material's Hugoniot equation of state, and the two that are usually measured are pressure and particle velocity. Prior to VISAR, particle velocity was measured using shorting pins of various lengths at the back free surface of the impacted sample.[49] While this method, developed by Los Alamos in the 50's, provides an average particle

velocity for the shock wave, it lacks any information about the structure of the shock front. The advent of affordable laser systems in the 1960's enabled the laser driven Michelson displacement interferometer. A laser beam is split using a beam splitter, where one arm is reflected off a mirror and the other reflected off the polished back of the displaced specimen. The two beams are then recombined. As the phase between the two beams is shifted due to the change in travel length of the specimen arm, a beating pattern can be seen in a bulls-eye shape, where the creating of new rings or fringes can be counted and the displacement calculated from the light wavelength.

The laser displacement interferometer was limited in its use for shock studies due to limitations in frequency processing. Shock impact velocities of just 300 m/s would produce fringe frequencies in the GHz range, which were difficult to record at the time of development. To mitigate this limitation, the team at Sandia split the Doppler-shifted light and ran one beam through a delay leg of a few nanoseconds. Using this technique, the fringe frequency becomes proportional to the velocity. In this arrangement, the VISAR became an optical differentiator of distance with respect to time, $\Delta x/\Delta t$, where Δt is the time delay of the delay leg. This arrangement had the additional benefit of moving the interferometer out of the line of sight for the impact experiment, allowing velocity interferometers to be reused. However, the initial velocity interferometer had poor resolution and could not distinguish acceleration from deceleration. In addition, the measured surface still needed to have a mirror finish to deliver enough optical intensity to make measurements. However, the WAMI configuration would alleviate most of these issues.

The WAMI configuration relaxed the mirror finish restriction on the specimen surface, allowing for 'any reflector' surface to yield a measurement. The WAMI uses an uncompensated dielectric in one leg of the interferometer ensuring uniform illumination of the detectors. Additionally, by shifting the phase of one of the beams by 90°, acceleration and deceleration

could be easily distinguished. Two final refinements were needed for calculating accurate particle velocity. One was accounting for the change of the index of refraction with wavelength within the glass etalon used in the delay leg. Even though the Doppler-shift in wavelength was very small, it was enough to shift the phase within the etalon. The other was accounting for the change of refractive index of the back window plate. Back window plates are used to investigate the particle velocity of a material without subjecting it to immediate release waves, as one does in free surface plate impact experiments.

Conventional VISAR interferometers are essentially two WAMI systems operating on different polarizations of light. The input beam is split using a beam splitter and sent down two different legs of the interferometer, as well as to the input beam intensity monitor. One leg of the interferometer is reflected off a mirror of known optical distance, while the other is sent through a glass etalon and to the specimen surface. The initially unpolarized light reflected off the specimen is split into two output signals using a polarizing beam splitter and read by a pair of detectors. A 1/8 wave plate phase shifts the two polarizations with respect to each other.

Computer analysis enables the counting of fringes to be accurate to at least 0.02% of a fringe.[50] The number of fringes is then multiplied by the interferometer's velocity-per-fringe (VPF) constant to get the velocity history. The VPF depends on the delay time of the etalon and wavelength of light. This leads to the velocity, v(t) given in equation 1.12, where λ is the wavelength of light, τ is the delay time, and F(t) is the fringe count. Only two fringes are needed in an experiment to obtain 1% accuracy in velocity.[50] The detector signals D1 and D2 are given by equations 1.13 & 1.14.

$$v(t) = \lambda/2\tau \cdot F(t) \quad \text{(Eq. 1.12)}$$

$$D_1(t) = a_{11}^2 I_0(t-t_1) + a_{21}^2 I_0(t-t_2) + 2a_{11}a_{21}\sqrt{I_c(t-t_1)I_c(t-t_2)}\cos\Phi_1(t) \quad \text{(Eq. 1.13)}$$

$$D_2(t) = a_{12}^2 I_0(t-t_1) + a_{22}^2 I_0(t-t_2) + 2a_{12}a_{22}\sqrt{I_c(t-t_1)I_c(t-t_2)}\cos\Phi_2(t) \quad \text{(Eq. 1.14)}$$

Here a_{ij} refer to the light polarization j passing through leg i. I_0 is the original intensity of the beam as monitored by the beam intensity monitor, and I_c is the intensity of the coherent light. The transit time for the j^{th} leg is given by t_j. Φ_1 is the phase difference between the light passing through each leg of the interferometer, and Φ_2 is the phase difference function that accounts for the round-trip passage through the 1/8 wave plate. The difference between each polarization, once it passes through the 1/8 wave plate, is given by equation 1.15.

$$\Phi_2(t) = [\phi(t-t2) - \beta] - \phi(t-t1) = \Phi(t) - \beta \quad \text{(Eq. 1.15)}$$

Here β is the relative phase delay and is controlled by rotating the 1/8 wave plate about its axis. When $\beta=\pi/2$, the two detector signals are said to be in perfect quadrature. It's useful to express β in terms of quadrature error, q, shown in equation 1.16. The beam intensity monitor is not exposed to any interference and its signal is given in equation 1.17.

$$\Phi_2(t) = \Phi(t) - \pi/2 - q \quad \text{(Eq. 1.16)}$$

$$D_{BIM}(t) = a_3^2 I_0(t-t_3) \quad \text{(Eq. 1.17)}$$

Here a_3 and t_3 are the coupling factor and transit time for the beam intensity monitor's optical path. If the light intensity varies slowly with regards to the time scales t_1, t_2, and t_3, the expressions $I_0(t-t_j)$ can be replaced with $I_0(t)$. Now the detector signals can be normalized by the beam intensity monitor signal (Eq. 1.18 & 1.19).

$$D_x = \frac{D_1(t)}{D_{BIM}(t)} = \underbrace{\bar{a}_{11}^2 + \bar{a}_{21}^2}_{x_0} + \underbrace{2\bar{a}_{11}\bar{a}_{21}\, I_c(t)/I_0(t)}_{A_x(t)}\cos\Phi_1(t) \quad \text{(Eq.1.18)}$$

$$D_y = \frac{D_2(t)}{D_{BIM}(t)} = \underbrace{\bar{a}_{12}^2 + \bar{a}_{22}^2}_{y_0} + \underbrace{2\bar{a}_{12}\bar{a}_{22}\, I_c(t)/I_0(t)}_{A_y(t)} \sin(\Phi_1(t) - q) \qquad \text{(Eq. 1.19)}$$

Here the barred ā variables represent the ratio of the interferometer coupling factors to the beam intensity monitor coupling factor; $\bar{a}_{ij}=a_{ij}/a_3$. The normalized signals D_x and D_y parametrically define a family of ellipses. When I_c/I_0 is constant, the interferometer output falls upon a single ellipse. Each normalized signal has two components, a constant offset x_0 (y_0) and a time-varying function $A_{x,y}(t)$. An ideal ellipse centered at the point (1,1) would have a signal amplitude of unity ($I_c/I_0=1$), however in practice the contrast is less than unity and the ellipse is slightly off center. The quadrature error q leads to non-circular ellipses.

Since the VISAR system only measures the optical phase difference, calculating the apparent velocity was usually done using the VISAR approximation or the more general inverse analysis,[51] where conventional VISAR data analysis software incorporates both of these equations as well as additional numerical techniques. Additional velocity corrections are needed because different types of motions can alter the phase shift of the beams in the same manner. Angular illumination and reflection must be accounted for, as well as window corrections.

The VISAR system can be characterized by the delay time, the ellipse parameters, the dynamic contrast, and the precision limits. The delay time, dictated by the etalon in the delay leg of the interferometer, must be slightly adjusted to account for dispersion effects due to the Doppler-shifting of the light. The ellipse parameters define the trace of the ellipse parameterized by the quadrature signals D_x and D_y. The ellipse is determined by the phase difference of the two signals and should ideally trace a circle of radius 1 centered on 1,1. Typically, incoherency in the light beam and quadrature error produce a less than ideal ellipse, and ellipse fitting or parameter constraining must be used to identify the ellipse parameters. Dynamic contrast describes the

change of contrast during the experiment, such as a loss of contrast of coherent light, or multiphase interference. The radius of the ellipse is related to dynamic contrast and equal to it when q=0 and D_x=D_y. Precision limitations include fringe ambiguity and fringe uncertainty. Fringe ambiguity arises due to the fact that adding 2π to the phase difference yields the same signal. When contrast is maintained during an experiment, this is not a problem, as the ellipses are traced out and easy to follow. However, if contrast is lost as the VISAR traces the ellipse, it is an indication that fringes need to be added, but it can be unclear how many are necessary. There are a number of logical means that can be applied to estimate the number of fringes to add, including considering velocity limitations or using two VISAR systems.

1.5.5 Photon Doppler Velocimetry (PDV)

VISAR measurements are made by splitting Doppler-shifted light, sending one beam down a delay leg, and recombining the light to obtain interference fringes. Photon Doppler Velocimetry (PDV) combines unshifted light with Doppler shifted light to form a beat frequency proportional to the target velocity. A PDV system is essentially a fast Michelson interferometer, whose ability to measure such fast changes in fringes was enabled by the recent advances in gigahertz sampling. The relationship between apparent velocity v and signal frequency f is given by equation 1.20, where the source wavelength λ is typically centered around 1550 nm.[52] The velocity resolution is determined through the uncertainty principle in equation 1.21, which describes how well the frequency can be resolved over a time period t.

$$v = \frac{\lambda}{2} f \qquad \text{(Eq. 1.20)}$$

$$\Delta f \cdot t \geq \frac{1}{4\pi} \qquad \text{(Eq. 1.21)}$$

This corresponds to an uncertainty of 62 m/s for a time period of 1 ns, which highlights the necessity for gigahertz sampling capability.[52] Comparison of PDV to VISAR and velocity pin data suggests that PDV can reduce velocity uncertainty to lower than 0.1%.[53] Traditional PDV systems can have difficulty following rapid, low velocity changes. In these situations, optically upshifted PDV systems can be used to increase the frequency baseline.

1.6. Thesis Organization and Significant Results

In this thesis, experimental and computational research into the linear and nonlinear electromechanical response of ferroelectric composites is presented. Chapter 1 presents the research motivation for utilizing ferroelectric layered composites for shock mitigation, in addition to highlighting the working principles of the experimental procedures.

Chapter 2 presents the multiphysics modeling performed using the shock hydrocode ALEGRA-FE.[54] This research investigated the piezoelectric response of ferroelectric composites under shock loading. The results show that the stress state within the composite can be tuned in real time by controlling the electrical boundary conditions across the ferroelectric layers. Ferroelectrics that have been electrically shunted can transfer the mechanical shock energy ahead of the shock to induce tensile stress and negative particle velocities in the yet-unshocked region of the ferroelectric. This is accomplished by converting the mechanical energy within the shocked region of the ferroelectric into electrical energy via the piezoelectric effect, transferring the electrical energy ahead of the shock front to the yet-unshocked region of the ferroelectric, and then transforming the electrical energy back into mechanical energy to mitigate the shock stress. The stress state can be altered by as much as 20%, assuming the behavior stays within the piezoelectric regime. The stress levels can be altered locally and nearly instantaneously.

Chapter 3 presents the nonlinear electromechanical response of PZT under higher amplitude transient waves. Experimental mechanical depolarization studies of both PZT 52/48 and 95/5 have been undertaken in the low- to intermediate-loading rate regime. The results indicate no discernable loading rate dependence for loading rates on the order of MPa/ms for either PZT 52/48 or PZT 95/5. However, PZT 52/48 exhibits a spread in the rate of depolarization at loading rates within the MPa/μs regime. The depolarization of PZT 95/5 was found to be significantly less loading-rate dependent within this intermediate loading rate regime. Given the minimal loading rate dependence of PZT 95/5, as well as the evidence of active control of shock propagation via the electrical boundary conditions available in the literature, PZT 95/5 was chosen as the ferroelectric component of the proposed ferroelectric composite.

Chapter 4 presents the experimental and computational results of a ferroelectric composite shock loaded via plate impact. Multilayered composites consisting of brass and PZT 95/5 were fabricated and then characterized via plate impact experiments using a 100 mm bore single stage gas gun. The electrical boundary conditions were controlled via load resistances in series with the ferroelectric layers. Both VISAR and PDV were utilized to obtain the free surface particle velocity. Gigahertz oscilloscopes captured the ferroelectric depoling currents. In addition, the nonlinear FE-AFE material model was utilized in ALEGRA-FE to gain insight into the plate impact experiments. Two different pressure regimes were examined (~1.4 GPa and 0.9 GPa). The ferroelectric layers were fully depoled, and the released electrical energy was successfully transferred ahead of the shock front. The layered structure resulted in a velocity profile structure associated with wave scattering. The impact velocity appeared to affect the composite wave speed, rise time, and late-time velocity oscillation amplitude, while the electrical boundary conditions did not produce any discernable effect on mechanical response.

While chapters 2 – 4 discuss the shock response of electromechanical materials, chapter 5 details the preliminary findings of a novel mechanical test bed for reactive multilayer material systems. The experimental techniques described in chapters 3 and 4 lack the ability to probe the effects of high strain-rate on microstructure in a timely and cost-effective manner. Chapter 5 develops a high strain-rate experimental technique based on a laser-driven shock compression system, where reactive multilayer materials are deposited as a thin film onto copper nanopillars and shocked at various intensities. The nanopillar platforms enable pre- and post-shock analysis of the material system on a microstructural level by utilizing scanning electron microscopy and transmission electron microscopy. While the findings are preliminary, the results indicate that this system holds potential for investigating the layer interdiffusion necessary for the ignition of multilayer reactive material systems. Chapter 6 ends with a brief summary of the combined research and its implications.

1.7 References

1. R. Jankowski, K. Wilde, and Y. Fujino, "Reduction of pounding effects in elevated bridges during earthquakes," *Earthq. Eng. Struct. D.*, vol. 29, pp. 195-212, Feb. 2000.

2. N. N. Thadhani, "Shock-induced chemical reactions and synthesis of materials," *Prog. Mater. Sci.*, vol. 37, pp. 117-226, March 1993.

3. A. Nakagawa *et al.*, "Mechanisms of primary blast-induced traumatic brain injury: insights from shock-wave research," *J. Neurotrauma,* vol. 28, pp. 1101-1119, June 2011.

4. R. Monti, "Normal shock wave reflection on deformable solid walls," *Meccanica*, vol. 5, pp. 285-296, Dec. 1070.

5. P. Krehl, *History of Shock Waves, Explosions and Impact*, Springer-Verlag Berlin Heidelberg, 2009.

6. L. L. Altgilbers *et al.*, *Explosive Pulsed Power*, World Scientific, 2011.

7. I. Fritz and J. Keck, "Pressure-temperature phase diagrams for several modified lead zirconate ceramics," *J. Phys. Chem. Solids,* vol. 39, pp. 1163–1167, April 1978.

8. P. C. Lysne and C. M. Percival, "Electric energy generation by shock compression of ferroelectric ceramics: normal- mode response of PZT 95/5*," *J. Appl. Phys.,* vol. 46, pp. 1519–1525, April 1975.

9. 37. D. A. Berlincourt, H. H. A. Krueger, and C. Near, "Properties of piezoelectric ceramics," MorganElectro Ceramics, Technical Publication 226, 1999.

10. O. M. Stuetzer, "Secondary stresses in a stress pulse activated piezoelectric element," *J. Appl. Phys.*, vol. 38, pp. 3901-3904, May 1967.

11. M. Redwood, "Transient performance of a piezoelectric transducer," *J. Acoust. Soc. Am.*, vol. 33, no. 4, pp. 527-536, April 1961.

12. W. J. Halpin, "Current from a shock-loaded short-circuited ferroelectric ceramic disk," *J. Appl. Phys.*, vol. 37, no. 1, pp. 153-163, Jan. 1966.

13. W. Mock and W.H. Holt, "Pulse charging of nanofarad capacitors from the shock depoling of PZT 56/44 and PZT 95/5 ferroelectric ceramics," *J. Appl. Phys.,* vol. 49, no. 12, pp. 5846-5854, Dec. 1978.

14. J. C. Valadez *et al.*, "The effect of a hydrostatic pressure induced phase transformation on the unipolar electrical response of Nb modified 95/5 lead zirconate titanate," *J. Appl. Phys.,* vol. 111, pp. 024109-16, Dec. 2012.

15. M. D. Furnish *et al.*, "Dynamic electromechanical characterization of axially poled PZT 95/5," *AIP Conf. Proc.,* vol. 505, pp. 975, Jan. 2000.

16. J. J. Dick and J. E. Vorthman, "Effect of electrical state on mechanical and electrical response of a ferroelectric ceramic PZT 95/5 to impact loading," *J. Appl. Phys.,* vol. 49, pp. 2494, Aug. 1978.

17. L. Chao-Hui *et al.*, "Modeling of PZT ferroelectric ceramic depolarization driven by shock stress, *Chin. Phys, Lett*, vol. 28, no. 8, pp. 088301, Jan. 2011.

18. D. Jiang *et al.*, "Self-generated electric field suppressing the ferroelectric to antiferroelectric phase transition in ferroelectric ceramics under shock wave compression," *J. Appl. Phys.*, vol. 111, pp. 024103, Jan. 2012.

19. R. K. Linde, "Depolarization of ferroelectrics at high strain rates," *J. Appl. Phys.*, vol. 38, no. 12, pp. 4839-4842, Nov. 1967.

20. D. G. Doran, "Shock-wave compression of barium titanate and 95/5 lead zirconate titanate," *J. Appl. Phys.,* vol. 39, no. 1, pp. 40-47, Jan. 1968.

21. W. J. Halpin, "Resistivity estimates for some shocked ferroelectrics," *J. Appl. Phys.*, vol. 39, no. 8, pp. 3821-3826, July, 1968.

22. P. C. Lysne, "Dielectric properties of shock-wave-compressed PZT 95/5,"*J. Appl. Phys.*, vol. 48, no. 3, pp. 1020-1023, March 1977.

23. L. C. Chhabildas, "Dynamic shock studies of PZT 95/5 ferroelectric ceramic," Sandia National Labs., Albuquerque, NM, SAND-84-1729, 1984.

24. R. E. Setchell *et al.,* "Dynamic electromechanical characterization of the ferroelectric ceramic PZT 95/5," *AIP Conf. Proc.,* vol. 429, no. 1, pp. 781-784, 1998.

25. D. H. Zeuch, S. T. Montgomery, and D. J. Holcomb, "Uniaxial compression experiments on lead zirconate titanate 95/5-2Nb ceramic: Evidence for an orientation-dependent, "maximum compressive stress" criterion for onset of the ferroelectric to antiferroelectric polymorphic transformation," *J. Mater. Res.,* vol. 15, no. 3, pp. 689-703, March 2000.

26. D. H. Zeuch, S. T. Montgomery, and J. D. Keck, "Hydrostatic and triaxial compression experiments on unpoled PZT 95/5–2Nb ceramic: The effects of shear stress on the FR1 → AO polymorphic phase transformation," *J. Mater. Res.,* vol. 7, no. 12, pp. 3314-3332, Dec. 1992.

27. D. H. Zeuch, S. T. Montgomery, and D. J. Holcomb, "The effects of nonhydrostatic compression and applied electric field on the electromechanical behavior of poled lead zirconate titanate 95/5-2Nb ceramic during the ferroelectric to antiferroelectric polymorphic transformation," Journal of Materials Research, *J. Mater. Res.,* vol. 14, no. 5, pp. 1814-1827, May 1999.

28. M. D. Furnish *et al.*, "Gas gun impact testing of PZT 95/5, part 1: Unpoled state," Sandia National Labs., Albuquerque, NM, SAND-99-1630, 2000.

29. R. E. Setchell, "Recent progress in understanding the shock response of ferroelectric ceramics," *AIP Conf. Proc.,* vol. 620, no. 1, pp. 191-196, 2002.

30. R. E. Setchell *et al.*, "The effects of shock stress and field strength on shock-induced depoling of normally poled PZT 95/5," AIP Conf. Proc., vol. 505, no. 1, pp. 979-982, 2000.

31. R. E. Setchell, "Shock wave compression of the ferroelectric ceramic $Pb_{0.99}(Zr_{0.95}Ti_{0.05})_{0.98}Nb_{0.02}O_3$: Hugoniot states and constitutive mechanical properties," *J. Appl. Phys.*, vol. 94, no. 1, pp. 573-588, March 2007.

32. R. E. Setchell *et al.*, "Dielectric properties of PZT 95/5 during shock compression under high electric fields. *AIP Conf. Proc.*, vol. 845, no. 1, pp. 278-281, 2006.

33. R. E. Setchell, "Shock wave compression of the ferroelectric ceramic $Pb_{0.99}(Zr_{0.95}Ti_{0.05})_{0.98}Nb_{0.02}O_3$: Depoling currents," *J. Appl. Phys.*, vol. 97, no. 1, pp. 013507-16, Feb. 2005.

34. R. E. Setchell, "Shock wave compression of the ferroelectric ceramic $Pb_{0.99}(Zr_{0.95}Ti_{0.05})_{0.98}Nb_{0.02}O_3$: Microstructural effects," *J. Appl. Phys.*, vol. 101, no. 5, pp. 053525-9, March 2007.

35. R. E. Setchell, B.A. Tuttle, and J.A. Voigt, "Microstructural effects on the shock response of PZT 95/5," *AIP Conf. Proc.*, vol. 706, no. 1, pp. 180-186, 2004.

36. R. E. Setchell *et al.*, "Effects of initial porosity on the shock response of normally poled PZT 95/5, "*AIP Conf. Proc.*, vol. 620, no. 1, pp. 209-212, 2002.

37. J. Foley, "Shock-Mitigating Multilayered Mechanical Metamaterials (SM5)," Air Force Research Laboratory, Eglin AFB Fl Munitions Dir/Ordnance Division, 2012.

38. S. Zhuang, G, Ravichandran, and D. E. Grady, "An experimental investigation of shock wave propagation in periodically layered composites," *J. Mech. Phys. Solids,* vol. 51, pp. 245-265, 2003.

39. X. Chen, N. Chandra, and A. M. Rajendran, "Analytical solution to the plate impact problem of layered heterogeneous material systems," *Int. J. Solids Struct.,* vol. 41, pp. 4635-4659, April 2004.

40. X. Chen and N. Chandra, "The effect of heterogeneity on plane wave propagation through layered composites," *Compos. Sci. Technol.*, vol. 64, pp. 1477-1493, August 2004.

41. L. Tsai and V. Prakash, "Structure of weak shock waves in 2-D layered material systems," *Int. J. Solids Struct.*, vol. 42, pp. 727-750, August 2004.

42. T. J. Vogler, J. P. Borg, and D. E. Grady, "On the scaling of steady structured waves in heterogeneous materials," *J Appl. Phys.* vol. 112, pp. 123507, Dec. 2012.

43. J. W. Swegle and D. E. Grady, "Shock viscosity and the prediction of shock wave rise times," *J. Appl. Phys.*, vol. 58, no. 2, pp. 692, July 1985.

44. MTS Systems Corporation. (May 2015). *MTS Series 793 Control Software (Release 5.9 A)* [Online]. Available: https://www.mts.com/en/services/Manuals/MTS_010175

45. K. T. Ramesh, "High Rates and Impact Experiments," in *Springer Handbook of experimental solid mechanics*, Springer US, 2008, pp. 929-960.

46. D.J. Frew, M.J. Forrestal, and W. Chen, "Pulse shaping techniques for testing brittle materials with a split Hopkinson pressure bar," *Exper. Mech.* vol. 42, pp. 93–106, March 2002.

47. D.S. Drumheller, *Introduction to Wave Propagation in Nonlinear Fluids and Solids,* Cambridge: Cambridge Univ. Press, 1998.

48. M.A. Meyers: *Dynamic Behavior of Materials,* New York: Wiley, 1994.

49. S. Minshall, "Investigation of a polymorphic transition in iron at 130 kb," *Phys. Rev.*, vol. 98, pp. 271, 1955.

50. L. M. Barker, "VISAR vs PDV," Valyn International.

51. D. H. Dolan, "Foundations of VISAR analysis," Sandia National Labs., Albuquerque, NM, SAND-2006-1950, 2006.

52. D. H. Dolan, "Accuracy and precision in photonic Doppler velocimetry," *Rev. Sci. Instrum.*, vol. 81, pp. 053905, May 2010.

53. B. J. Jensen *et al.* "Accuracy limits and window corrections for photon Doppler velocimetry," *J. Appl. Phys.*, vol. 101, pp. 013523, Jan. 2007.

54. A. C. Robinson *et al.* "ALEGRA: an arbitrary Lagrangian-Eulerian multimaterial, multiphysics code," in *AIAA Aerospace Science Meeting and Exhibit,* Reno, NV, 2008.

2 Piezoelectrics for Shock Mitigation

2.1 Introduction

In impact and blast events, it is not only the penetrating shrapnel that can damage sensitive devices, but also the transmitted shock wave. The shock structure, from the steepness of the front to the late-time profile, all have marked effects on the amount of damage they produce. For example, the spall strength in stainless steel[1] and copper[2,3] is nearly twice as high for triangle wave profiles compared to square wave profiles, with significant differences in damage evolution. Both the magnitude of stress and impulse duration are important in protecting sensitive structures.[4] As such, the ability to modify an incident shock's structure is paramount in the design of shock wave mitigating systems.

Traditionally, shock waves have been mitigated through energy absorption or redirection. Metal armor plates absorb shock energy through ductile deformation,[5] which can be enhanced with the addition of a polymer backing.[6] Core composites of sandwiched material between two metal faceplates have also been effective at absorbing energy, as the core material can be made of collapsible pores that can either attenuate[7] or amplify peak pressure.[8] Shock metamaterials have also been developed based on the scattering or transfer of shock energy. Systems incorporating coupled spring-masses have been suggested for blast attenuation, where negative effective mass density is utilized to localize momentum.[9] Linearly-nonlinearly coupled systems, such as those utilizing internally rotating masses, have demonstrated the ability to unidirectionally transfer kinetic energy absorbed in the linear part of the system to the nonlinear portion, where it can be effectively dissipated.[10]

Periodic, impedance-mismatched layered composites have also been proven effective at shock attenuation through dissipative geometric dispersion.[11] The interaction of compression and

rarefaction waves from impedance-mismatched interfaces results in a lower shock velocity, a longer shock rise time, and an oscillatory late time wave profile.[12] The late time oscillations can be mitigated by viscoelastic layers that cyclically absorb the shock energy and therefore increase shock attenuation.[13,14,15] The impedance-mismatched composite does not have to be layered; metallic foams[16] and granular materials[17] have similarly been proven effective at wave scattering.[18] More recently, techniques have been borrowed from phononic crystals, which attenuate vibrations over a specific bandwidth. Periodic, hierarchical composites have been constructed where multiple periodicities over various length scales result in the superimposing of bandgaps for broadband attenuation.[19]

Active materials, such as piezoelectric ceramics, also hold great promise in altering the shock structure of blast and impact waves. The shock compression of piezoelectrics generates an electric potential at the shock front through the direct piezoelectric effect. When an electrical shunt is placed between the two electrodes of a shock loaded piezoelectric, the electrical energy can be transferred ahead of the shock front nearly instantaneously due to the faster speed of electricity. As this electrical energy is redistributed, it modifies the stress state of the piezoelectric ahead of the shock via the converse piezoelectric effect (fig. 2.1). These 'secondary stresses' can modify both the stress profile and momentum distribution within the piezoelectric. Since the electric response is considered quasistatic in comparison to the mechanical response, these effects can be continuously modified while the shock front traverses the piezoelectric.

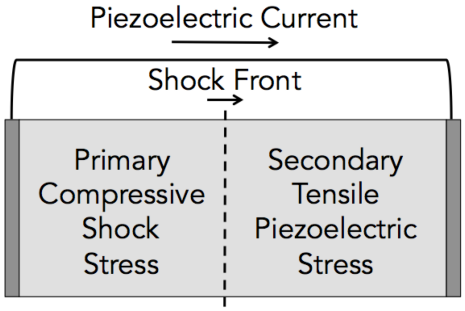

Figure 2.1: The shock wave imparts mechanical energy via compression of the piezoelectric, which is transformed into electrical energy via the direct piezoelectric effect. The electrical energy propagates ahead of the shock front nearly instantaneously visa the electrical shunt as the shock traverse the piezoelectric. Ahead of the front, the electrical energy is transformed into mechanical energy in the form of a secondary tensile stress wave via the converse piezoelectric effect. The electrical boundary conditions across the piezoelectric determine the amount of energy that can be propagated ahead of the shock front.

In 1961, Redwood[20] derived an analytical expression for the shock response of piezoelectric plates and bars poled in the direction of shock propagation (the so-called axial configuration) under open circuit and under large load resistance conditions using Laplace transform calculus. He showed that there was an electric potential difference across the shock front, resulting in an electric field within the shocked region of the piezoelectric material. Stepanow[21] had suggested this might be the case back in 1933 when he noticed that rocksalt developed a surface charge under transient loading. In 1966, Halpin[22] analyzed the transient loading of a ferroelectric disk subjected to axial shock loading. He developed an expression for the short circuit current that resulted from the depoling of the ferroelectric, and acknowledged that the electrical boundary conditions required an electric field of opposite polarity to develop in the yet-unshocked region of the ferroelectric. The following year, Stuetzer[23] went one step further by showing that the opposite electric field in the unshocked region results in stresses due to the converse piezoelectric effect. While Stuetzer claimed to be the first to recognize these

'secondary stresses', Lobdell[24] pointed out that Redwood experimentally observed this phenomenon as 'wave reflections' but neglected to discuss it in detail.

Additional research into the electromechanical response of piezoelectrics subjected to shock loading continued throughout the 1970's. Lysne[25] incorporated a nonlinear equation of state utilizing Laplace transform calculus, specifically looking at the effect of strain on the piezoelectric and dielectric properties and the effect of electric displacement on stiffness. Chen[26] developed an explicit expression for the fully coupled electromechanical response to shock loading, capable of including a variety of different circuit elements such as inductors and capacitors. Duvall[27] developed a Maxwell-like relation to explain the compressive stress relaxation seen in piezoelectrics under short circuit conditions. Lynse[28] developed an expression for the equation of state to take into account the combined linear piezoelectric and nonlinear ferroelectric response, which illustrated how shock loading could act to repolarize the ferroelectric under axial configuration. In 1986, Ani and Maugin[29] developed jump relations and the Hugoniot equation for piezoelectric materials under strong discontinuous shock loading. In 2006, Fish and Chen[30] formulated a procedure for computing the shock response of heterogeneous periodic piezoelectric media based on multiphysics finite element modeling using representative volume elements. In 2011, Hopkins and Gozanas[31,32] investigated the fully-coupled, nonlinear response of piezoelectrics by comparing the linear response to the nonlinear using multiphysics finite element modeling. They verified the linear results using Laplace transforms and a modified Dubner-Abate-Crump algorithm, and then discussed the effects of nonlinear coupling with regards to the higher-order elastic, dielectric, and piezoelectric coupling coefficients.

The stress and electrical displacement are related through the piezoelectric constitutive equations (Eq. 2.1 & 2.2).

$$T_i = C_{ij}^E S_j - e_{ij} E_j \tag{2.1}$$

$$D_i = e_{ij} S_j + \varepsilon_{ij} E_j \tag{2.2}$$

Here we adopt the notation common to discussing piezoelectrics. T, S, E, and D denote the stress, strain, electric field, and electric displacement written in reduced Voigt notation. Reduced Voigt notation can be implemented due to the symmetry of the system. C^E, e, and ε are the short circuit elastic moduli, piezoelectric moduli, and dielectric permittivity. Under shock loading, the material is subjected to uniaxial strain loading conditions, reducing the piezoelectric constitutive equations to equations 2.3 & 2.4.

$$T_3 = C_{33}^E S_3 - e_{33} E_3 \tag{2.3}$$

$$D_3 = e_{33} S_3 + \varepsilon_{33} E_3 \tag{2.4}$$

Here the x-3 direction will be synonymous with the z direction; the direction of shock propagation and the direction of polarization for the piezoelectric. Under open circuit conditions, the electric displacement change is zero, yielding an expression for the stress-induced electric field (Eq. 2.5).

$$E_3 = -\frac{e_{33} S_3}{\varepsilon_{33}} \tag{2.5}$$

Equation 2.5 leads to an expression for the piezo-modified stress within the material, broken up into separate contributions (Eq. 2.6).

$$T_3 = \left(C_{33}^E + \frac{e_{33}^2}{\varepsilon_3} \right) S_3 = C_{33}^D S_3 \tag{2.6}$$

Here C^D is the open circuit, piezo-modified elastic modulus and k is the electromechanical coupling factor. This stress can be broken into the purely mechanical C^E*S term and the piezoelectric e^2/ε*S term. The former is due to the mechanical bonds within the material, the latter due to the electrical dipole field resisting compression.

Now let us define a shock traveling through a piezoelectric material capped with electrodes of similar mechanical impedance. Let the shock traverse from the left to right along the positive z direction, and let the piezoelectric be poled in the same direction. As the shock traverses the piezoelectric (fig. 2.2), the dipoles are compressed within the shocked region, resulting in a potential difference at the shock front. The resulting positive electric field within the shocked region is due to the direct piezoelectric effect. Ahead of the shock, the dipoles and surface charges remain unchanged, and therefore no electric field is present. Once the shock front traverses the entirety of the piezoelectric element, the charge imbalance on the opposing electrodes results in a uniform positive electric field, exactly as in the quasistatic open circuit case.

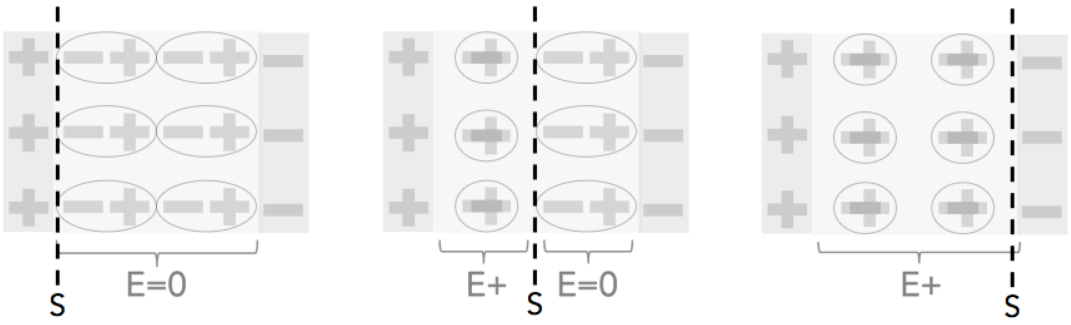

Figure 2.2: Schematic of the piezoelectric response to transient shock loading under open circuit conditions. Initially, dipole charges are balanced by charge on the electrodes, resulting in no electric field within the piezoelectric. As the shock front sweeps the piezoelectric, the internal dipoles are compressed and reduce in strength, causing a potential difference between the front electrode and the shock front interface. This potential difference results in a positive electric field within the shocked region. Under open circuit configuration, no charge is allowed to flow between the two electrodes, and the electric field within the yet unshocked region of the material remains null. After the piezoelectric is fully compressed by the shock, there exists an electric field within the piezoelectric due to the potential difference between the electrodes.

Figure 2.3 illustrates the same situation, only now under short circuit conditions. These conditions require the voltage between the two electrodes to be equal, resulting in charge transfer between the front and rear electrodes via the electrical shunt. At any time, the integral of

the electric field in the shocked region (superscript S) must be equal and opposite of the integral of the electric field in the unshocked region (superscript U), as shown in equation 2.7.

$$\int_0^l E^S \, dz = -\int_l^L E^U \, dz \tag{2.7}$$

Here L is the length of the piezoelectric and l is the length of the shock compressed region. The negative electric field that develops in the unshocked region induces a tensile 'secondary' stress wave the due to the converse piezoelectric effect. If the back surface of the piezoelectric is mechanically free, this tensile stress wave results in the contraction of the unshocked region. If the back surface is mechanically clamped, the tensile stress builds and reduces the compressive stress at the shock front.

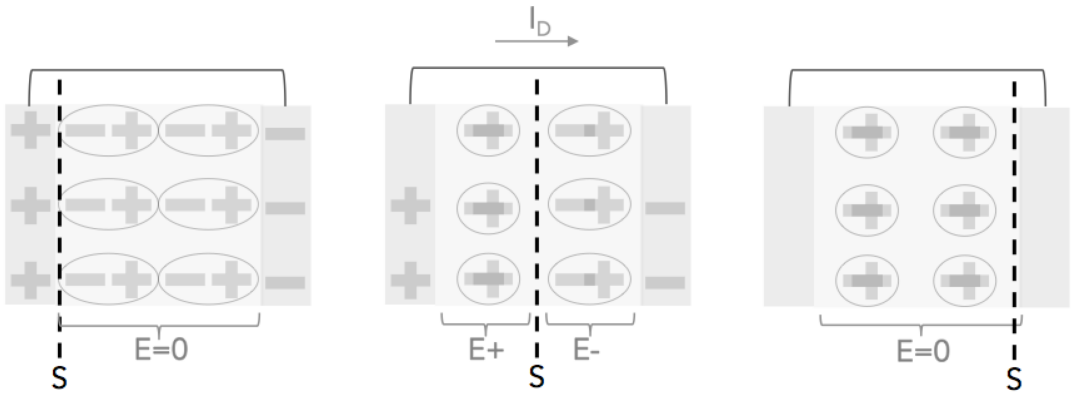

Figure 2.3: Schematic of the piezoelectric response to transient shock loading under short circuit conditions. Initially, dipole charges are balanced by charge on the electrodes, resulting in no electric field within the piezoelectric. As the shock front sweeps the piezoelectric, the internal dipoles are compressed and reduce in strength, causing a potential difference at the front electrode and the shock front interface. This potential difference results in a positive electric field within the shocked region. Under short circuit configuration, I depoling current I_D flows across the shunt to equalize the potential difference between electrodes. The change in potential of the rear electrode results in an electric field of opposite polarity within the yet unshocked region of the material. This electric field in the unshocked region results in a tensile stress wave that alters both the particle velocity and stress within the piezoelectric. After the piezoelectric is fully compressed by the shock, no electric field exists within the piezoelectric since the electrode potential is equal.

The magnitude of the secondary stress that develops in the unshocked region of the piezoelectric under short circuit conditions is dependent on the electromechanical coupling factor of the piezoelectric material. The maximum electric field in the shocked region of the piezoelectric is generated immediately after the shock enters the material, when the potential difference across the shock front is closest to the front electrode. Since the potential difference across the shock front is assumed to remain constant, the maximum field in the unshocked region of the short-circuited piezoelectric must occur just as the shock approaches the rear electrode. The maximum fields that occur within the shocked and unshocked regions are approximate in magnitude but opposite in polarity (Eq. 2.8). If the rear surface of the piezoelectric is mechanically clamped, no strain is present in the unshocked region and the uniaxial strain constitutive relation for this region is dependent on electric field only (Eq. 2.9). Combining equations 2.5, 2.8, and 2.9 leads to an expression for the maximum secondary stress (Eq. 2.10). If we further assume constant piezoelectric and dielectric moduli, we can write the ratio of maximum secondary stress in the unshocked region to that of the initial stress in the shocked region (Eq. 2.11). Equation 2.11 illustrates how piezoelectric materials may transfer a significant portion of mechanical energy from the shock stress ahead of the shock front and modify the stress state of the yet-unshocked region.

$$\mathrm{E}_3^{\mathrm{U}\max} \approx -\mathrm{E}_3^{\mathrm{S}\max} \tag{2.8}$$

$$\mathrm{T}_3^{\mathrm{U}} = -\mathrm{e}_{33}^{\mathrm{U}}\mathrm{E}_3^{\mathrm{U}} \tag{2.9}$$

$$\mathrm{T}_3^{\mathrm{U}\max} \approx -\frac{\mathrm{e}_{33}^{\mathrm{U}}\mathrm{e}_{33}^{\mathrm{S}}\mathrm{S}_{33}^{\mathrm{S}}}{\varepsilon_{33}^{\mathrm{S}}} \tag{2.10}$$

$$\frac{\mathrm{T}_3^{\mathrm{U(max)}}}{\mathrm{T}_3^{\mathrm{S(max)}}} \approx \frac{\mathrm{e}_{33}^2}{\varepsilon_3\mathrm{C}_{33}^{\mathrm{E}} + \mathrm{e}_{33}^2} = \frac{\mathrm{k}_{33}^2}{1+\mathrm{k}_{33}^2} \tag{2.11}$$

In this work, we investigate the effects of the secondary stresses that are generated from the transfer of mechanical energy out of the shock-compressed region and ahead of the shock front via the piezoelectric effect using the multiphysics shock code ALEGRA-FE[33]. First, a single layer of piezoelectric is examined in one dimension to elucidate the ability to dynamically tune the secondary stress wave. Next, the electrical boundary conditions are varied along a perpendicular direction in reference to the shock propagation direction to demonstrate spatial modification of the secondary stress waves. Finally, the effect of secondary stress waves within a layered composite is examined to explore the control of geometric wave dispersion.

2.2 Procedure: ALEGRA-FE Piezoelectric Module Simulation

The electromechanical response of piezoelectrics to shock loading was simulated using state-of-the-art multiphysics finite element modeling. ALEGRA-FE[33] is an arbitrary Lagrangian-Eulerian (ALE) shock hydrodynamic finite element code developed by Sandia National Laboratories. It uses an ALE hybrid scheme to circumvent some of the difficulties associated with using a purely Eulerian or purely Lagrangian method. The additional ferroelectric (FE) module allows for dynamic electromechanical characterization of piezo- and ferroelectric materials, in addition to coupled electrical circuits. Since the characteristic time of the electrical response of piezoelectric materials is orders of magnitude faster than that of the shock wave propagating through them, the electromechanics of the system can be solved quasistatically. The code utilizes linear piezoelectric constitutive equations in order to compute the electromechanical response, and assumes the elastic, dielectric, and piezoelectric moduli remain constant under mechanical and electrical loading. A full description of the operating methodology is available.[33, 34]

In this work, the effects of secondary stresses on the stress and momentum distribution within the piezoelectric material lead zirconate titanate subjected to uniaxial strain via plate

impact are explored by spatially and temporally varying the electrical boundary conditions across the piezoelectric. The material properties of PZT-5A were used for the piezoelectric material.[35] The direction of polarization and shock propagation are collinear (the so-called axial configuration), where the shock propagates in the positive z-direction. Brass was chosen as the electrode material due to its similar impedance with PZT-5A (36.7[36] vs 33.7[37] Mrayl), and in all cases the electrode thicknesses were limited to 100 μm. Uniaxial strain mechanical boundary conditions were ensured by setting the displacements in the lateral (x and y) directions to zero at the lateral edges of the models. ALEGRA-FE requires a fully three dimensional geometry, however the mechanical boundary conditions essentially reduce the results presented here to either one or two dimensions. Since the code treats the piezoelectric material response as linear, all stress and velocity data are normalized by the initial impact stress or velocity magnitudes.

In the first set of simulations, a single layer of piezoelectric material subjected to shock loading was modeled under various electrical boundary conditions. The uniaxial strain boundary conditions essentially reduced the results to one dimension, where the shock traversed a 5 mm thick piezoelectric layer capped with brass electrodes (fig. 2.4a). A brass impactor was used with an initial velocity in the positive z direction. The impactor was sufficiently thick as to ensure that any release waves were not present in the piezoelectric layer for the duration of the simulation. The mechanical boundary conditions applied to the back surface of the piezoelectric were varied to either investigate the stress or momentum profiles. First, the back surface was kept mechanically free, and the back surface particle velocity histories recorded using a point tracer probe placed in the center of the rear surface. Second, the back surface was mechanically clamped in the z-direction to allow the secondary stresses to grow to their maximum values, and a line tracer down the z-axis was used to examine the stress profile within the piezoelectric. The electrical boundary conditions were additionally varied between open and short circuit by tuning

the series resistance across the piezoelectric. Finally, the effect of dynamically switching the electrical boundary conditions mid transit was examined.

For the second set of simulations, the effect of spatially varying the electrical boundary conditions was explored. The essentially one-dimensional model from the first set of simulations was expanded along the x direction by splitting the front and rear electrodes into nine pairs, as shown in figure 2.4b. 100 μm strips of Kapton kept the electrodes electrically isolated, allowing the electrical boundary conditions across the piezoelectric to be modified laterally through each of the nine electrically independent pairs of electrodes. The piezoelectric was kept at 5 mm in thickness, and each pair of electrodes was 1 mm in length. A PMMA impactor was used so that the front electrodes would remain electrically isolated. The series resistances across the nine independent electrodes were then varied, while the back surface of the piezoelectric was mechanically clamped.

For the third set of simulations, a layered composite was examined. A composite of ten 2.8 mm thick piezoelectric layers, each capped with brass electrodes and electrically isolated from one another by 100 μm thick layers of Kapton, were stacked along the z direction (fig. 2.4c). A brass impactor was used to ensure symmetric impact conditions, and a velocity tracer at the impact plane captured the reflected wave trains from the composite. The electrical boundary conditions of the piezoelectric layers were switched between open and short circuit to alter the profile of the final shock structure. The 2.8 mm thickness of the piezoelectric layers was chosen to maximize attenuation of the wave reflections from the Kapton layers under short circuit boundary conditions.

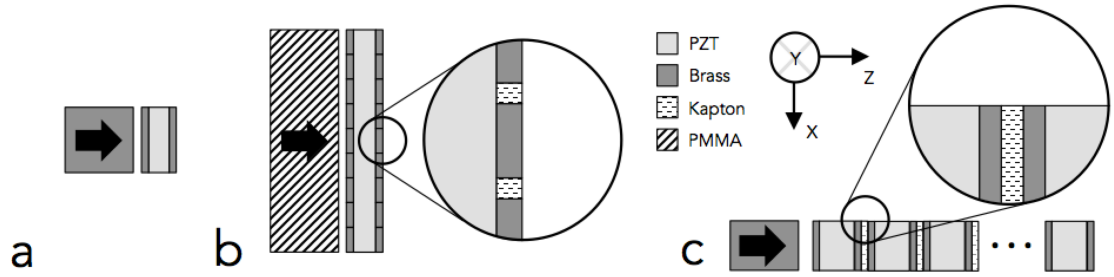

Figure 2.4: Composite morphologies. Impactors are shown with black arrows; all shock waves traverse the composites in the positive z direction. The first set of simulations (a) involved a brass impactor incident on a 5 mm thick block of piezoelectric sandwiched between two brass electrodes of 100 μm thickness. The second set of simulations (b) extended the length along the x direction and split the brass electrodes into nine electrically independent segments, separated by 100 μm strips of electrically isolating Kapton. In addition, a PMMA impactor was used. The third set of simulations (c) involved a brass flyer impacting a multilayered composite, where each piezoelectric layer was 2.8 mm thick. 100 μm thick layers of Kapton were used between each sequential piezoelectric electrode, allowing for independent electrical control of each piezoelectric layer.

2.3 Results

Figure 2.5 shows progressive snapshots of the electric field (a & b) and stress (c & d) distribution along the z direction within a shock loaded piezoelectric layer under both open circuit (a & c) and short circuit (b & d) boundary conditions. Utilizing the geometry of figure 2.4a, the rear surface of the piezoelectric was mechanically clamped so that no relaxation of the secondary stresses could take place. Figure 2.5a shows the electric field distribution within the piezoelectric for open circuit conditions. No charge may flow between the electrodes in the open circuit case, and therefore the electric field is restricted to the shock-compressed region of the piezoelectric. The stress profile of the piezoelectric under open circuit conditions (fig. 2.5c) shows no secondary stresses in the unshocked region. Figure 2.5c shows the electric field distribution within the piezoelectric for short circuit conditions. Under these conditions, charge is allowed to flow between the two electrodes in order to maintain equal potential, resulting in the development of an electric field of opposite polarity in the unshocked region of the piezoelectric.

The stress profile of the piezoelectric under short circuit conditions show secondary stresses that increase as the wave traverses the piezoelectric. The magnitude of the stress at the shock front is reduced by the secondary stress, which reaches a maximum of 23% of the incident stress magnitude.

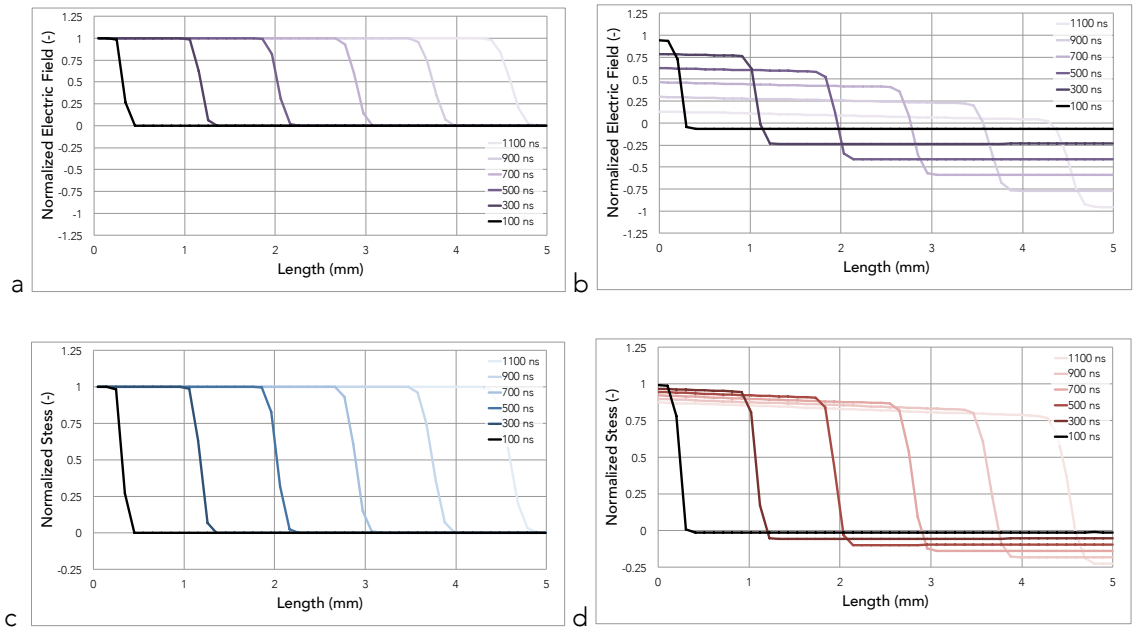

Figure 2.5: Cauchy stress (c & d) and electric field (a & b) profiles for four sequential times illustrating shock propagation in the z direction across the 5 mm thick piezoelectric under open circuit (left) and short circuit (right) electrical boundary conditions. In the short circuit configuration, the compressive stress of the shock is eventually reduced by 23%.

Figure 2.6a shows the stress profiles under various resistive loads at a time when the secondary stresses are at a maximum. As above, open circuit conditions do not result in any secondary stresses in the unshocked region, while short circuit conditions produce the highest secondary stresses in this region. By varying the series resistance between the electrodes (2 kΩ - 10 kΩ), the amount of generated secondary stress in the unshocked region can be tuned.

Figure 2.6b shows the back surface particle velocity histories of a piezoelectric under various time dependent electrical boundary conditions. The geometry of figure 2.4a was used, but this time the back surface was kept mechanically free so that the secondary stresses could

partially relax through piezoelectric contraction. Under open circuit conditions, the back surface particle velocity remains zero until the shock front arrives. The shock reflects off the free back surface as a release wave while increasing the back surface particle velocity to a constant value determined by the impedances of the materials and the initial flyer velocity. Since brass and PZT-5A have similar impedances, the impact can be approximated as symmetric. Under short circuit conditions, the generated tensile wave causes the material to contract as soon as the shock enters the piezoelectric. This is evident by the initial negative back surface particle velocity prior to the arrival of the shock front. The magnitude of this velocity can be as large as 12% of the impact velocity. After the shock reflects off the back surface, the piezoelectric behind the release wave expands, causing a continued rise of the back surface particle velocity beyond that of the open circuit case.

The effect of piezoelectric expansion can be separated from the effect of piezoelectric contraction by dynamically switching the electrical boundary conditions. The brown line in figure 2.6b illustrates the rear surface particle velocity history of a shock traversing the piezoelectric initially under short circuit conditions. The initial negative velocity is still evident due to piezoelectric contraction. When the shock front reaches the rear surface, the electrical boundary conditions are switched to open circuit, locking the potential of the electrodes. As the shock reflects back as a release wave, the piezoelectric material behind it is kept partially compressed due to the generated electric field. As the potential difference across the shock front moves away from the rear electrode, the piezoelectric slowly expands back to its original length, and the rear surface particle velocity increases to match that of the open circuit case.

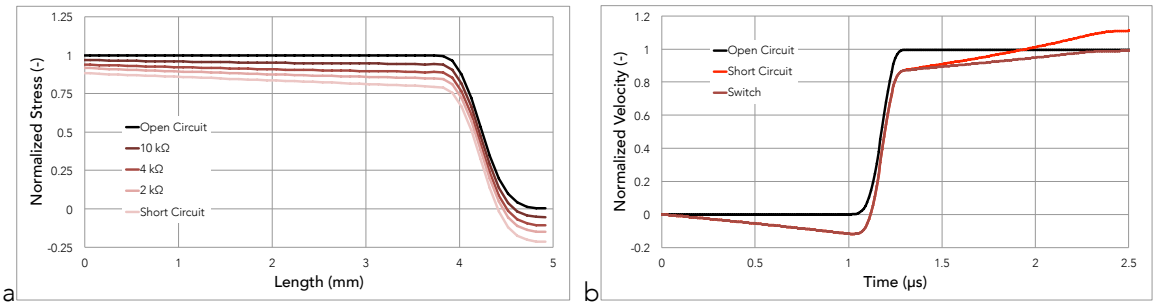

Figure 2.6: Normalized Cauchy stress profiles (a) for various series resistances, ranging from short circuit to open circuit, with tuning capable with series resistance between 2 kΩ to 10 kΩ. Normalized back surface particle velocities (b) for open circuit, short circuit, and a variable resistance switch.

Next, the ability to alter the shock structure spatially was investigated utilizing the geometry of figure 4b. Here the electrical boundary conditions of the nine pair of electrodes were set to either open circuit, short circuit, or tuned between the two using the various series resistances utilized previously. The back surface of the piezoelectric was mechanically clamped in the z direction, allowing the secondary stresses to build to their maximum values. The snapshots were taken at a time when the secondary stresses are at a maximum. The shock stress is represented using both relative height as well as the indicated color map, with the grey plane set at a height of zero stress.

Figure 2.7a shows the array of piezoelectric layers under alternating open and short circuit conditions. In general, the expected secondary stresses are present in the short circuit piezoelectric areas. However, there are additional compressive and tensile stresses in the vicinity of the interface between the open and short circuit electrodes. The concentrated electric fields in these regions induce tensile stresses at the corners of the short circuit regions. These stress concentrations cause significant shear stresses within the material that may lead to material failure. Figure 2.7b shows the array of piezoelectric blocks where the electrical boundary conditions have been gradually altered from open circuit conditions at the edges to short circuit

conditions in the center block using various series resistances. By gradually altering the electrical boundary conditions, the concentrated electric fields can be reduced, resulting in a reduction of shear stresses at the electrode interfaces when compared to figure 2.7a.

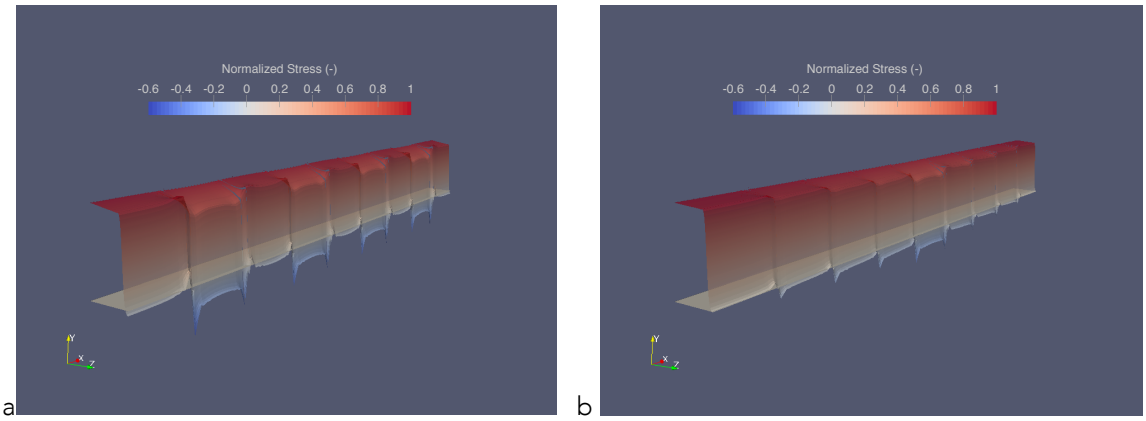

Figure 2.7: Normalized Cauchy stress profiles for alternating open/short (a) and gradual (b) open to short circuit boundary conditions, represented by both scaled height and color mapping. The snapshot is taken when the toe of the shock reaches the back surface and the secondary stresses in the short circuit regions are at a maximum. The grey plane is at a height of zero stress.

Finally, the effect of the electrical boundary conditions on wave scattering in a multilayered composite was investigated using the geometry of figure 2.4c. Figure 2.8a shows the back surface particle velocity histories of the composite for open and short circuit boundary conditions. The shock front and late-time profiles are markedly altered with electrical boundary conditions. Under open circuit, the late-time particle velocity exhibits oscillatory motion associated with shock front scattering at the impedance-mismatched Kapton interfaces. In the short circuit history, these oscillations are significantly reduced, however the average particle velocity is higher. To examine the nature of these variances, the particle velocity histories at the impact plane were plotted (fig. 2.8b). Owing to the symmetric impact conditions, roughly half of the initial flyer momentum propagates into the composite. Since the brass impactor is homogeneous, the particle velocity history at the impact plane can be associated with

backwards-traveling wave trains from each successive layer in the composite. The pulses seen under open circuit conditions are associated with wave reflections from the low-impedance Kapton layers, while the additional wave pulses under short circuit conditions are due to the secondary tensile waves within the piezoelectric layers.

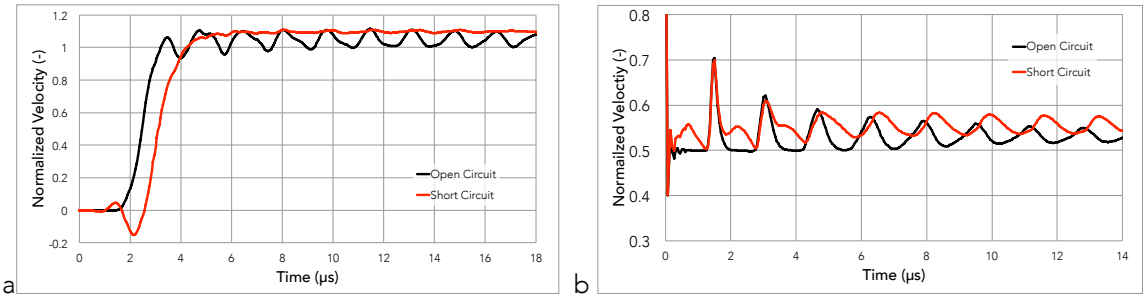

Figure 2.8: Normalized back surface particle velocity histories (a) for multilayer composites under open circuit and short circuit electrical boundary conditions. Normalized particle velocity histories (b) taken at the impact plane.

2.4 Discussion

The electrical boundary conditions of piezoelectric material subjected to shock loading can be used to alter the stress and momentum distribution within the shock front and late time profile. The secondary tensile stress wave reduces the stress at the shock front and/or imparts an initial negative particle velocity ahead of the front, depending on the mechanical boundary conditions of the piezoelectric. These effects can be tuned in real time by resistive circuits in series with the piezoelectric. The secondary stresses can be varied spatially by utilizing isolated pairs of electrodes, although the resulting shear stresses must be accounted for. In layered composites, the secondary stresses can have a marked effect on the shock arrival time and wave profile.

The secondary stress can act to reduce the compressive stress at the shock front by more than 20%. The tensile stress reduces the shock stress at the front, as seen in figure 2.5d. The Hugoniot jump relations dictate the initial change in stress across the shock front, and therefore

the drop in compressive stress behind the front in exactly equal to the tensile stress ahead of the front. This is the reason equation 2.8 must be approximated; the drop in the shock front stress creates a gradient of stress and thus electric field within the shocked region. The maximum electric field in the unshocked region, which is dictated by the sloped stress in the shocked region, will always be slightly lower than the maximum electric field within the shocked region, which occurs immediately after the shock enters the piezoelectric when there is no stress gradient. However, this difference is minimal; extrapolating the maximum tensile stress from figure 2.5d predicts a maximum reduction of 23.2%, matching well with the 23.4% predicted by equation 2.11 when using the piezoelectric, dielectric, and elastic moduli values utilized by the code.

The magnitude, duration, and location of the tensile secondary stresses can be tuned in real time by altering the electrical boundary conditions across the piezoelectric. Figure 2.6a illustrates how various electrical loads can tune the magnitude of the secondary stresses ahead of the shock. Figure 2.6b shows the ability to impart an initial negative momentum ahead of the shock front via piezoelectric contraction under short circuit boundary conditions. Upon release, the piezoelectric usually expands to impart additional positive momentum. However, by switching the electrical boundary conditions from short to open circuit after full piezoelectric contraction, the potential of the electrodes can keep the piezoelectric contracted upon release. Figure 2.7a shows how the electrical boundary conditions can be altered across the piezoelectric to modify the wave profile spatially. Significant shear stresses can develop at the interface of the open and short circuit electrodes, but figure 2.7b shows how the electrical boundary conditions can be gradually altered to minimize these effects. These simulations illustrate the fundamentals of spatially and temporally modifying shock structure using piezoelectric materials. Incorporation

of piezoelectric materials into morphologies such as layered composites can further expand the response of these systems to shock loading.

The wave front in impedance-mismatched layered composites can be altered using piezoelectric layers. In traditional periodic elastic layered composites, the reflected compression waves eventually outrun the shock front due to their faster wave speed resulting from traveling in a compressed media.[14] This has the effect of spreading the shock front and increasing the rise time. ALEGRA-FE uses the same wave speed within the piezoelectric media regardless of the compression state or electrical boundary conditions. Nonetheless, the shock front appears to arrive ~300 ns later in the short circuit configuration. The apparent delay in wave arrival is a result of modification of the shock front. Upon closer inspection, a small, initial positive velocity wave can be seen that is immediately followed by a negative velocity wave, a result of the secondary tensile waves from the piezoelectric layers. Just as in figure 2.6b, the shock creates a tensile wave within the piezoelectric layers just ahead of the shock front, imparting a negative particle velocity. As these leading tensile waves enter additional piezoelectric layers, they create their own leading compression waves with positive particle velocity. In figure 2.8a, the leading tensile wave has a negative particle velocity magnitude that is 15% of the impact velocity, matching closely with the magnitude of 12% from the single layer results of figure 2.6b. The small, leading compression wave, assumed to be generated from the leading tensile wave, has a positive particle velocity magnitude that is 5% that of the impact velocity, and 25% that of the leading tensile wave's particle velocity. The leading tensile wave has the effect of dropping the particle velocity of the shock front, essentially delaying the arrival by 300 ns.

During the late time oscillations, the secondary stresses have the effect of modulating the natural oscillation frequency by 180°, as seen by comparing the wave train profiles in the 10-14 μs range in figure 2.8b. Compression and rarefaction waves resulting from reflection from the

impedance-mismatched Kapton layers create leading secondary stress waves of opposite polarity within the piezoelectric layers, which in turn create their own waves. The result is a significant reduction of the late-time oscillation magnitude, from 13% of the impact velocity under open circuit, to 1% under short circuit configuration. This effect is dependent on the piezoelectric layer thickness; the duration of the secondary stress wave must be similar to the duration of the compressive and rarefaction waves generated by the impedance-mismatched Kapton layers. This is best illustrated by comparing the wave trains in figure 2.8b in the 0-4 μs range. For Kapton thicknesses of 100 μm, this requires piezoelectric thicknesses of 2.8 mm. In a physical composite, effects such as stress-dependent wave speed and mechanical impedance will additionally complicate the resulting wave profiles, however these results demonstrate the fundamental piezoelectric mechanisms that affect wave scattering in impedance-mismatched composites.

While these simulations suggest that piezoelectrics can be used to produce significant shock wave modification in real time, the physical limitations of the material place limits on this effect. Piezoelectric PZT can achieve compressive strengths of greater than 500 MPa, but their tensile strengths are limited to 30 MPa unless preloaded in compression.[38] In addition, to maintain operation in the linear piezoelectric regime where these simulation results are accurate, the piezoelectric must not undergo depolarization. PZT-5A begins to depole around 20 MPa under uniaxial quasistatic loading, however PZT-8 can achieve stresses up to 80 MPa.[38] Two factors may circumvent this issue. For impact situations where the force is applied over periods on the order of microseconds, piezoelectrics can maintain their linear behavior at much higher stresses due to insufficient time for domain reorientation.[39] Even when shock-induced depolarization drives the shocked region out of the piezoelectric regime, the unshocked region may still behave linearly to the resulting field if dielectric breakdown is avoided. Typical remnant polarization values for PZT-5A are around 26 $\mu C/cm^2$, corresponding to maximum electric fields

of tens of kV/mm.[40] However, Shkuratov et al. found that the maximum electric field that can be sustained before dielectric breakdown occurred around 3-5 kV/mm.[40] Using equation 2.9, this corresponds to a maximum secondary stress of approximately 50-90 MPa for PZT-5A. Assuming the same relative dielectric strength, the higher piezoelectric coefficients for PZT-5H would increase this value up to 130 MPa.[35] Of all the aforementioned material considerations, the tensile strength of the unshocked region is the limiting factor in developing the maximum secondary stresses in a shock loaded short circuited ceramic piezoelectric.

There is a class of piezoelectrics that can achieve a higher ratio of secondary to primary stress, albeit at lower magnitudes. Relaxor lead titanate (PT) based single crystal ferroelectrics have even higher piezoelectric coefficients than their polycrystalline counterparts; 3-4 times greater than the above-mentioned PZT ceramics. Unfortunately, their properties start to degrade at electric fields on the order of tenths of kV/mm as the crystals undergo a phase transformation out of the desirable rhombohedral phase.[41] Therefore the maximum secondary stress value they can achieve is limited to tens of MPa. Nonetheless, the ratio of secondary stress to initial stress can be as high as 40% for single crystal PMN-0.30PT due to the excellent dielectric and piezoelectric properties.[42] Advancements in piezoelectric materials may one day extend these excellent electromechanical properties into a system that can withstand the limiting tensile stresses and breakdown fields.

2.5 Conclusion

The effects of the electrical boundary conditions on the shock wave structure within piezoelectric materials and their composites were investigated using the multiphysics shock code ALEGRA-FE. The simulations demonstrate that energy from the shock can be transferred ahead of the front to modify the stress and momentum profile in real time via the piezoelectric effect. A

leading tensile stress wave can be created ahead of the shock that can reduce the stress in the front by more than 20%. The tensile wave can likewise propagate ahead of the front with a negative particle velocity of magnitude ~15% that of the impact velocity. The stress and momentum profiles of the shock wave can be modified both spatially and temporally by tuning the series resistances. The electrical boundary conditions can also influence the shock wave structure in impedance-mismatched, piezoelectric composites by attenuating wave scattering and delaying the shock front arrival. This research provides insight into incorporating piezoelectric materials into shock mitigating systems.

2.6 References

1. G.T. Gray, N.K. Bourne, and B.L. Henrie, "On the influence of loading profile upon the tensile failure of stainless steel," *J. Appl. Phys.*, vol. 101, pp. 093507, May 2007.

2. B.H. Sencer, S.A. Maloy, and G.T.Gray III, "The influence of shock-pulse shape on the structure/property behavior of copper and 316 L austenitic stainless steel," *Acta Materialia*, vol. 53, pp. 3293, June 2005.

3. G.T. Gray *et al.* "The effects of shockwave profile shape and shock obliquity on spallation: Kinetic and stress-state effects on damage evolution," *AIP Conf. Proc.*, vol. 1195, pp. 1097, Jan. 2010.

4. T. Rahimzadeha, E. M. Arrudaa, and M. D. Thoulessa, "Design of armor for protection against blast and impact," *J. Mech. Phys. Solids*, vol. 85, pp. 98-111, Sept. 2015.

5. G. I. Taylor, "Pressure and impulse of submarine explosion waves on plates," in *The Scientific Papers of Sir Geoffrey Ingram Taylor Aerodynamics and the Mechanics of Projectiles and Explosions*, vol. 3, G. K. Batchelor, Eds. Cambridge, UK: Cambridge University Press, 1963, pp. 287–303.

6. A. V. Amirkhizi *et al.*, "An experimentally-based viscoelastic constitutive model for polyurea, including pressure and temperature effects," *Philos. Mag.,* vol. 86, pp. 5847–5866, Nov. 2006.

7. Q. M. Li, and H. Meng, "Attenuation or enhancement – a one-dimensional analysis on shock transmission in the solid phase of a cellular material," *Int. J. Impact Eng.*, vol. 27, pp. 1049–65, Nov. 2002.

8. V. F. Nesterenko, "Shock (blast) mitigation by ''soft'' condensed matter," *MRS Symp. Proc.*, vol. 759, pp. MM4.3.1-MM4.3.12, 2003.

9. Y. Xu and V. F. Nesterenko, "Attenuation of short stress pulses in strongly nonlinear dissipative metamaterial," *J. Appl. Phys.,* vol. 117, pp. 114303, March 2003.

10. E. Smith, and A. Ferri, "Shock and Vibration Isolation using Internally Rotating Masses," *ASME. Int. Design Engineering Technical Conf. Computers Information Engineering Conf., Vol. 8: 27th Conf. Mechanical Vibration Noise*, Boston, MA, 2015, pp. V008T13A047.

11. S. Zhuang, G, Ravichandran, and D. E. Grady, "An experimental investigation of shock wave propagation in periodically layered composites," *J. Mech. Phys. Solids,* vol. 51, pp. 245-265, 2003.

12. X. Chen, N. Chandra, and A. M. Rajendran, "Analytical solution to the plate impact problem of layered heterogeneous material systems," *Int. J. Solids Struct.,* vol. 41, pp. 4635-4659, April 2004.

13. K. T. Tan, H. H. Huang, and C. T. Sun, "Blast-wave impact mitigation using negative effective mass density concept of elastic metamaterials," *Int. J. Impact Eng.*, vol. 64, pp. 20-29, Oct. 2013.

14. L. Tsai and V. Prakash, "Structure of weak shock waves in 2-D layered material systems," *Int. J. Solids Struct.*, vol. 42, pp. 727-750, August 2004.

15. L. Tsai, and V. Prakash. "Experimental determination of shock structures in heterogeneous layered material systems," Case Western Reserve Univ., Cleveland, OH, July 2005.

16. M D Goel *et al.*, "Interaction of a Shock Wave with a Closed Cell Aluminum Metal Foam," *Combust. Explos. Shock Waves*, vol. 51, no. 3, pp. 373-380, June 2015.

17. D. E. Grady, "Structured shock waves and the fourth-power law," *J. Appl. Phys.*, vol. 107, pp. 013506, Jan. 2010.

18. F. Melo *et al.* "Experimental evidence of shock mitigation in a Hertzian tapered chain," *Phys. Rev. E*, vol. 73, pp. 041305, May 2006.

19. P. Zhang and A. C. To, "Broadband wave filtering of bioinspired hierarchical phononic crystal," *Appl. Phys. Lett.*, vol. 102, pp. 121910, March 2013.

20. M. Redwood, "Transient performance of a piezoelectric transducer," *J. Acoust. Soc. Am.*, vol. 33, no. 4, pp. 527-536, April 1961.

21. A. W. Stepanow, "Über den Mechanismus der plastischen Deformation," *Zs. Phys.*, vol. 81, no. 560, Jan 1933.

22. W. J. Halpin, "Current from a shock-loaded short-circuited ferroelectric ceramic disk," *J. Appl. Phys.*, vol. 37, no. 1, pp. 153-163, Jan. 1966.

23. O. M. Stuetzer, "Secondary stresses in a stress-pulse-activated piezoelectric element," *J. Appl. Phys.*, vol. 38, pp. 3901-3904, May 1967.

24. D. Lobdell, "Comment upon 'Secondary stresses in a stress-pulse-activated piezoelectric element' by O. M. Stuetzer," *J. Appl. Phys.*, vol. 39, pp. 2975, 1968.

25. P. C. Lysne, "One-dimensional theory of polarization by shock waves: application to quartz gauges," *J. Appl. Phys.*, vol. 43, pp. 425, Feb. 1972.

26. P. J. Chen and L. Davison, "Electrical response of nonlinear piezoelectric materials," *J. Appl. Phys.*, vol. 47, pp. 4759, 1976.

27. G. E. Duvall, "The shocked piezoelectric disk as a Maxwell solid," *J. Appl. Phys.*, vol. 48, pp.4415, 1977.

28. P. C. Lynse, "Shock induced polarization of a ferroelectric ceramic," *J. Appl. Phys.*, vol. 48, pp. 1024, 1977.

29. W. Ani and A. Maugin, "Basic equations for shocks in nonlinear electroelastic materials," *J. Acoust. Soc. Am.*, vol. 85, pp. 599, 1989.

30. J. Fish and W. Chen, "Modeling and simulation of piezocomposites, *Comp. Methods in Appl. Mech. Eng.*, vol. 192, pp. 3211-3232, July 2003.

31. D. A. Hopkins and G. A. Gonzalas, "Wave propagation in second order nonlinear piezoelectric media," Army Research Lab., Aberdeen Proving Grounds, MD, No. ARL-TR-5766, 2011.

32. G. A. Gonzalas, R. A. Wildman, and D. A. Hopkins, "Elastodynamic impact into piezoelectric media," Army Research Lab., Aberdeen Proving Grounds, MD, No. ARL-TR-7056, 2014.

33. A. C. Robinson *et al.* "ALEGRA: An arbitrary Lagrangian-Eulerian multimaterial, multiphysics Code," in *AIAA Aerospace Science Meeting and Exhibit,* Reno, NV, 2008.

34. J. A. Mitchell and T. J. Fuller, "Nonlinear kinematics for piezoelectricity in ALEGRA-EMMA," Sandia National Labs., Albuquerque, NM, SAND-2013-7363, 2013.

35. C. H. Sherman and J. L. Butler, *Transducers and Arrays for Underwater Sound*. New York: Springer-Verlag, 2007.

36. NDT Resource Center. *Acoustic properties for metals in solid form* [Online]. Available: www.nde-ed.org/GeneralResources/MaterialProperties/UT/ut_matlprop_metals.htm

37. NDT Resource Center. *Acoustic properties for metals in solid form* [Online]. Available: www.nde-ed.org/GeneralResources/MaterialProperties/UT/ut_matlprop_piezoelectrics.htm

38. D. A. Berlincourt, H. H. A. Krueger, and C. Near, "Properties of piezoelectric ceramics," MorganElectro Ceramics, Technical Publication 226, 1999.

39. R. K. Linde, "Depolarization of ferroelectrics at high strain rates," *J. Appl. Phys.*, vol. 38, no. 12, pp. 4839-4842, Nov. 1967.

40. S. I. Shkuritov, E. F. Talantsev, and J. Baird, "PZT 52/48 ferroelectric ceramics: Depolarization and electric breakdown under longitudinal explosive shock," Pulsed Power Conf., Chicago, IL, 2011.

41. S. Zhang and T. R. Shrout, "Relaxor-PT single crystals: observations and developments," *IEEE Trans. Ultrason. Ferroelectr. Freq. Control,* vol. 57, pp. 2138-46, Oct. 2010.

42. R. Zhang *et al.* "Elastic, dielectric and piezoelectric coefficients of domain engineered 0.70Pb(Mg1/3Nb2/3)O3-0.30PbTiO3 single crystal," *AIP Conf. Proc.*, vol. 626, pp. 188, August 2002.

3 Strain-rate dependence of PZT 52/48 and PZT 95/5 under low and intermediate loading rate

3.1 Introduction

The ferroelectric ceramic lead zirconate titanate (PZT) has been utilized for its piezoelectric properties as well as its ability to rapidly depolarize under shock compression, which can be harvested to produce a large, one time electrical pulse.[1] There are two popular types of ceramic PZT based on the Zirconate/titanate ratio, PZT 52/48 and PZT 95/5. Many characteristics, including the crystal structure, dielectric response, and piezoelectric response, are a direct result of the zirconate/titanate ratio. PZT 52/48 resides on the morphotropic phase boundary,[2] where many of the electromechanical properties are enhanced. PZT 95/5 lies on a phase boundary between a ferroelectric (FE) phase and an antiferroelectric (AFE) phase, allowing for a pressure-induced FE to AFE phase transformation.[3]

A transient acoustic wave will propagate through PZT at the speed of sound, ~ 4350 m/s, generating electric fields within the material due to the piezoelectric effect. If a propagating wave is of sufficient magnitude in axial stress, it can drive the collinear dipoles to rotate normal to the poling (and shock) direction. This so-called 90° domain switching process is a common depoling mechanism for PZT 52/48. Alternatively, PZT 95/5 will undergo both domain switching and a ferroelectric-to-antiferroelectric phase transformation starting at around 500 MPa.[4] As the ferroelectric depoles the recently freed charges on the electrodes can be harvested by connecting the PZT in series with a resistive or capacitive load. If the charge is not released, electrical breakdown across the ferroelectric will occur due to the newly formed fracture surfaces within the material.

There has been a great deal of work done on the shock depoling of ferroelectric PZT using plate impact experiments, which carry uniaxial strain rates on the order of 10^6/s. Most of the shock research revolves around PZT 95/5 as a result of the material's greater remnant polarization

value, and thus the larger amount of charge held on the electrodes. PZT 95/5 depoles using two different mechanisms. At lower pressures, 90° domain switching plays a dominant role on the partial depolarization of the ferroelectric. At higher pressures starting at about 500 MPa, the ferroelectric undergoes a phase transformation from the FE rhombohedral phase to the AFE orthorhombic phase, resulting in a 0.9% volume reduction[2] and complete depoling of the ferroelectric. The shock response of both PZT 52/48 and 95/5 has been investigated in the unpoled state, axial poled, and transversely (normal) poled state under both low and high field conditions.

There has been considerably less work performed regarding the response of these materials under low and intermediate dynamic loading, mainly due to the ceramic's brittle nature. Nevertheless, intermediate loading rates on the order of 1-10 MPa/μs have been achieved using a pulsed laser system, drop weight tower, and a split Hopkinson pressure bar (SHPB).[5] With careful experimental control, the SHPB can been used to investigate the dynamic mechanical loading behavior of ceramics.[6-8] Hao-Sen and colleagues used a SHPB for dynamic fracture toughness measurements of PZT, covering a loading range from 0.4 to 0.6MPa/μs.[7] Their results showed that the dynamic fracture toughness was 8–12 times greater than the static fracture toughness. Wang and Liu investigated the dynamic response of PZT 52/ 48 with a modified SHPB, which allowed for additional hydrostatic pressure.[10] Strain rates from 500/s to 900/s were achieved at hydrostatic pressures up to 15MPa, for a max stress of 963 MPa. They saw an increase in fracture strength with increasing hydrostatic pressure and strain rate. Hard PZT-4, which has a composition around $(Pb_{0.94}Sr_{0.06})(Zr_{0.53}Ti_{0.47})O_3$[11] as used by Dong and colleagues for uniaxial stress experiments in a SHPB with loading rates from 3.3 to 4.0MPa/ms.[12] It was found that PZT-4 is significantly rate sensitive, showing an apparent ''rate hardening'' effect. The switching stress

increased from 10 MPa for a rate of 1MPa/s up to 56MPa for a rate of 4 MPa/μs, showing a six-fold increase of switching stress over six decades of loading rate.

In order to investigate the depolarization dependence on mechanical loading rate of PZT 52/48 and 95/5, intermediate loading-rate experiments were performed using a SHPB. We observe significant rate sensitivity in PZT 52/48. By comparison, PZT 95/5 was found to be less rate sensitive; instead displaying a jump in depolarization stress at loading rates around 50–60 MPa/μs.

3.2 Procedure: Load Frame & Split-Hopkinson Pressure Bar Experiments

Ceramic PZT 52/48 and 95/5 ranging from 0.55-0.89 mm in thickness were diced into 7.7±4.0 mm^2 square samples using a DISCO diamond cutting saw. Gold electrodes were deposited on the top and bottom surfaces using chemical vapor deposition. Each sample was then poled in the thickness direction using a 2 MV/m electric field at a 200 mHz frequency. The average remnant polarization was 0.33 C/m^2 for PZT 52/48 and 0.34 C/m^2 for PZT 95/5.

The samples were placed between two hardened steel platens. Electrical leads were attached to the steel platens in order to record the depolarization of the samples. Kapton tape (120 μm thick) was used on the outside of the steel platens to electrically isolate the sample and platens from the environment. An alignment fixture[13] was used to mitigate any tilt in the system to ensure conditions as close to uniaxial stress as possible. In addition, a thin layer of vacuum grease was used between the steel platens and the sample in an attempt to minimize lateral clamping and thus fracture of the sample under Poisson expansion. Three different current viewing resistances were chosen to keep the depoling voltage under 10 V.

Samples were then loaded into an Instron biaxial load frame, with the loading direction congruent with the polarization direction. A pre-stress of ~5 MPa was added to align the sample.

The samples were loaded at a constant rate while the stress and depolarization data was collected. The stress rate and constancy was confirmed by analyzing the stress history. Additional samples of PZT 95/5 were prepared and tested with the polarization normal to the loading direction as well. A schematic of the load frame and circuit are shown in figure 3.1, while experimental parameters can be seen in table 3.1.

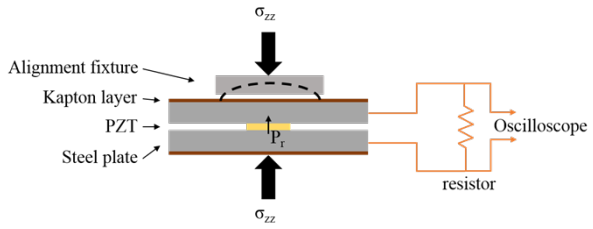

Figure 3.1: Schematic of load frame arrangement and current viewing circuit.

Table 3.1: Load frame experimental parameters.

PZT type	Surface area (mm^2)	Thickness (mm)	Loading rate (MPa/ms)	Resistor (kΩ)
52/48	8.94	0.73	0.56	98.9
52/48	11.15	0.73	4.48	98.9
52/48	10.14	0.73	9.86	17.6
52/48	10.20	0.73	49.0	0.98
52/48	10.97	0.73	91.2	0.98
95/5	11.7	0.55	0.43	98.9
95/5	5.16	0.55	1.94	98.9
95/5	6.53	0.55	7.66	98.9
95/5	6.53	0.55	15.3	17.6
95/5	5.58	0.55	89.6	0.98
95/5	11.60/3.7*	0.89	8.62	98.9

*For transverse mode tests, the first surface area is used to calculate the stress and the second is used to calculate the charge density.

Dynamic uniaxial stress compression of axially poled PZT 52/48 and 95/5 was performed using a SHPB. The SHPB (Figure 3.2) consisted of an incident bar and transmitted bar, both equipped with strain gauges. The stress in the bars was kept below the elastic limit. This enabled direct determination of stress from the measured bar strain. The incident, transmitted, and reflected stress waves were measured. The length and material properties of the striker bar that was driven into the incident bar set the width of the incident impulse. The pressure used to launch the striker bar set the maximum amplitude of the impulse. A copper disk was attached to

the striking face of the incident bar to shape the pulse, increasing the rise time and providing a region of constant strain rate (Figure 3.2). The loading rate details and SHPB parameters can be found in Table 3.2.

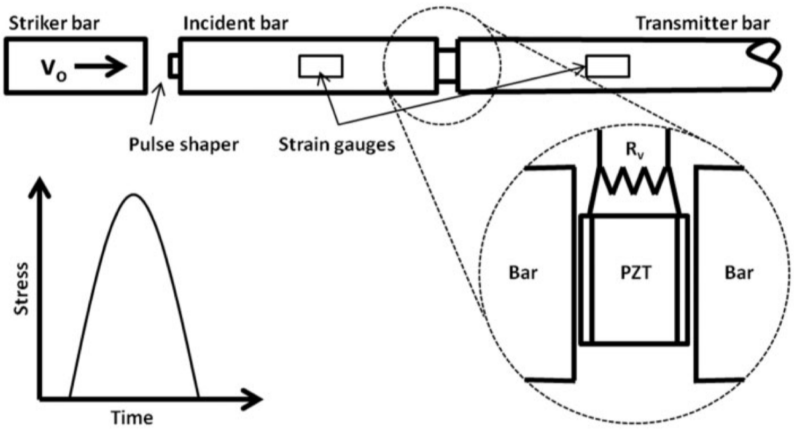

Figure 3.2: Schematic of a split Hopkinson pressure bar (top) with specimen (insert) and schematic impulse (bottom left).

Figure 3.2: SHPB experimental parameters.

Loading rate	
Range (MPa/μs)	7.2–92.5
Max (MPa)	900
Bar parameters	
Elastic modulus (GPa)	192.44
Poison's ratio (–)	0.31
Speed of sound (mm/μs)	4.8655
Bar diameter (mm)	18.9

Commercial PZT 52/48 (TRS 200) and PZT 95/5 ceramics were obtained from TRS Technologies. Electrically conducting copper tape was attached to each electrode. A viewing resistor was soldered to the copper tape, and Kapton tape was used to electrically isolate each specimen from the bars. Electrical leads were attached across the viewing resistor and connected to a digital potentiometer. A schematic of the specimen setup can be seen in Figure 3.3. The specimen dimension, remnant polarizations, and viewing resistance are listed in Table 3.3.

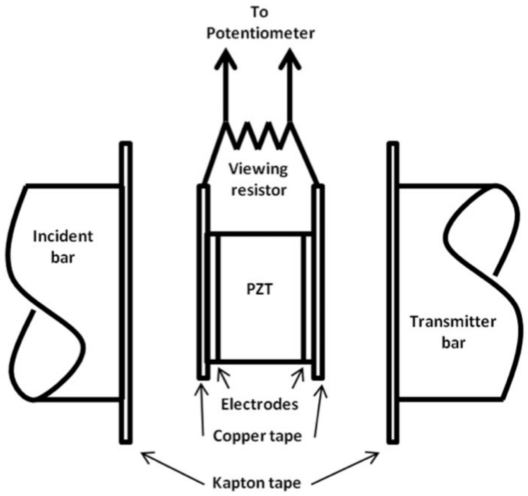

Figure 3.3: Specimen configuration within the SHPB. Kapton tape insulates the sample from the steel bars. Copper tape completes the circuit of the PZT sample and viewing resistor.

Table 3.3: Specimen parameters.

Specimen parameters	PZT 52/48	PZT 95/5
Diameter (mm)	12.5	12.5
Thickness (mm)	3.18	3.18
Remnant polarization (C/m^2)	0.32 ± 0.02	0.35 ± 0.05
Viewing resistance (Ω)	1.0	

3.3 Results: Low Loading Rate Experiments

Figure 3.4 shows the stress and released charge density histories recorded during two typical compression experiments using the load frame. The constancy of the loading rate for each experiment was verified by the recorded stress history. Figure 3.5a shows the charge density as a function of stress for PZT 52/48 at several different loading rates. The charge density rises rapidly on the application of pressure from 0 to 100 MPa, curve in a transition zone of pressure from 100-500 MPa, and then saturate from 500 MPa onward. While the charge density of one sample (0.56 MPa/ms) reaches the remnant polarization value of 0.33 C/m^2, the other samples reach about 85% of this value, indicating incomplete depolarization of the ferroelectric. Figure 3.5b shows the

charge density as a function of stress for PZT 95/5 at several different loading rates. The charge density rises rapidly on the application of pressure from 0-300 MPa, curve in a transition zone of pressure from 300-900 MPa, and then saturate from 900 MPa onward (although only two samples survived stresses greater than 1200 MPa.)

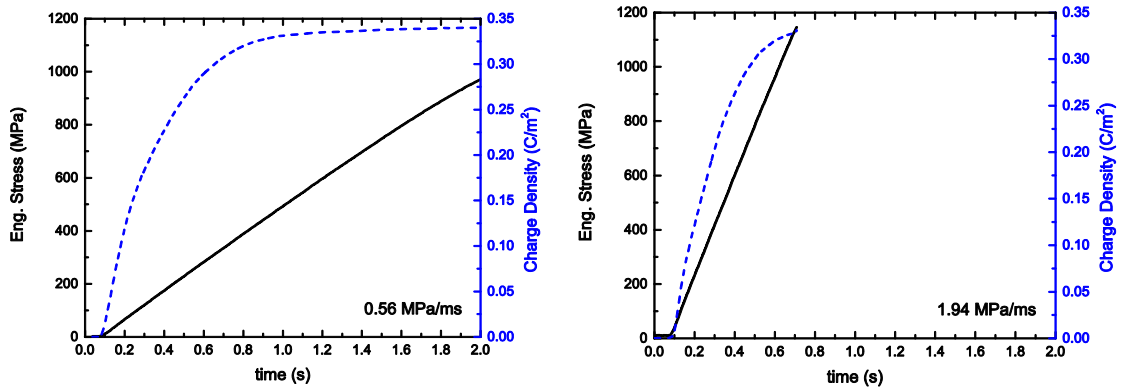

a b

Figure 3.4: Stress and depolarization history for PZT 52/48 at 0.56 MPa/ms (a) and PZT 95/5 at 1.94 MPa/ms (b).

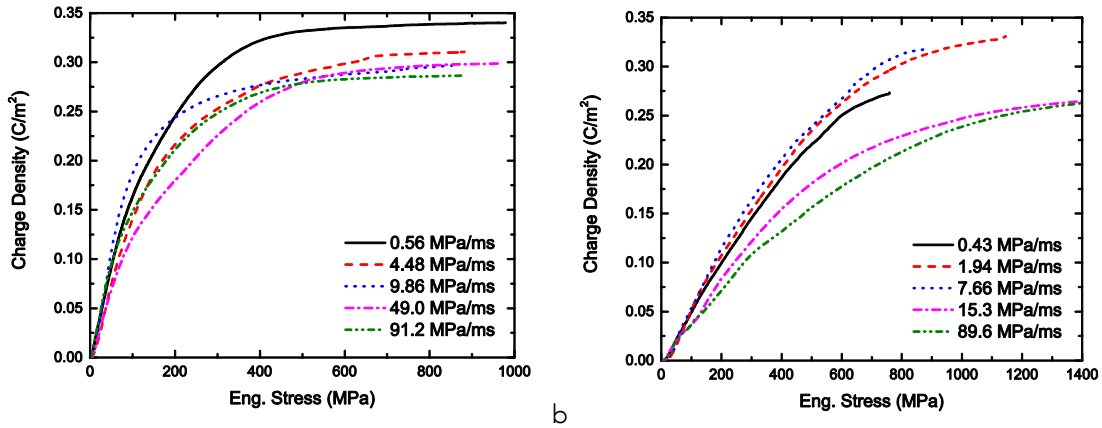

a b

Figure 3.5: Depolarization of PZT 52/48 (a) and PZT 95/5 (b); depolarization charge density as a function of stress for various loading rates.

Figure 3.6 shows a typical stress and charge density history for PZT 95/5 loaded in the transverse (normal to poling) direction. Since the ferroelectric dipoles now face perpendicular to the applied stress, they undergo a positive strain due to Poisson expansion. The charge density

then drops due to the piezoelectric effect in the pressure range from 50-350 MPa. From 350-500 MPa the charge density gradually rises back to zero due to competing mechanisms. At 500 MPa there is a rapid jump in released charge density that coincides with a disturbance in the stress history, both of which could be explained by the onset of a partial FE-AFE phase transformation. The charge density saturates at a sixth of the remnant polarization value, most likely due to electrical shorting due to lateral cracks through the ceramic. Because the FE-AFE phase transformation induces a 0.9% volume reduction, a partial phase transformation could cause internal stresses leading to crack propagation.

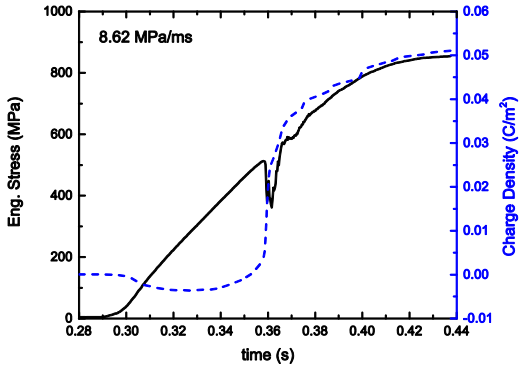

Figure 3.6: Stress and depolarization history for PZT 95/5 under the normal mode at 8.62 MPa/ms.

3.4 Discussion: Low Loading Rate Experiments

No clear trend for the rate dependence of the depolarization kinetics could be identified in the loading rate regime of 1-100 MPa/ms, however some general observations should be noted. The depolarization charge density values for both PZT 52/48 and 95/5 were usually 70-85% of the expected remnant polarization value, which could indicate incomplete depolarization of the ferroelectric. The stress value at which the charge density begins to saturate is roughly twice as large for PZT 95/5 (900 MPa) than for PZT 52/48 (500 MPa). The difference is depolarization stress is most likely due to different depolarization mechanisms, where 90° domain switching

would occur in both varieties of PZT, the 95/5 version additionally can undergo an FE-AFE phase transformation. As such, additional experiments were performed where PZT 95/5 samples were loaded in a direction normal to the polarization direction.

3.5 Results: Intermediate Loading Rate Experiments

The electrical response of mechanically loaded, axially poled PZT 52/48 and 95/5, along with the incident, transmitted, and reflected strain signals were recorded as a function of time. Figure 3.7 shows the stress pulse and released surface charge density as a function of time for a typical experiment. The charge density is the amount of charge liberated from the surface electrodes due to mechanical depolarization. Once this charge is lost, the electrodes maintain their charge state until further depoled or repoled by the application of a sufficient electric field. As the FE undergoes uniaxial stress loading, the crystals change variants through 90° domain switching. The stress field induces domain wall motion to decrease the domains with polarization parallel to the axis of compression. The rate at which this occurs is dependent upon the kinetics of variant evolution. Such kinetics includes the nucleation and growth of new domains, which are both thermally activated processes. The domain wall motion itself can be a function of the underlying driving force. Furthermore, frictional and viscous forces associated with various charged defects can act to hinder wall mobility.[14]

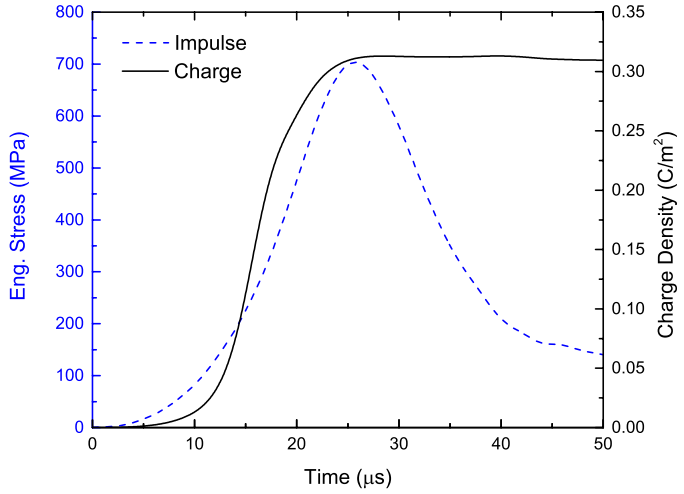

Figure 3.7: Depolarization charge density and stress pulse as a function of time for PZT 95/5 at 50.7 MPa/μs.

Nevertheless, under sufficient mechanical loading the material undergoes ferroelastic deformation, and charge that was once bound at the surface of the electrodes is released across the viewing resistor. Integrating the voltage response of the viewing resistor and dividing by the resistor value yields the total released charge. If sufficient stress is applied, the ceramic can be nearly fully depoled, indicated by the released surface charge density approaching the remnant polarization value of approximately 0.32–0.35 C/m^2.

Figure 3.8 illustrates the mechanically induced depolarization process. The curve can be characterized by dividing it into three regimes; an initial range up to 0.025 C/m^2 with a relatively linear response, a middle range from roughly 0.025–0.25 C/m^2 characterized by a substantially steeper slope, and a final range characterized by a decrease in slope. It is believed that this initial range is dominated by the piezoelectric effect, a combination of lattice deformation and an extrinsic contribution associated with some domain wall motion. The intermediate range is

dominated by large-scale 90° domain wall motion. During the final range, the 90° domain wall motion reaches saturation.

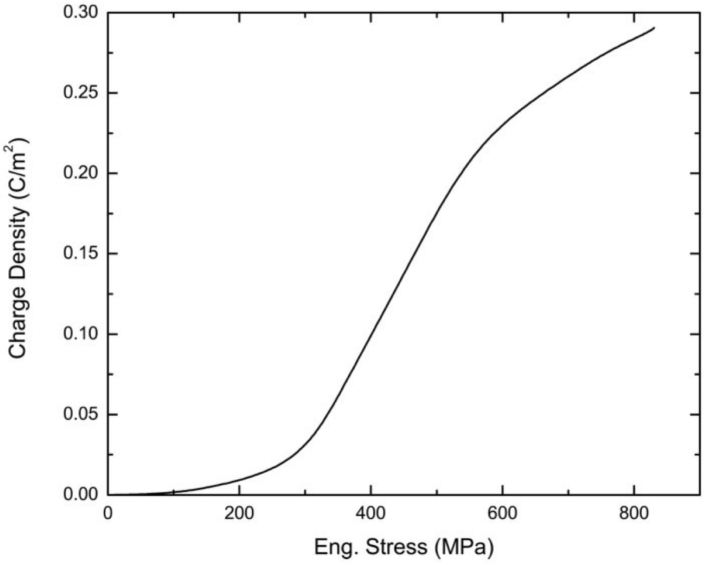

Figure 3.8: Charge density as a function of stress for PZT 95/5 at 81.2 MPa/μs.

The power generated by the PZT sample is a product of both the resistance of the load on the circuit and the square of the released current. The maximum current is a function of the material dependent remnant polarization, the fraction of depolarization, and the depolarization time. The depolarization time is dependent on the sample thickness and the stress impulse within the sample, as seen in Figure 3.7. The current is transient and therefore provides only a few microseconds of power, requiring an oscilloscope with gigahertz resolution. The maximum power is also dependent on the load resistance, with the limiting factor being dielectric breakdown across the PZT ceramic.[15] Here, we use a 1.0 Ω viewing resistor to enable an essentially short circuit boundary condition across the sample, while simultaneously ensuring a proper voltage for our measuring oscilloscope. A short circuit configuration reduces the chance of dielectric breakdown while providing information on the short-circuit depolarization kinetics.

Figure 3.9a shows the depolarization charge density as a function of stress and stress rate for PZT 52/48. The mechanical depolarization rate sensitivity of PZT 52/48 follows the trend observed by Dong and colleagues with PZT-4,[12] where higher loading rates increased the depolarization stress. Similar behavior may be expected since both ceramic compositions are near the morphotropic phase boundary. Figure 3.9b shows the depolarization charge density as a function of stress for PZT 95/5. The response of PZT 95/5 displays the same three depolarization regimes as seen in PZT 52/48, even at high loading rates. In addition, all of the samples had lost at least 50% of their polarization by the time the stress reached the uniaxial phase transformation starting pressure. Based on this, we conclude that domain switching was the primary driving force behind the depolarization of the PZT 95/5 samples.

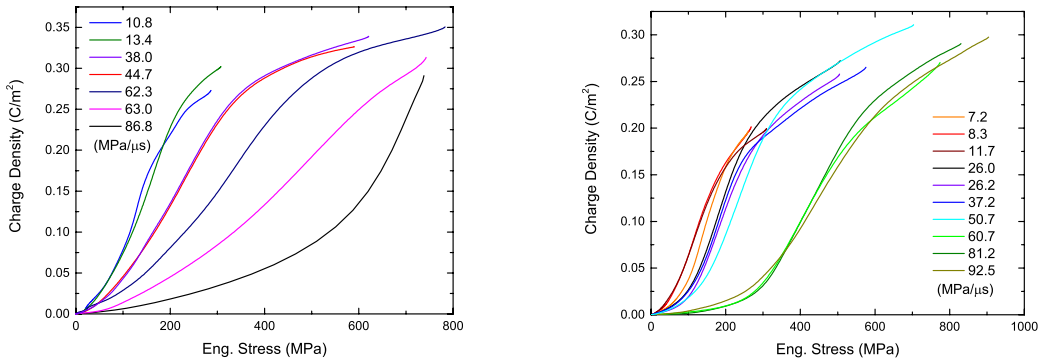

a b

Figure 3.9: Depolarization charge density of PZT 52/48 (a) and PZT 95/5 (b) as a function of stress for various loading rates. Increasing loading rate drastically changes the depolarization stress in PZT 52/48 compared to PZT 95/5.

3.6 Discussion: Intermediate Loading Rate Experiments

In contrast to PZT 52/48, the mechanical depolarization of PZT 95/5 shows little rate dependence. This may be explained due to differences in the domain switching kinetics reported for the two compositions. Domain wall motion has been suggested to be hindered by charged point defects in much the same way dislocations can become pinned in ductile materials. In PZT

52/48, the 90° wall motion is hindered by Ti or Zr vacancies.[2] Donor doping with Nb^{5+} on the B-site cations create A- and B-site vacancies in order to ensure charge neutrality.[16] The charged dipole vacancy defects are relatively immobile, and are believed to cause frustration in the domain structure.[16,17] These frustrations act to lower the energy barrier for domain wall motion by destabilizing the domains,[18] while at the same time act as an internal source of friction against wall motion.[17,18] Immobile dipole defects may also be the cause of viscous effects on domain wall motion, and have been explained by a dragging-depinning process. While oxygen vacancies are less prevalent in donor-doped PZT, those present may likewise add to both frictional and viscous effects.[18]

The PZT 52/48 used in these experiments is a Navy type II, PZT 5A, which is a soft PZT doped with Nb^{5+} in order to increase the dielectric and piezoelectric constants. PZT 95/5 is likewise doped with Nb^{5+} in order to increase stability of the FE phase. However, the ideal doping concentration for both compositions is around 2%,[14] suggesting that the effects of donor doping should be similar for both materials. Still, charged defects could play a role in the difference in depolarization kinetics on the basis of domain wall drag.

Another possible explanation for the difference in depolarization kinetics stems from the nature of the domain switching. The morphotropic phase boundary at the 52/48 composition is not a sharp boundary, but rather a mixture of tetragonal and monoclinic phases. In this regime, the domain switching is characterized by the stress-induced rotation of the monoclinic polar axis.[19] Conversely, domain switching in PZT 95/5 is largely though to obey the same 90° switching mechanisms seen in other FEs, where ionic displacements occur along the principle polarization axes. For PZT 95/5, these axes are along the <111> directions of the rhombohedral phase.[20] Such differing domain switching mechanisms may likewise play a role in the stress rate dependencies of the two material systems. The jump in depolarization stress for loading rates above 50–60

MPa/μs is suspected to arise due to different depolarization mechanisms. At lower stress rates, the depolarization rise time appears to coincide with the stress rise time, suggesting that the stress amplitude drives the rate at which the domain wall sweeps a domain. Yet at stress rates above 50–60 MPa/μs, the depolarization rise time is significantly longer than the stress rise time. It is unlikely that the split is due to the onset of the FE to AFE phase transformation, since the difference in depolarization is significant even below the uniaxial stress phase transformation pressure.[21] Furthermore, Fritz has suggested that domain switching is the dominant depolarization mechanism for PZT 95/5 under uniaxial stress in this pressure range, and found no evidence of the FE to AFE transformation.[22] It may be more likely that these higher stress rates are surpassing the rate at which the domain walls can sweep through the domains. If this were the case, one would expect to see the depolarization rise time saturate at a constant value with increasing stress rate. However, it appears that the depolarization rise time varies linearly with the stress rise time at these higher rates as well, providing the relatively stress rate independent response. Uniaxial stress compression experiments under different temperatures and utilizing volumetric strain measurements may help elucidate the cause of this phenomena.

3.7 Conclusion

The mechanical loading rate dependence on depolarization for PZT 52/48 and PZT 95/5 was investigated in the loading range of 0.1-100 MPa/ms, with a maximum stress up to 1 GPa for PZT 52/48 and 1.4 GPa for PZT 95/5 by using a load frame. Neither PZT 52/48 nor PZT 95/5 exhibited a strong rate dependence of depolarization in the range studied. The released charge density of PZT 52/48 saturated at ~500 GPa, while PZT 95/5 required twice the pressure for the saturation of polarization. Since the saturated charge density for both types of PZT is lower than their remnant polarization value, the materials may not have been fully depoled. Depolarization

behavior of both types of PZT is dominated by domain switching. The transverse loading experiments indicated that the phase transformation likely contributed to the depolarization response of PZT 95/5.

The mechanical loading rate dependence on the depolarization of PZT 52/48 and 95/5 was investigated in the loading range of 7.2 to 92.5 MPa/μs, with a maximum stress of around 900MPa using a SHPB. PZT 52/48 showed significant rate sensitivity, while PZT 95/5 was relatively rate insensitive. However, PZT 95/5 displayed a jump in depolarization stress for loading rates above 50–60MPa/μs. These results illustrate the importance of considering rate dependencies on the nonlinear electromechanical behavior of piezoelectric ceramics, and may be important for the design of active composites that sense and harvest energy from impact events.

3.8 References

1. W. Mock and W. H. Holt, "Pulse charging of nanofarad capacitors from the shock depoling of PZT 56-44 and PZT 95/5 ferroelectric ceramics," *J. Appl. Phys.,* vol. 49, pp. 5846–54, 1978.

2. I. J. Fritz and J. D. Keck, "Pressure-temperature phase diagrams for several modified lead zirconate ceramics," *J. Phys. Chem. Solids*, vol. 39, pp. 1163–1167, 1978.

3. P. C. Lysne and C. M Percival, "Electric energy generation by shock compression of ferroelectric ceramics: normal- mode response of PZT 95/5*," *J. Appl. Phys.* vol. 46, pp. 1519–25, April 1975.

4. L. C. Chhabildas, "Dynamic shock studies of PZT 95/5 ferroelectric ceramic," Sandia National Labs., Albuquerque, NM, SAND-84-1729, 1984.

5. I. Chasiotis and J. Lambros, "Dynamic failure of multi-layer MEMS at high loading rates: experiments and simulations," Ft. Belvoir, VA: Final Report for the U.S. Army Research Office. University of IL, Report no. 48421-EG.3, 2008.

6. J. M. Staehler *et al.* "Testing of high-strength ceramics with the split Hopkinson pressure bar," *J. Am. Ceram. Soc.* vol. 76, pp. 536–538, 1993.

7. W. Chen and H. Luo, "Dynamic compressive responses of intact and damaged ceramics from a single split Hopkinson pressure bar experiment," *Exp. Mech.* vol. 44, pp. 295–299, 2004.

8. J W. McCauley and G. D. Quinn, "Special workshop: Kolsky/ split Hopkinson pressure bar testing of ceramics," Report, Army Research Labs., Aberdeen Proving Ground, MD, Report no. ARL-SR-144, 2006.

9. C. Hao-Sen *et al.*, "Dynamic fracture toughness of piezoelectric ceramics," *J. Am. Ceram. Soc.* vol. 96, pp. 2036–38, 2013.

10. S. Wang and K. X. Liu, "Experimental research on dynamic mechanical properties of PZT ceramic under hydrostatic pressure," *Mater. Sci. Eng. A*, vol. 528, pp. 6463–68, 2013.

11. C. A. Randall *et al.*, "Intrinsic and extrinsic size effects in fine-grained morphotropic phase boundary lead zirconate titanate ceramics," *J. Am. Ceram. Soc.* vol. 81, pp. 677–688, 1998.

12. X. Dong *et al.*, "Rate dependence of domain switching in PZT under static and dynamic compressive loading," *J. Phys. IV France,* vol. 134, pp. 989–994, 2006.

13. H. Cao and A. G. Evans, "Nonlinear deformation of ferroelectric ceramics," *J. Am. Ceram. Soc.,* vol. 76, pp. 890–896, 1993.

14. L. L. Altgilbers, *et al.*, *Explosive pulsed power*, 1st ed. Covent Garden, London: Imperial College Press, 2011, pp. 369–439.

15. S. I. Shkuratov, *et al.* "Depolarization mechanisms of $PbZr_{0.52}Ti_{0.48}O_3$ and $PbZr_{0.95}Ti_{0.05}O_3$ poled ferroelectrics under high strain rate loading," *Appl. Phys. Lett.*, vol. 104, pp. 212901, 2014.

16. A. Moulson and J. Herbert, *Electroceramics: materials, properties, applications*, 2nd ed. Hoboken, NJ: John Wiley, 2003, pp. 362.

17. E. M. Bourim *et al.*, "Domain wall motion effect on the anelastic behavior in lead zirconate titanate piezoelectric ceramics," *J. Appl. Phys.*, vol. 91, pp. 6662, 2002.

18. Q. M. Zhang *et al.*, "Change of the weak- field properties of $Pb(ZrTi)O_3$ piezoceramics with compressive uniaxial stresses and its links to the effect of dopants on the stability of the polarizations in the materials," *J. Mater. Res.*, vol. 12, pp. 226–234, 2011.

19. R. Guo *et al.*, "Origin of the high piezoelectric response in $PbZr_{1-x}Ti_xO_3$," *Phys. Rev. Lett.*, vol. 84, pp. 5423–5426, 2000.

20. J. C. Valadez Perez, "Characterization and modeling of ferroelectric materials for high pressure, high temperature applications," PhD dissertation, Mech. Aero. Eng., UCLA, Los Angeles, CA, 2012.

21. D. H. Zeuch, S. T. Montgomery and D. J. Holcomb, "Uniaxial compression experiments on lead zirconate titanate 95/5-2Nb ceramic: evidence for an orientation-dependent, 'maximum compressive stress' criterion for onset of the ferroelectric to antiferroelectric polymorphic transformation," *J. Mater. Res.*, vol. 15, pp. 689–703, 2000.

22. I. Fritz, "Uniaxial-stress effects in a 95/5 lead zirconate titanate ceramic," *J. Appl. Phys.*, vol. 49, pp. 4922–4928, 1978.

4 Shock Response of Multilayered Ferroelectric Composites

4.1 Introduction

Shock mitigation systems that utilize smart materials expand the array of mitigation mechanisms that can be incorporated into system design. Ferroelectrics (FEs) have been proposed as a sensing and power-generating component of these systems. The shock wave produced by impact can depole a FE ceramic and produce a significant, one-time pulse of current.[1] The depoling mechanism can be attributed to domain switching or, in the case of lead zirconate titanate with a Zr:Ti ratio of 95:5 (PZT 95/5), a ferroelectric to antiferroelectric (FE-AFE) phase transformation. In either case, the electrical pulse travels at the electromagnetic wave speed, while the shock wave travels at speeds on the order of the speed of sound in the material. In a composite material consisting of a FE power-generating layer and a shock wave mitigating composite layer, the electrical pulse can propagate ahead of the shock wave. This can act as a signal for impact detection and a power source for mitigation techniques.

Of the mitigation techniques available, one obvious choice is to simply use another ferroelectric layer. Piezoelectrics undergo a change in effective stiffness under different electrical boundary conditions. For PZT 5A, the elastic modulus changes from 147 GPa under open circuit conditions, to 111 GPa under short circuit (SC) conditions.[2] A more complicated situation arises under shock loading, where secondary tensile stresses can develop in the yet-unshocked region of the short-circuited piezoelectric, dropping the stress at the shock front.[3] These piezoelectric effects may dominate at lower-pressures. At higher-pressures, ferroelectrics undergo either domain switching or phase transformations that can also alter the material's mechanical response. Of particular interest is the FE-AFE phase transformation in PZT 95/5 when subjected to pressures above 500 - 600 MPa.[4,5] The electrical boundary conditions, which are typically controlled by including a series resistance in the ferroelectric circuit, act to alter the phase

transformation kinetics and resulting shock wave profile by introducing large electric fields within the ferroelectric. Valadez explored the effect of electric field on phase transformation pressure for PZT 95/5, detailing how the FE-AFE phase transformation is dictated by competing forces of long-range and short-range order.[6] The electric field favors long range order (the FE phase), while the pressure favors short-range order (the AFE phase). Dick and Vorthman reported a 12% reduction in final particle velocity in shock loaded, normally poled PZT 95/5 under high field conditions.[7] They suggested that the presence of an electric field could hinder both domain switching and the phase transformation from a free energy perspective. Dai et al. suggested that the transformation pressure of shock-compressed PZT 95/5 shift with the relation in equation 4.1.

$$P_S = 4.5 \cdot 10^6 \cdot E + P_0 \qquad \text{(Eq. 4.1)}$$

Here P_s is the critical phase transformation pressure, E is the electric field (kV/cm) within the mixed transformation region, and P_0 is the critical transformation pressure at zero field (Typically 300 MPa).[8] Setchell et al. found that altering the electrical boundary conditions for normally poled PZT 95/5 shock loaded to 0.9 and 2.4 GPa resulted in distinct changes on the shock front profile, but not final state velocities.[9] A slight decrease in wave speed under high field conditions was also reported. Zeuch noted that in one of their constant-stress-difference loading experiments on PZT 95/5, the transformation pressure was anomalously high, which they said may be attributed to the electrical boundary conditions.[10] Jaing extended this work by shocking normally poled PZT 95/5 under a variety of resistive loads, plotting the degree of transformation and transformation rate for a variety of electric field values. Incorporating other author's data as well, they showed that the electric field can reduce the degree at which the phase transformation occurs by nearly 20%, but only at shock pressures below ~ 1 GPa.[11]

The aforementioned work suggests that the electrical boundary conditions considerably affect the shock response in poled PZT 95/5 due to the hindering of the FE-AFE phase transition

under high field. However, the choice of composite geometry is essential in maximizing these effects. Recent work with impedance-mismatched layered composites has shown promise in dissipating the shock energy through wave scattering off impedance-mismatched interfaces. The shock wave reflects off the impedance-mismatched interfaces, creating complex wave front interactions that slow the wave and dissipate the shock energy. Zhuang et al. characterized layered composites via shock loading using a 36 mm powder gun. These composites were comprised of polycarbonate and one of three materials: steel, aluminum, or glass. The resulting shock wave modification indicated that that the shock wave underwent scattering off the impedance-mismatched interfaces in such a way that both the bulk and deviatoric response was greatly modified.[12] The influence of scattering on the bulk response acted to reduce the wave speed of the shock wave, in some cases below the velocity of the bulk constituents. The influence of the deviatoric response resulted in structuring the shock front by increasing the shock front rise time similar to the effect of viscous material behavior in homogenous solids. They found that the shock front strain rate increased with the square shock stress, compared to the fourth power as seen in most homogeneous materials. Therefore, the effect on the deviatoric response was to increase the effective shock viscosity. The shock viscosity was found to increase with interface impedance mismatch, and decrease with larger interface density and loading amplitude. The periodic layered structure also resulted in an oscillatory late-time shock profile, possibly contributing to shock energy dissipation. An increase in shock loading resulted in an increase in the amplitude of oscillations, which implied that more of the kinetic energy had been transformed to internal energy and that the dissipation of shock energy had increased. Lastly, it was found that the existing mixture theories could reasonably predict the bulk response behavior of the mixtures to shock compression, but were incomplete when describing the deviatoric response.

Chen et al. provided an analytical solution to shock loading of heterogeneous composited by utilizing Floquet's theory of ordinary differential equations with periodic coefficients.[13] They found that the mean stress could be reasonably approximated using a superposition of wave trains or by using Dremin's mixture theory. Additionally, for some material combinations, the mean stress could be significantly higher than the value at time of impact. Chen et al. found that the mean stress decreased with time, attributed to some time-dependent dissipation mechanism.[14] An increase in impedance mismatch was found to increase the rise time, increase the late-time oscillations, lower the effective wave speed, and lower the oscillation frequency. Increasing interface density was found to lower rise time, increase oscillation frequency, and resulted in a higher peak stress due to shock reflections overtaking the shock front in the shock regime. Additionally, the slower shock wave speed was explained by the shock front dying out earlier than expected.

Tsai & Prakash also provided an analytical solution for shock loading of periodically layered composites, taking into account both elastic-elastic systems as well as elastic-viscoelastic systems.[15] They performed plate impact experiments on iron-titanium and aluminum-polycarbonate composites to verify their solution. They found that the elastic precursor decayed for increasing interface impedance-mismatch, increasing interface density, and increasing material inelasticity. The speed of the precursor was found to be equal to the average wave speed of the composites. The speed of the late-time oscillatory wave was found to decrease with increasing impedance mismatch, but was independent on the interface density. The rise time in the late-time wave increased with increasing impedance mismatch but decreased with increasing interface density. The late-time oscillations were found to oscillate around a mean value, and that increasing the interface impedance mismatch resulting in a decrease in oscillation frequency, while increasing the interface density increased the oscillation frequency.

Incorporating ferroelectric material into an impedance-mismatched layered composite could allow for electrical control of the shock wave structure by altering the interface impedance mismatch through some combination of the piezoelectric effect, hindering domain switching, or hindering the FE-AFE phase transformation. In order to investigate this possibility, layered composites of PZT 95/5 and brass were fabricated and shocked using a 100 mm single stage gas gun. PZT 95/5 was chosen since it was assumed to be less strain-rate sensitive than PZT 5A, allowing for the effects of variations in impact velocity to be reduced. In addition, the change in mechanical response of the FE and AFE phases in PZT 95/5 is assumed to be more significant than that of the domain switching behavior of PZT 5A. Brass was chosen due to its similar impedance to PZT, in the hopes that any change in impedance mismatch due to the electrical boundary conditions would be more discernable in the experimental results. Kapton tape was used to electrically isolate the front and rear sections of the ferroelectric. The electrical boundary conditions across the ferroelectric layers were controlled using difference series resistances for each experiment. The electrical boundary conditions had previously been shown to effect shock wave structure[7-9] and the FE-AFE phase transformation[8] of PZT 95/5 at shock stresses of 1.3 GPa and 0.9 GPa, respectively. Therefore, these two stresses were chosen to explore a set of four electrical boundary conditions, resulting in a total of eight impact experiments.

4.2 Procedure: Flyer Plate Impact Experiments

Two sets of impact experiments were performed using the 100 mm single stage gas gun at the High Pressure Particulate Physics Facility at Eglin Air Force Base, Florida. The higher-pressure experiments were performed using brass impactors launched with an impact velocity of 90±6 m/s, while the lower-pressure experiments were performed using PMMA impactors launched at an impact velocity of 270±13 m/s. The ferroelectric composite consisted of two

ferroelectric layers, each between two brass layers which acted as electrodes. This allowed each ferroelectric layer to have their electrical boundary conditions set independently from one another. The polarization direction in the front ferroelectric layers was chosen to be parallel to the shock propagation direction, while the rear was chosen to be antiparallel. This was done to keep the inner brass layers at a grounded potential to prevent crosstalk between the ferroelectric layers. A thin layer of high dielectric strength Kapton tape was placed between the two to insure electrical isolation. A schematic for the composites can be seen in figure 4.1. Each brass layer was double-sided lapped to ensure planarity down to 10 μms. The layers are nominally 1.5 mm thick, with slight variation between the lower-pressure and higher-pressure experiment sets due to the double-sided lapping process.

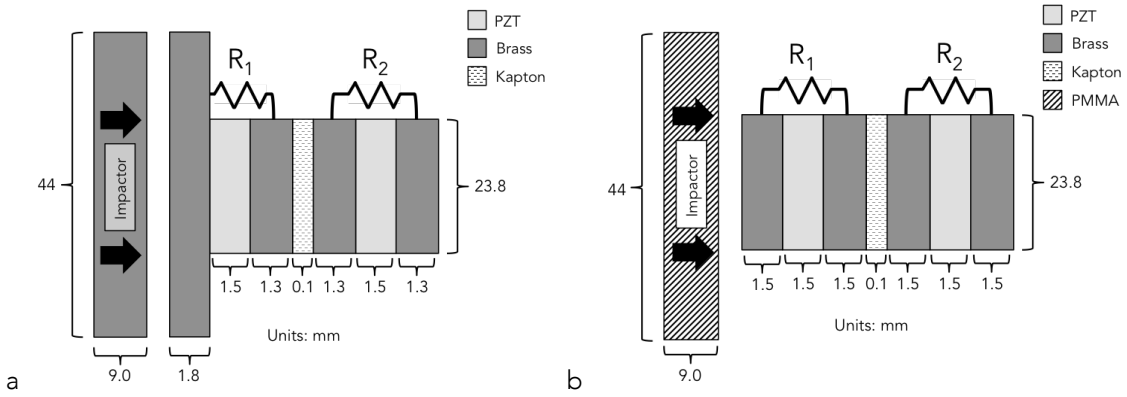

Figure 4.1: Multilayer design for impact experiments. The higher-pressure experiments (a) utilized a brass impactor, while the lower-pressure experiments (b) utilized a PMMA impactor. The stack consisted of two PZT ferroelectric layers sandwiched between brass layers that acted as the electrodes for the PZT layers. The two brass/PZT/brass components were electrically isolated from one another using Kapton tape. Series resistances R_1 and R_2 were used to control the electrical boundary conditions within the ferroelectric layers.

The layers were bonded together under pressure from a hand vice using a two-part low viscosity epoxy. Coaxial leads were soldered to each brass layer prior to bonding, where the inner conductor was used to record the ferroelectric depoling current pulse, while the outer conductor was terminated around 10 mm from the composite and only acted as a grounded shield to

prevent crosstalk between the circuits (fig 4.2a). The composite was then centered in a target plate and potted using a two-part epoxy (fig. 4.2b). Both the composite and target plate were potted while clamped against a planar surface to ensure planarity between composite and target plate faces.

a  b 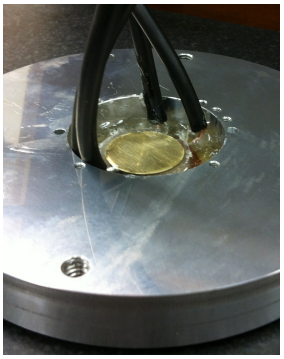

Figure 4.2: Picture of the fabricated multilayer composite with shielded coaxial electrical leads attached (a). The composite was set in an aluminum target plate and potted with epoxy for mechanical support and electrical isolation (b).

Once the composite was potted into the target plate, tilt sensors and velocity interferometer probes were added. The coaxial cables acting as electrical leads were connected in series to a 0.01 Ω thin film surface mount resistor for recording the current. A coaxial cable was connected across this current viewing resistor and ran to a gigahertz oscilloscope terminated with a 50 Ω terminator. The current viewing resistor was rated as extremely low inductance (0.5 – 5 nH) with excellent frequency response (50 MHz).[16] In order to alter the electrical response of the ferroelectric layers, a load resistance was placed in series with the ferroelectric and current viewing resistor. High pulse load MELF resistors ranging from 2.2 – 10 Ω were used to construct load resistances from 2 – 14.5 Ω. The load resistors were rated up to 10kV / 17 kW for single pulses.[17] The resistance values were chosen in order to generate significant electric field in an attempt to alter the shock profile and hinder the FE-AFE phase transformation without undergoing dielectric breakdown across the ferroelectric.[18] The resistors were potted in a two

part epoxy, wrapped with electrical tape, then wrapped in conductive foil. The foil and outer conductor of the coaxial cable used for leads from the brass layers to the current viewing resistor were then grounded to reduce any electromagnetic interference produced by the sudden depoling of the ferroelectric layers. Each ferroelectric layer was then electrically isolated from one another.

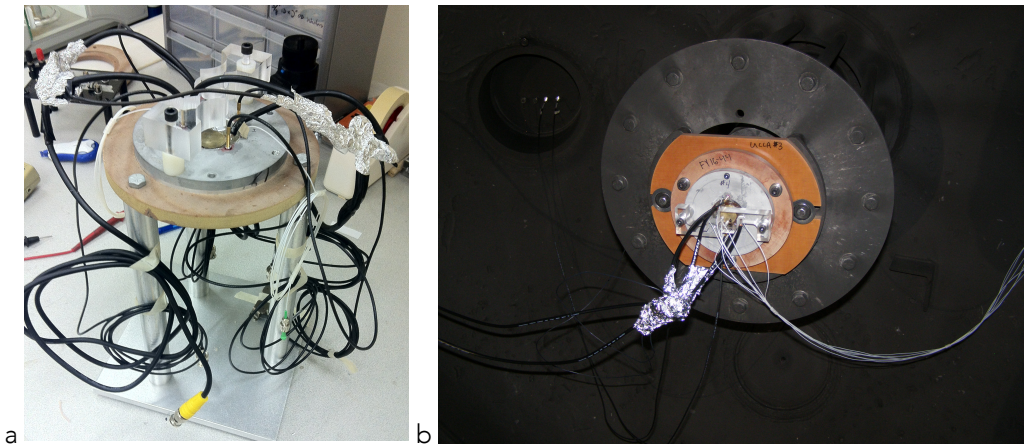

Figure 4.3: Final target plate assembly for the higher-pressure experiments (a) utilizing VISAR and lower-pressure experiments (b) utilizing PDV. Shorting pins were used to identify tilt in the higher-pressure experiments, while PDV probes were used to identify the flyer velocity. The shorting pins and VISAR probes were switched to PDV probes to identify tilt and free surface particle velocity in the lower-pressure experiments.

The higher-pressure experiments utilized shorting pins for the tilt sensors, photon Doppler Velocimetry (PDV) probes for the impact velocity measurements, and a single velocity interferometer system for any reflector (VISAR) probe for the free surface particle velocity measurements. Figure 4.3a shows the final target plate set up. For the lower-pressure experiments, the tilt pins were replaced with PDV probes to reduce crosstalk between the piezo shorting pins and the ferroelectric circuits. The single VISAR probe was replaced with multiple PDV probes to record the free surface particle velocity at the not only the center of the rear surface, but also the sides (5 mm up and 5 mm down from center) of the composite. Figure 4.3b

shows the final target plate set up, installed within the catch tank at the end of the 100 mm gas gun.

A 100 mm single stage gas gun (fig. 4.4a) was used for the impact experiments. Brass and PMMA impactors were machined and bonded into aluminum projectiles using low viscosity epoxy under pressure from a hand vice (fig. 4.4b). The impactors were nominally 44 mm in diameter and 9 mm thick, as depicted in figure 1a & b. The projectiles weighed approximately two kilograms in total. For the higher-pressure experiments, brass was chosen as the impactor material to ensure symmetric impact and to reduce the number of impedance-mismatched interfaces to those within the composite. The gas gun system had a limiting lower projectile range of around 70 m/s, requiring that the lower-pressure experiments utilize a lower impedance impactor material (PMMA) at higher velocities. This resulted in an additional impedance-mismatched interface at the interface of the impactor and first brass layer of the composite.

a  b 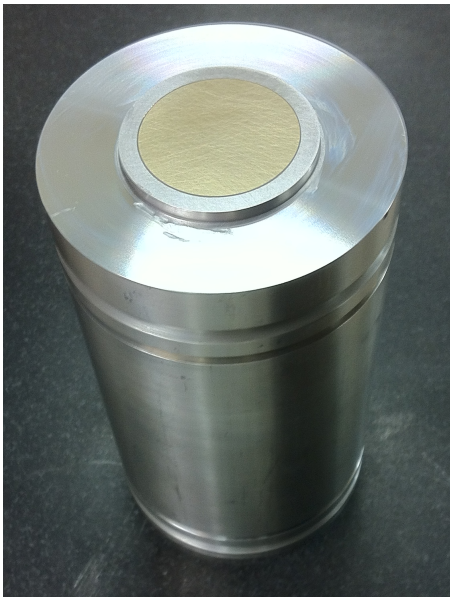

Figure 4.4: A 100 mm bore single stage gas gun (a) was used to launch aluminum projectiles (b) with either brass (higher-pressure experiments) or PMMA (lower-pressure experiments) impactors.

Impedance matching techniques utilizing the Hugoniots for brass,[19] PMMA,[19] and PZT[20] were used to identify the required impact velocity for the higher (fig. 4.5a) and lower (fig. 4.5b) pressure experiments. An impact velocity of 90 m/s utilizing a brass impactor resulted in approximately 1.4 GPa of pressure in the ferroelectric layers, while an impact velocity of 270 m/s utilizing a PMMA impactor resulted in approximately 0.90 GPa of pressure in the ferroelectric layers. These pressures were chosen since they would ensure that the FE-AFE phase transformation would be driven to near-completion while remaining low enough that the electrical boundary conditions may still have an effect on wave profile, most likely by hindering the transformation.

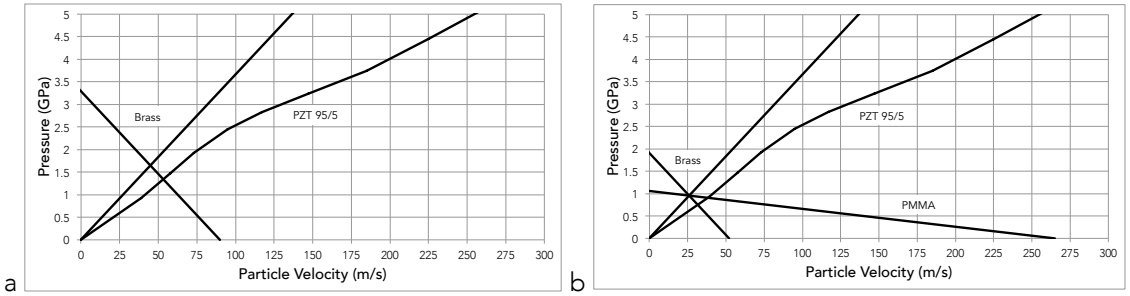

Figure 4.5: Impedance matching of brass (a) and PMMA (b) flyers on brass/PZT multilayer composites using Hugoniots of brass, PMMA, and PZT 95/5. The brass flyer velocity of 90 m/s results in a pressure of 1.4 GPa within the PZT layers, while the PMMA flyer velocity of 270 m/s results in a pressure of 0.90 GPa within the PZT layers.

4.3 Procedure: ALEGRA-FE FE-AFE Module Simulation

In order to elucidate some of the experimental behavior, the electromechanical response of the multilayered composite was computed using the multiphysics shock hydrocode ALEGRA-FE. The operating principles of the mechanical aspects of the ALEGRA hydrocode can be found in Ref. 21. The addition of the FE-AFE material module implemented in ALEGRA allows for the complex electromechanical interactions to be considered by updating the quasistatic electrical state during each time step. The ferroelectric material model for PZT 95/5 implemented in the

FE-AFE module takes into consideration the mechanical and dielectric behavior of both the FE and AFE phases. The transformation pressure, dielectric breakdown field, phase transformation rate, and remnant polarization can all be independently assigned. The simulation's default material parameters were used. Unfortunately, there is no mechanism in the model's formulation to alter the mechanical behavior of the material based on the internal electric fields. Still, the stress state, particle velocity history, and mechanical depolarization can all be modeled assuming a SC configuration.

The three dimensional simulation was modeled using the geometry of figure 4.1a & b. Electrical boundary conditions were set at the front and rear surfaces of the front and rear ferroelectric layers in order to allow for SC behavior. Material tracers were placed in the geometric center of the front and rear ferroelectric layers to capture the stress state and mechanical polarization. An additional tracer was placed on the back surface of the composite to capture the free surface particle velocity history. The radial and tangential mechanical boundary conditions were set to zero displacement in order to keep the system under a state of uniaxial strain. In addition, the effect of layer debonding was modeled by adding a small (0.1 μm thick, 2 mm radius) air gap at the location of the Kapton tape. A second tracer was placed 5 mm above the center tracer in compare velocity histories.

4.4 Results: Flyer Plate Impact Experiments

Both the higher and lower-pressure experiments yielded impact velocity and impactor tilt data, depoling current history, and free surface velocity histories. Figure 4.6 shows the free surface particle velocity histories for the higher-pressure experiments recorded with VISAR (fig. 4.6a) and the lower-pressure experiments recorded with PDV (fig. 4.6b). Here only the center PDV probes are shown for the lower-pressure experiments. Both groups of experiments show a

pronounced step in the velocity profile around 30-35 m/s, and have significant oscillations in the late-time profiles. The step has been attributed to the FE-AFE phase transformation.[5] The precursor rise time varies significantly with both sets of experiments and does not appear to be a function of impact velocity or electrical boundary conditions. Most noticeable is the extreme spread in arrival time, suggesting a large variation in effective composite wave speed.

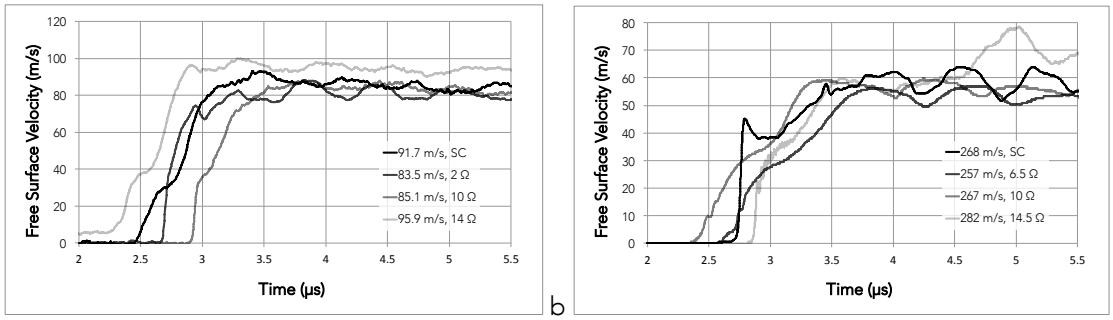

Figure 4.6: VISAR free surface particle velocity histories for the higher-pressure experiments (a) with average impact velocities of 89.7 ± 6.2 m/s. PDV free surface particle velocity histories for the lower-pressure experiments (b) with average impact velocities of 270 ± 13 m/s.

4.4.1 Higher-Pressure (~1.4 GPa) Experiments: Particle Velocity Histories

Figure 4.7 shows the four higher-pressure experiments free surface particle velocity histories. The SC experiment had no load resistance and only a current viewing resistor in series with each ferroelectric layer (fig. 4.7a). The 2 Ω experiment has noticeably enhanced late-time oscillations compared to the other higher-pressure experiments (fig. 4.7b). The 10 Ω experiment has a similar profile to the SC profile with the exception of a steeper precursor rise time (fig. 4.7c). The 14 Ω experiment has also has a profile similar to the SC experiment, with the exception of a small ~5 m/s initial velocity (fig. 4.7d). Due to issues with electrical crosstalk between the shorting pins and the front ferroelectric layers, this experiment attempted to utilize shorting pins that were significantly offset from the target face (~ 1 mm). This unfortunately resulted in a small velocity wave arriving a couple of microseconds before the shock front.

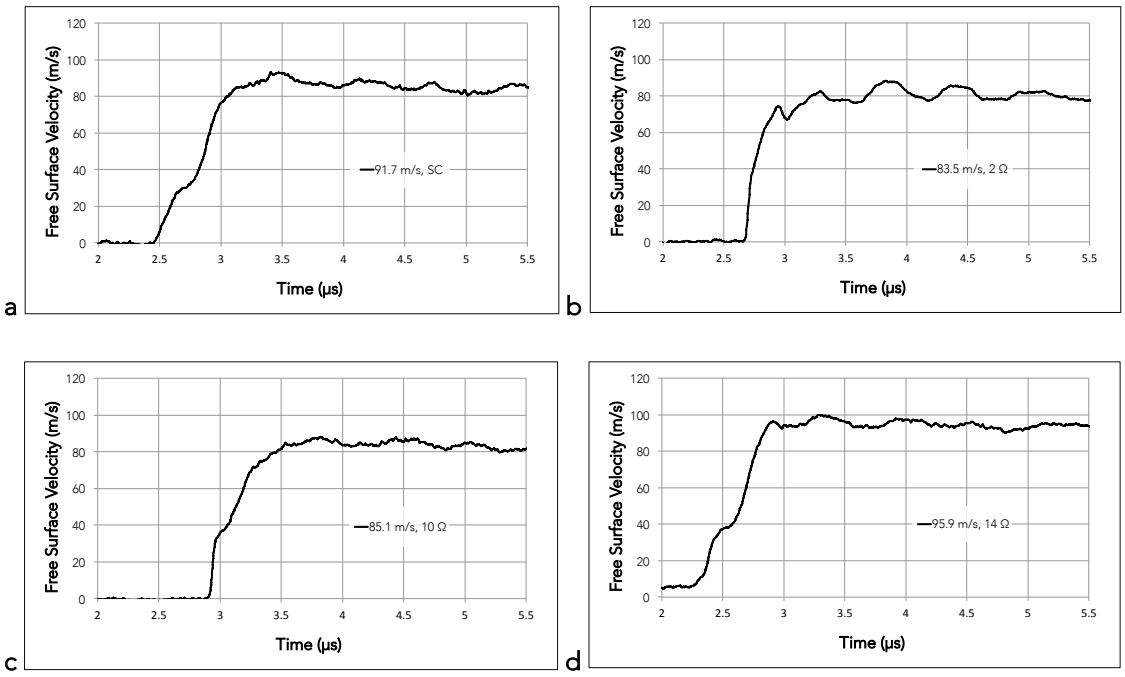

Figure 4.7: Individual VISAR free surface particle velocity histories for the SC experiment at impact velocity of 91.7 m/s (a), 2 Ω series resistance at 83.5 m/s (b), 10 Ω series resistance at 85.1 m/s (c), and 14 Ω series resistance at 95.9 m/s (d) for the higher-pressure (1.4 GPa) experiments.

4.4.2 Higher-Pressure (~1.4 GPa) Experiments: Depoling Currents

Figure 4.8 shows the depoling currents (dashed line) and corresponding released charge density (solid line) for the front (grey) and rear (black) ferroelectric layers as a function of time. The charge density was computed by integrating the current and dividing by the area of the electrodes. The mechanical depoling of the ferroelectric layers is driven by both domain switching and the FE-AFE phase transformation, with the later dominating once the pressure within the ferroelectric layers reaches the transformation pressure. For full ferroelectric depolarization, the released charge density value should equal the remnant polarization value, which could range from 0.33 to 0.40 C/m^2 for PZT 95/5.[22,23] The released charge density in the SC experiment initially overshoots to a value of 0.43 C/m^2, but quickly decreases to the remnant

polarization value of 0.33±0.01 C/m^2 for both the front and rear ferroelectric layers (fig 4.8a). The 2 Ω series resistance experiment was actually the first experiment performed, and a combination of improper electrical impedance termination at the oscilloscope, along with shorting between the ferroelectric layers, caused the depoling current pulse to reflect within the circuit (fig. 4.8b). The period of oscillation of the electrical ringing corresponded to twice the approximate length of the coaxial cable the signal traverses from current viewing resistor to oscilloscope. The 10 Ω series resistance experiment's rear layer's released charge density exhibited a similar overshoot as in the SC experiment. The charge density overshoots to a value of 0.51 C/m^2 and relaxes to a value of 0.33 C/m^2 (fig. 4.8c). The front layer's released charge density obtains an unphysical value due to the shorting tilt pin's capacitors partially discharging through the front ferroelectric's circuit. While the front brass layer was kept electrically isolated from the target face, the brass and aluminum impactor provided a conductive path for the charge released by the shorting pins. Therefore, for the 14 Ω series resistance experiment, the tilt pins were extended to ~1 mm proud from the target surface. This resulted in a small, initial velocity wave prior to the shock front as seen in figure 4.7d, but succeeded in isolating the front ferroelectric circuit from crosstalk. The 14 Ω series resistance experiment's front ferroelectric layer's released charge density overshoots to a value of 0.43 C/m^2 and relaxes to the remnant polarization value of 0.31 C/m^2 (fig. 4.8d). The rear ferroelectric layer's released charge density does not overshoot, but instead obtains a final value of 0.29 C/m^2, which indicates partial depoling and thus an incomplete FE-AFE phase transformation. Given that this experiment had the highest impact velocity and thus loading stress, it is more likely that the high series resistance and resulting internal electric field of 4.1 kV/mm was responsible for the incomplete phase transformation.

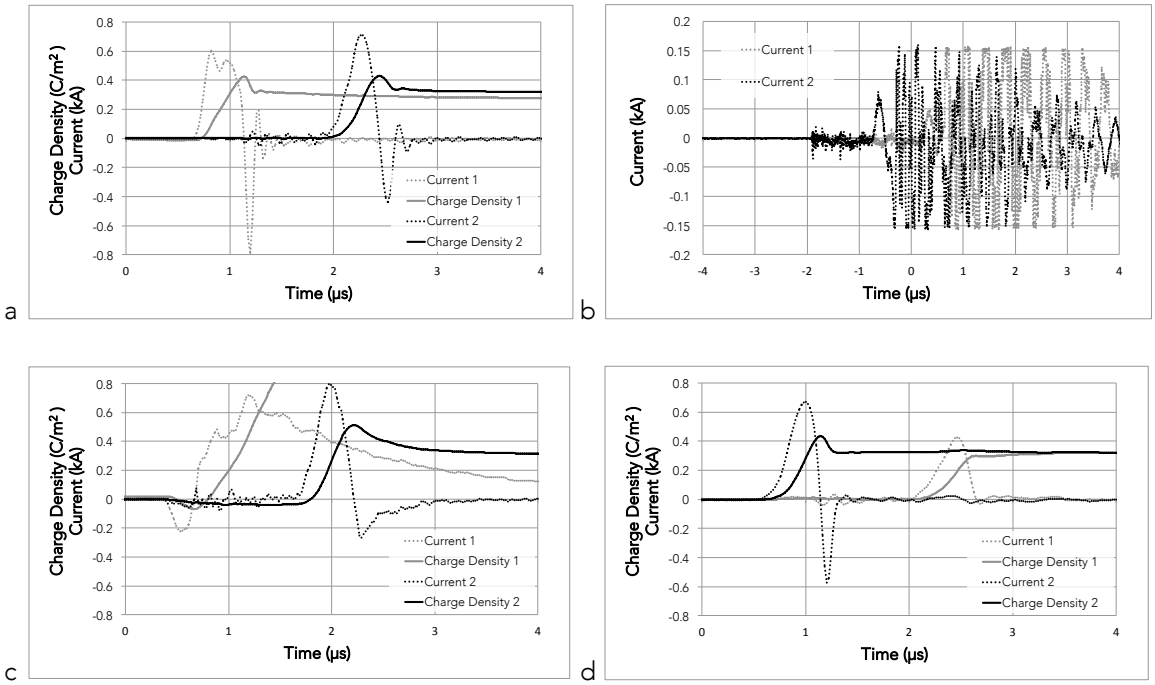

Figure 4.8: Ferroelectric depoling currents and released charge density plots for SC (a), 2 Ω series resistance (b), 10 Ω series resistance (c), and 14 Ω series resistance (d) for higher-pressure (1.4 GPa) experiments. The front (grey) and rear (black) ferroelectric layers are denoted with labels '1' and '2', respectively. The 2 Ω series resistance experiment suffered from mismatched electrical impedance at the oscilloscope and possible crosstalk between ferroelectric circuits, confusing the data. The 10 Ω series resistance experiment suffered from crosstalk from the tilt pins and front ferroelectric layer, causing excess charge across the current viewing resistor. Most plots exhibit an overshoot of the released charge density to high values that relax back to the remnant polarization values of around 0.33 C/m^2.

4.4.3 Lower-Pressure (~0.9 GPa) Experiments: Particle Velocity Histories

The free surface particle velocity histories presented in figure 4.6b was that of the center PDV probes. Figure 4.9 presents this data in addition to the free surface particle velocity histories from the off-center PDV probes, which have been placed 5 mm above (up) or below (down) the center probes. This was done to understand how the wave travels within the composite. Each wave arrival time has been adjusted to take into account any impactor tilt, which was less than 2 mrad for each experiment. Figure 4.9a shows the velocity histories for the SC experiment, with an

impact velocity of 268 m/s. The wave arrives at the upper back surface of the composite 200 ns before it arrives at the center. The center has an extremely short shock front rise time, and significant oscillations in the late-time wave profile. Figure 4.9b shows the velocity histories for the 6.5 Ω series resistance experiment, with an impact velocity of 257 m/s. The wave arrives at the upper back surface of the composite 450 ns before it arrives at the center, while it arrives at the lower back surface of the composite 100 ns before it arrives at the center. The rise time is much greater for both the center and side profiles compared to the SC experiment. The oscillations in the late-time profile appear to damp out more quickly as well. Figure 4.9c shows the velocity histories for the 10 Ω series resistance experiment, with an impact velocity of 267 m/s. Here the PDV data is slightly ambiguous at the toe of the wave due to fringe effects; the oscillations are an artifact of the PDV system. The wave arrives at the lower back surface of the composite approximately 200 ns before it arrives at the center, while it arrives at the upper back surface of the composite approximately at the same time as it arrives at the center. The general shape of the profile looks similar to the 6.5 Ω series resistance experiment. Figure 4.9d shows the velocity histories for the 14.5 Ω series resistance experiment, with an impact velocity of 282 m/s. The wave arrives at the upper back surface of the composite 380 ns before it arrives at the center. The center wave front rise time is considerably smaller than that of the 6.5 and 10 Ω resistance experiments, similar instead to the SC experiment.

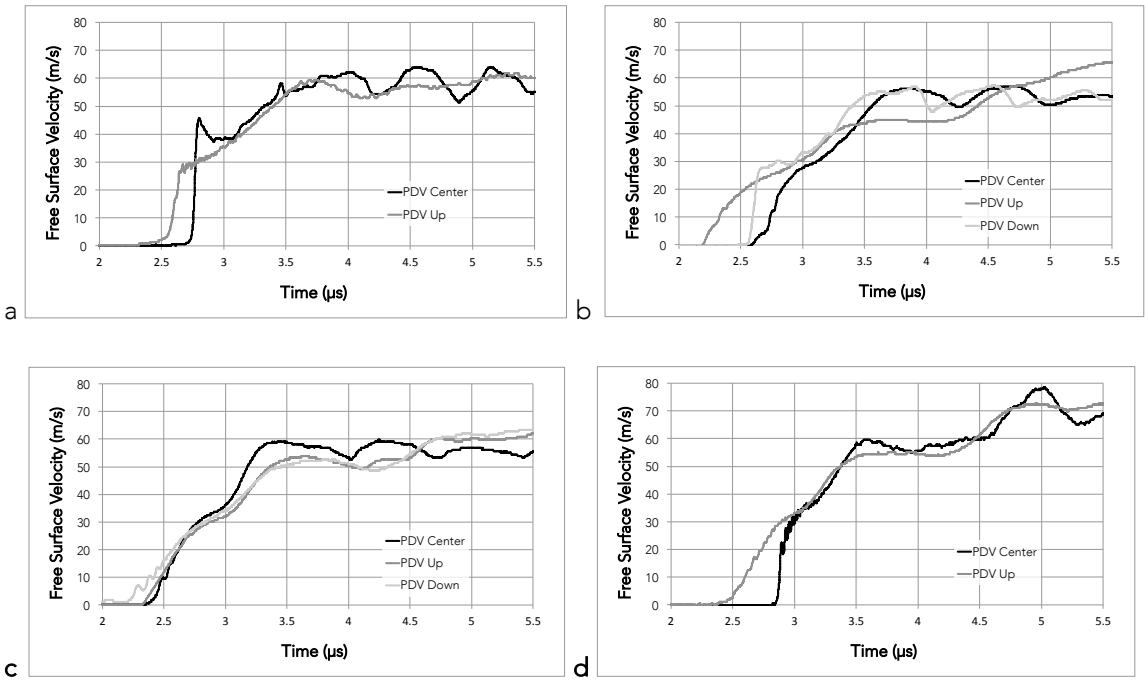

Figure 4.9: Free surface velocity histories obtained via Photon Doppler Velocimetry under SC (a), 6.5 Ω series resistance (b), 10 Ω series resistance (c), and 14.5 Ω series resistance (d) for lower-pressure (~0.90 GPa) experiments. For all the experiments, the wave travels slower down the center of the composite.

4.4.4 Lower-Pressure (~0.9 GPa) Experiments: Depoling Currents

Figure 4.10 shows the depoling currents (dashed line) and corresponding released charge density (solid line) for the front (grey) and rear (black) ferroelectric layers as a function of time. The released charge density in the front ferroelectric layer of the SC experiment initially overshoots to a value of 0.33 C/m^2, but quickly relaxes down to the remnant polarization value of 0.29 C/m^2 (fig 10a). The rear ferroelectric layer experiences no overshoot but approaches a released charge density value of 0.30 C/m^2. Both of the final charge density values are below the expected remnant polarization values. The released charge density in the front ferroelectric layer of the 6.5 Ω series resistance experiment approaches a value of value of 0.32 C/m^2, while the rear layer approaches a value of value of 0.31 C/m^2 (fig 4.10b). These are again below the expected remnant polarization value. The released charge density in the front ferroelectric layer of the 10 Ω

series resistance experiment only reaches a value of value of 0.06 C/m^2 due to electrical shorting, while the rear layer approaches a value of value of 0.29 C/m^2 (fig 4.10c). The released charge density in the front ferroelectric layer of the 14.5 Ω series resistance experiment only reaches a value of value of 0.07 C/m^2 due to electrical shorting, while the rear layer approaches a value of value of 0.32 C/m^2 (fig 4.10d). The electrical breakdown in figures 10c & d occurred at an electric field value of 2.3 and 2.8 kV/mm, respectively, well under the reported dielectric breakdown strength of PZT 95/5 under shock compression.[18] This suggests that electrical shorting occurred along the edges of the ferroelectric layers, where air gaps between the ferroelectric and potting material may be present. The dielectric strength of air is around 3 kV/mm,[24] which is around the internal electric field values.

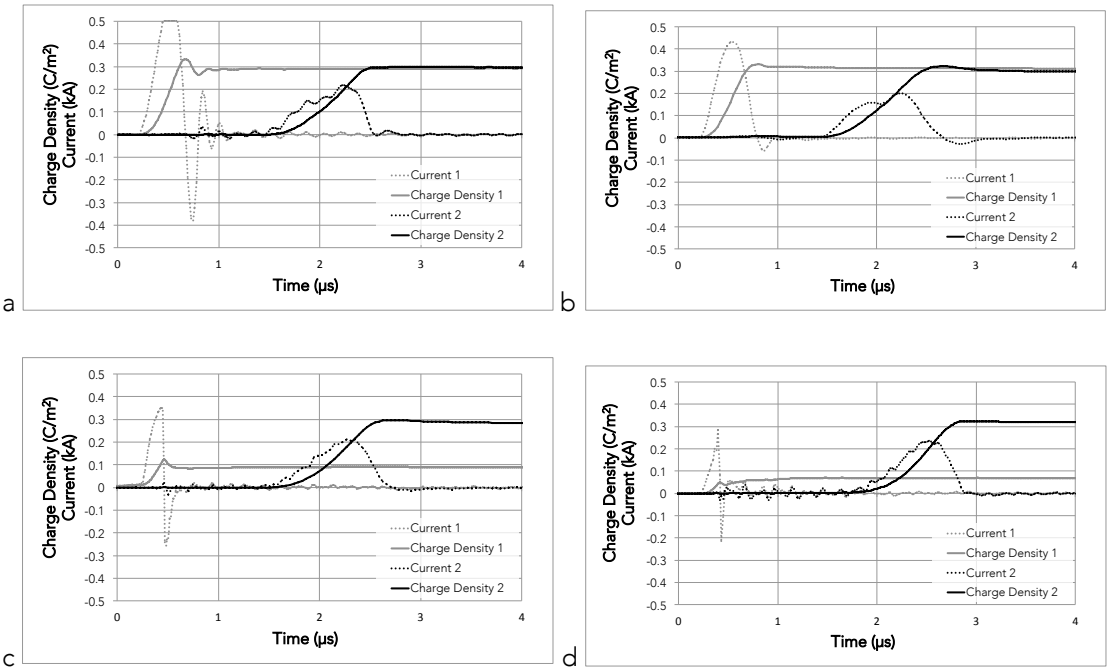

Figure 4.10: Ferroelectric depoling currents and released charge density plots for SC (a), 6.5 Ω series resistance (b), 10 Ω series resistance (c), and 14.5 Ω series resistance (d) for lower-pressure (0.90 GPa) experiments. The front (grey) and rear (black) ferroelectric layers are denoted with labels '1' and '2', respectively. The front layers subjected to higher electric field (c & d) suffered from electrical breakdown, indicated by partial depolarization.

4.5 Discussion: Flyer Plate Impact Experiments

4.5.1 Particle Velocity Histories

One of the most striking results of the experiments was the wide range of effective wave speed within the composite. Figure 4.11 shows the effective composite wave speed (a) and rise time (b) for each of the four higher-pressure experiments calculated from figure 4.7a-d. In general, both the composite wave speed and rise time of the shock front is expected to increase with increasing impact velocity. The Hugoniot plots of brass and PZT 95/5 place the predicted shock wave speed at 3.9 km/s. The composite wave speed is expected to be lower than this value due to the wave front slowing when propagating through multiple impedance-mismatched interfaces.[14] The calculated composite wave speed (fig. 4.11a) for all experiments is below this value, in agreement with Zhuang et al.[12] There is a slight general trend of increasing composite wave speed with increasing impact velocity, while the rise times (fig. 4.11b) increase with increasing impact velocity.

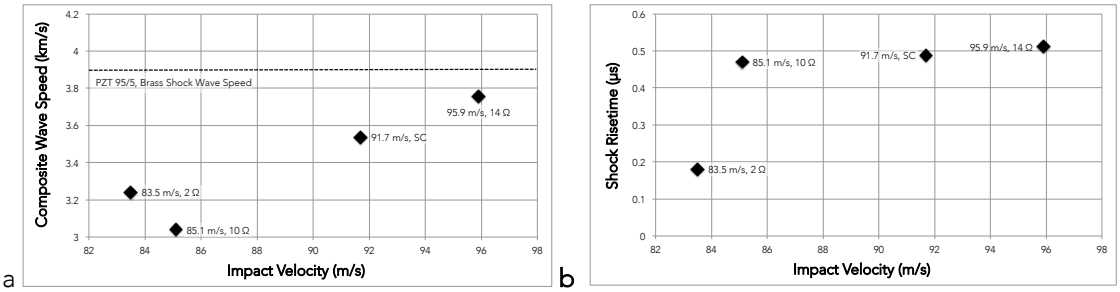

a b

Figure 4.11: Composite wave speeds (a) and shock rise time (b) for the higher-pressure experiments. The composite wave speeds are primarily below the predicted shock velocity (3.9 km/s) of the individual components of brass and PZT. The rise time generally increases with increasing load.

Figure 4.12 shows the effective composite wave speed (a) and rise time (b) for each of the four lower-pressure experiments calculated from figure 4.9a-d. The Hugoniot plots of brass and

PZT 95/5 place the predicted shock wave speed at 3.8 km/s. The calculated composite wave speed (fig. 4.12a) for most experiments is below this value. There is a slight general trend of decreasing composite wave speed with increasing impact velocity, while the rise times (fig. 4.12b) decrease with increasing impact velocity. These trends oppose those of the higher-pressure experiments and that predicted by the Hugoniot curves.

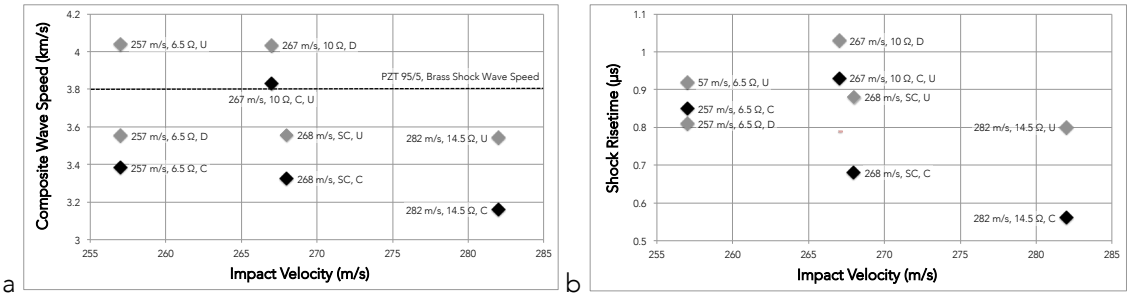

Figure 4.12: Composite wave speeds (a) and shock rise time (b) for the lower-pressure experiments. Most of the composite wave speeds are below the predicted shock velocity of the individual components of brass and PZT. The rise time generally decreases with increasing load.

One of the premises of this research was to investigate whether the wave scattering within the multilayered composite could be influenced by the electrical boundary conditions of the PZT layers. Towards this end, the late-time velocity profiles of the higher-pressure (fig. 4.7a-d) and lower-pressure (fig. 4.9a-d) experiments were converted into the frequency domain using fast-Fourier transforms (FFT). Figure 13a & b shows the FFTs of the higher-pressure and lower-pressure experiments. If the individual layer thicknesses within the multilayered composite are taken to be ~1.5 mm, and the wave speed in the brass and PZT materials approximated as ~4.2 mm/µs, then the characteristic frequency from the interface reflections should be approximately 1.4 MHz. Figures 4.13a & b show strong peaks around 1.5 MHz for all of the experiments, however there is no evidence for a dependence on the electrical boundary conditions.

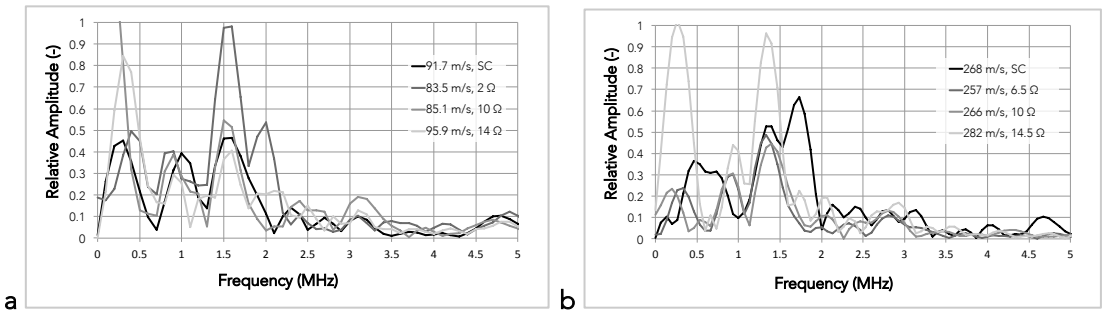

Figure 4.13: Fast-Fourier transform of the late-time particle velocity for higher-pressure (a) and lower-pressure (b) experiments. The periodic oscillations around 1.5 MHz show no dependence on the electrical boundary conditions, but instead on impact velocities.

Instead, the relative scattering amplitude appears to be dependent on impact velocity. Figures 4.14a & b show the amplitude of the 1.5 MHz peaks as a function of impact velocity for the higher (fig. 4.14a) and lower (fig. 4.14b) pressure experiments. There is a decreasing trend of relative scattering amplitude with increased impact velocity for the higher-pressure experiments, while the lower-pressure experiments show an increasing trend.

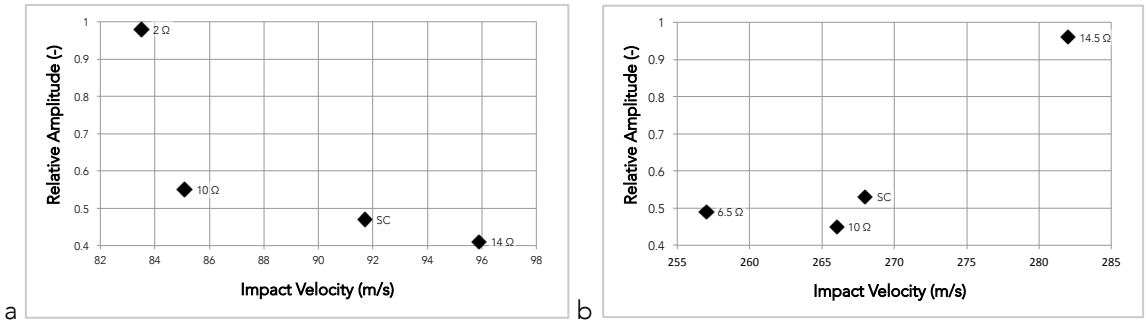

Figure 4.14: Relative scattering amplitude of the ~1.5 MHz oscillations of the late-time particle velocity as a function of impact velocity for higher-pressure (a) and lower-pressure (b) experiments. There is a decreasing trend for the higher-pressure experiments and increasing trend with the lower-pressure experiments. The increasing of the late-time oscillation with increasing loading strength (impact velocity) for the lower-pressure experiments agrees with the findings of Ref. 11.

The opposing trends of the higher and lower-pressure experiments are curious. It may be that the data for both sets fall in the range of experimental random noise. It is unlikely that the

difference in pressure regimes contributes to the differing trends, as there are no significant features in the Hugoniots for any of the constituents between 0.9 and 1.4 GPa. Both the higher and lower-pressure experiments were above the Hugoniot elastic limit of the brass while well below the yielding stress. The experiments were likewise above the start of the FE-AFE phase transformation of the ferroelectric while well below the pressure of pore collapse. From previous research with polycarbonate/metal periodically layered composites,[12] one would expect the rise time to decrease with increasing impact velocity, in agreement with the trend seen in figure 4.12b for the lower-pressure experiments. The difference in impactors for the two sets of experiments (brass for the higher-pressure experiments, PMMA for the lower-pressure experiments) may contribute to the trends by the way in which they reflect wave trains from the impedance-mismatched interfaces of the composite. The brass impactor would be perfectly impedance matched to the first brass layer, and as such that impact interface would be invisible to back-reflected waves. The PMMA impactor would create a highly impedance-mismatched interface resulting in the increase of the number of internally reflected compression and rarefaction waves. These waves are what have been attributed with the reduction of wave velocity through interaction with the shock front.[12] Therefore the effect of impact velocity may be more apparent in the experiments that utilize a PMMA impactor, i.e. the lower-pressure experiments.

4.5.2 Depoling Currents

The depoling data in figures 4.8 and 4.10 show that the ferroelectric layers nearly full depolarization due to shock compression. The released charge density in the higher-pressure experiments (fig. 4.8) show an overshoot effect that may be due to stray inductance. The value of the charge density quickly returns to a reasonable value and then slightly decays. If we take the final depolarization value to be that right after the overshoot, the released charge density all rise

above 0.29 C/m^2. The released charge density for the lower-pressure experiments likewise rise above 0.29 C/m^2, with the exception of the two front layers under higher load resistances. These two suffer from electric breakdown and release only ~20% of their bound charge through the current viewing resistor. Figure 4.15 shows the released charge density as a function of peak electric field within the ferroelectric layers for all experiments. There is no trend relating the total released charge density to peak electric field, impact velocity, or load resistance. Assuming a remnant polarization value of 0.35 C/m^2, the majority of the layers were depoled by at least 80%.

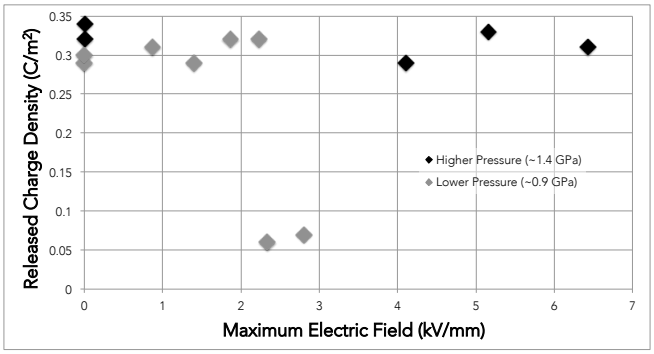

Figure 4.15: Released charge density as a function of maximum electric field within each of the ferroelectric layers. The results indicate that the majority of the layers were depoled by at least 80%.

It is difficult to infer the behavior regarding the phase transformation with stray inductance effects complicating the data with artificially high charge density values. However, for the lower-pressure experiments, most of the data did not show any overshoot effects, with the exception of the front layer of the SC experiment. Figure 4.10 a-d show the depoling characteristics for the lower-pressure experiments. The front ferroelectric layers in the higher filed experiments (fig. 4.10 c & d) suffered from electrical breakdown. Figures 4.10 a & b show a markedly different shape of the current released by the ferroelectric layers for the front and rear layers. Two factors can contribute to such differences. The first and most obvious is the evolving shock structure, where the wave front is more dispersed in the rear layer due to the wave

scattering from the previous layers interfaces. The second is due to the polarization orientation of the ferroelectric layers. In our experimental configuration, the front layers' polarization are oriented parallel to the shock propagation direction, and the rear layers' are oriented antiparallel. Mock and Holt shock depoled PZT 56/44 in both the parallel and antiparallel orientation and discovered that the antiparallel orientation required more time to reach the peak current and also suffered from electrical breakdown.[26] Cutchen discovered that in the antiparallel orientation, electrical breakdown becomes more likely[22,27] Figure 4.10 a & c illustrate the depoling in the front and rear layers, where the rear layers depole more slowly, in agreement with the results of Mock and Holt.

The depoling kinetics can help elucidate the phase transformation kinetics. The Kolmogorov-Johnson-Mehl-Avrami (KJMA) theory has been used to describe the time evolution of the order parameter in a variety of systems, including first order phase transformations[28-30] and ferroelectric domain switching.[31-35] The assumptions made by KJMA theory, which include a constant nucleation rate and interfacial wave speed, are satisfied due to the constant velocity of the shock wave and relatively fast rise in pressure across the front. Here, the order parameter is the polarization, whose value can be computed through the released charge density in figures 4.8 and 4.10. The polarization ranges from the remnant polarization value of 0.33 - 0.40 C/m^2 down to zero for material that has been fully depoled. Since the released change density is directly related to the change of polarization, it can be modeled using the KJMA equation, often simply called the Avrami equation (Eq. 4.2).

$$P = P_0(1 - \exp(-k \cdot t^n)) \tag{4.2}$$

The Avrami equation states that the released charge density from the depolarization of the ferroelectric, P, is dependent on the remnant polarization, P_0, and two fitting parameters, k and n. Traditionally, the fitting parameter k has been a thermally activated rate constant which

represents both growth and nucleation rates, while the exponent n represents the transformation process and ranges from 1 – 4. The exponential fitting parameter n has been associated with the number of growth dimensions as well as the nucleation rate, ranging from n=2 for two-dimensional growth, to n=3 for three dimensional growth with zero nucleation rate, to n=4 for three dimensional growth with constant nucleation rate.[34] Unfortunately, the depoling data for the higher-pressure experiments suffered from an artificial overshoot of the released charge density, which should have maximized at the remnant polarization value. Therefore, we restrict our analysis of the released charge density to the lower-pressure experiments. We further restrict our analysis to those ferroelectric layers that did not suffer electrical breakdown. This leaves the two front ferroelectric layers in the SC and ~6.5 Ω series resistance experiments, and all of the rear ferroelectric layers. Fitting was accomplished using the MATLAB curve fitting toolbox while requiring that the maximum remnant polarization be restricted to less than the maximum manufacture's published value of 0.405 C/m[22].[23] All fitted plots have R-squared values better than 0.998.

Figure 4.16 shows the Avrami fit for the depolarization of the front and rear ferroelectric layers under SC configuration for the lower-pressure experiment. Figure 4.17 shows the Avrami fit for the depolarization of the front and rear ferroelectric layers for the lower-pressure experiment under ~6.5 Ω series resistance. Figures 4.18 a & b show the Avrami fit for the depolarization of the rear ferroelectric layers for the lower-pressure experiments under ~10 Ω and ~14.5 Ω series resistances, respectively. All of the fitted remnant polarization values are between 0.33-0.40 C/m^2, without being constrained. The depolarization time for the front layers (~0.5 μs) is substantially less than that of the rear layers (~1.2 μs).

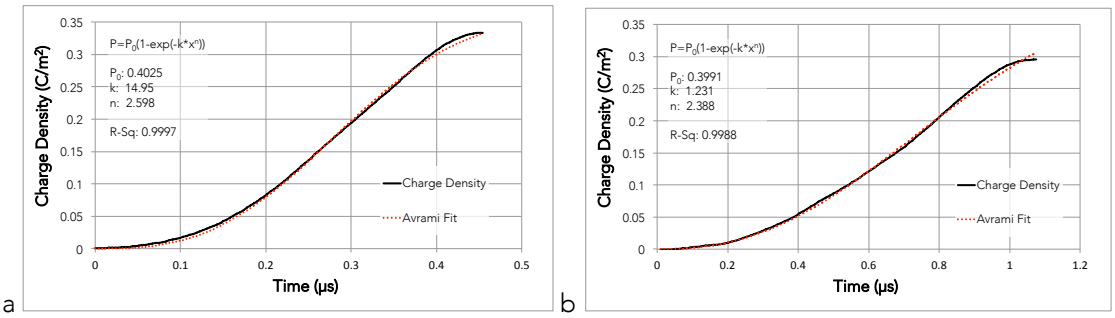

Figure 4.16: Ferroelectric depoling charge density plots with Avrami fit for the front (a) and rear (b) layers under SC conditions.

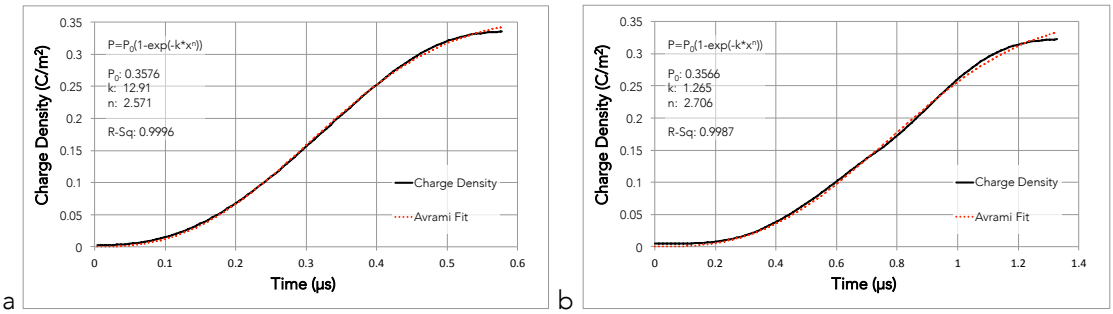

Figure 4.17: Ferroelectric depoling charge density plots with Avrami fit. The front layer (a) was in series with a 6.4 Ω resistance and obtained a maximum electric field of 1.8 kV/mm. The rear layer (b) was in series with a 6.6 Ω resistance and obtained a maximum electric field of 0.86 kV/mm.

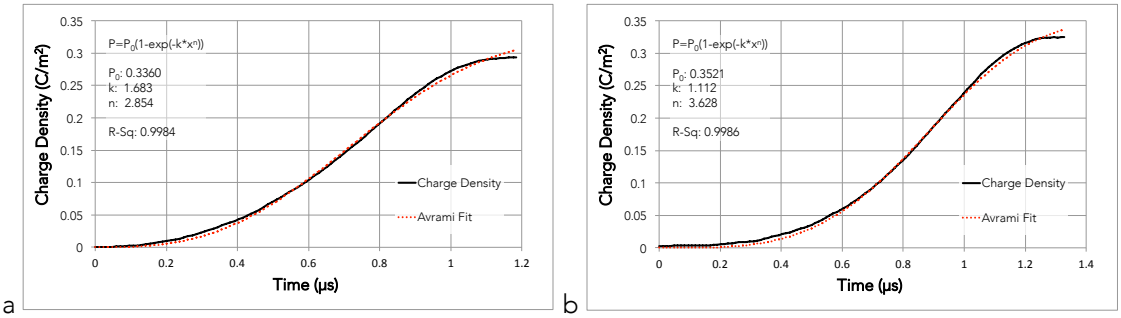

Figure 4.18: Ferroelectric depoling charge density plot for the rear layers with Avrami fit. The rear layer for the 10.3 Ω resistance (a) obtained a maximum electric field of 1.3 kV/mm. The rear layer for the 14.5 Ω resistance (a) obtained a maximum electric field of 2.2 kV/mm.

The resulting Avrami fitting parameters show a dependence on layer position and maximum sustained electric field within the ferroelectric layers during depoling. Figure 4.19a

shows the k fitting parameter, which ranges from 13 – 15 for the front ferroelectric layers, and 1.1 – 1.7 for the rear ferroelectric layers. The difference in k values can either be attributed to a dispersed shock wave front or the polarization orientation. Figure 4.19b shows the exponential fitting parameter n, which is 2.6 for both the front layers, but steadily climbs with increased electric field from 2.4 to 3.6 for the rear layers.

The next question that arises is the effect of the series resistance on depoling kinetics. Under open circuit conditions, the shock propagates into the ferroelectric layer and an electric field develops in the shocked region of the due to domain switching (at lower-pressures) and the shock induced FE-AFE phase transformation (at pressures above the transformation pressure). This electric field exists between the recently freed surface charge on the front electrode and the potential difference across the shock front. The yet-unshocked region of the ferroelectric maintains no net electric field, since the remnant polarization still exactly balances the electric field between the potential difference across the shock front and the bound surface charge on the rear electrode. Under these high field conditions, the strong electric field within the shocked region of the ferroelectric can act to repole the ferroelectric and raise the FE-AFE transformation pressure.[10] Under SC conditions, the released charge on the front electrode is allowed to migrate to the rear electrode to equilibrate the electric potential between the two conductors. The electric field within the shocked region is reduced, while an electric field of opposite polarity develops in the yet-unshocked region. To some extent, this opposite polarity field can act to partially depole the ferroelectric ahead of the shock[26] and lower the FE-AFE transformation pressure.[8-10] Therefore, it is expected that higher series resistances hinder both domain switching and the FE-AFE transformation, while SC conditions are expected to enhance these depoling mechanisms. This analysis should be independent of polarization orientation due to the symmetry of electrostatics, however experimentally this may not be the case.[26,27]

Figure 4.19a shows the k parameter fitting for the front and rear ferroelectric layers as a function of maximum sustained electric field within the layers. The k parameters for the front layers (13 – 15) are much higher than the rear layers (1.1 – 1.7) due to the increased depoling time of the rear layers. This increased depoling time could be attributed to an increase in shock rise time due to wave dispersion as the shock wave front has already scattered off the majority of the composite's interfaces. Likewise, the antiparallel polarization orientation could play a role as seen in Ref. 27, where the depoling current requires significantly more time than the parallel polarization orientation. When comparing the two front ferroelectric layers, the short-circuited layer has a slightly higher k fitting parameter. This is a result of the faster depoling time in the SC layer, since the k parameter describes the length of time over which depoling occurs (4.5 μs for the SC layer, vs. 5.8 μs for the 6.4 Ω layer). The fact that the SC layer depoles faster than the 6.4 Ω layer is in agreement with Ref. 25. However, the overshoot seen in the depoling data for the front layer of the SC experiment may also contribute to the higher k fitting parameter. No significant trend for the k parameter was identified for the rear ferroelectric layers.

Figure 4.19b shows the exponential n fitting parameter as a function of maximum sustained electric field. While the front ferroelectric layers both have a value of 2.6 regardless of the difference of electric field, significant trend emerges for the rear ferroelectric layers. The n values increase gradually from 2.4 to 3.6 with increasing maximum electric field within the ferroelectric layers, suggesting a more abrupt transformation. The lower exponent fitting parameters for the SC and low field data might be explained by the reduced electric field within the shocked region of the ferroelectric in combination with the opposite polarity electric field that develops in the unshocked region. Both the reduction of the field in the shocked region and the presence of the opposite polarity field in the unshocked region reduce the phase transformation pressure.[6,10] Equation 4.1 predicts the higher field layers would require an additional 100 MPa to

initiate the phase transformation, which may account for the more abrupt transformation and higher exponential fitting parameter.

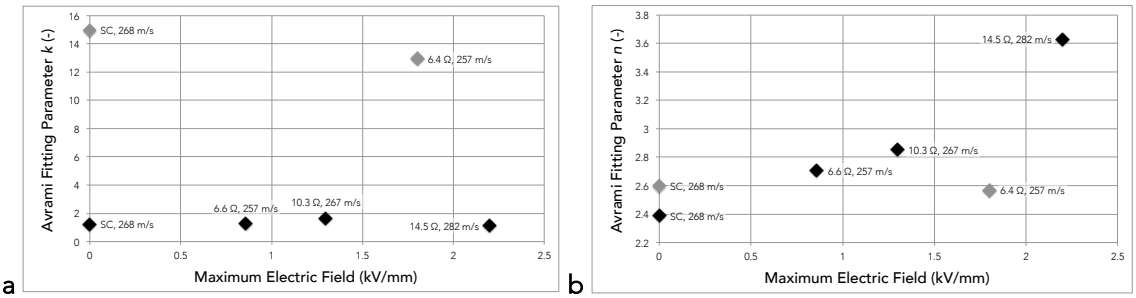

Figure 4.19: Avrami fitting parameters versus the maximum sustained electric field for the lower-pressure experiments. Grey markers are front ferroelectric layers and black markers are rear ferroelectric layers. The k parameter is lower for the rear layers, possibly as a result of an increased rise time in shock front. The n parameter is approximately equal at 2.6 for the front layers, and increases from 2.4 to 3.6 with sustained electric field for the rear layers.

4.6 Results: ALEGRA-FE FE-AFE Module Simulation

To ensure that the simulation agreed with experiment, the free surface particle velocity was compared to that obtained by VISAR for the short-circuited experiments (fig. 4.20). For both simulations, the model under predicts the wave arrival time by ~0.5 μs (fig. 4.20 a & b). This is accounted for by artificially shifting the arrival time for each simulation forward (fig. 20c & d). For the higher-pressure simulation (fig. 4.20c), the shock structure and peak particle velocity match well within the first 2 μs. At times greater than 4.5 μs the velocity histories diverge, most probably due to more complex wave interaction with the sidewall release waves that were not modeled in the simulation. The lower-pressure experiment (fig. 4.20d) matched only in final average free surface velocity.

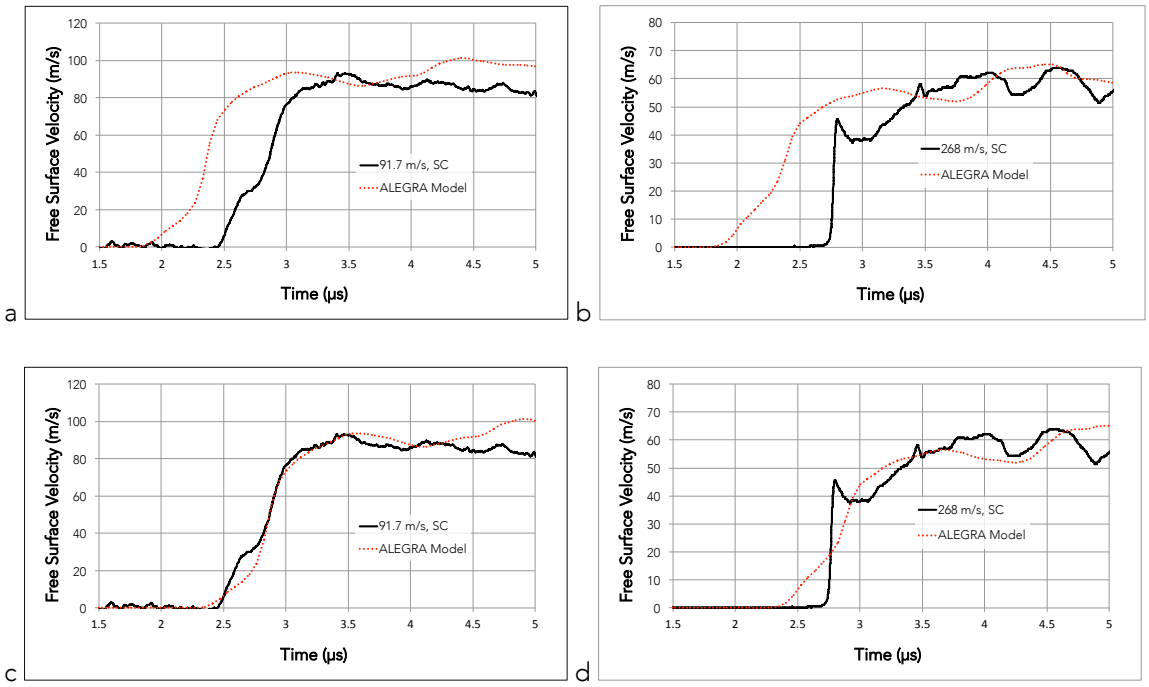

Figure 4.20: Free surface particle velocity histories for the ALEGRA FE-AFE simulations (dashed red line) vs. PDV results for the higher-pressure (a) and lower-pressure (b) SC impact experiments. Both simulations under predict the wave arrival time. By shifting the arrival time forward 0.5 μs, the higher-pressure simulation (c) matches well. For the shifted lower-pressure simulation (d), only the late-time peak velocity matches with experiment.

Figure 4.21 shows the unshifted calculated stress histories for both higher and lower-pressure simulations. The stress history of the front ferroelectric layer shows the shock arriving at 0.5 μs and a rarefaction wave at around 1.7 μs. The stress history of the rear ferroelectric shows the peak stress arriving at 2.4 μs. The calculated peak stress within the ferroelectric layers for the higher-pressure simulation is around 1.5 GPa. The lower-pressure simulation has more variation in the structure of the front ferroelectric layer's stress history. If we ignore the stress overshoot in the shock front and look for the peak stress within the first microsecond of loading, then the peak stress in both ferroelectric layers is around 0.93 GPa.

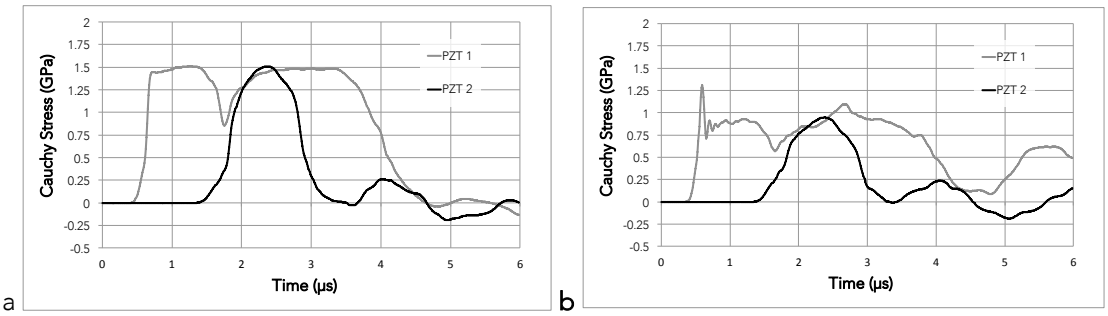

Figure 4.21: Calculated stress histories within the front and rear ferroelectric layers for the higher-pressure (a) and lower-pressure (b) experiments. The front (grey) and rear (black) ferroelectric layers are denoted with labels '1' and '2', respectively.

Since the shifted particle velocity history of the higher-pressure simulation matched well with experiment, the electromechanical histories of the ferroelectric layers were plotted to elucidate the interaction between stress and depolarization (fig. 4.22). The stress in the front ferroelectric layer rises to its maximum value in 260 ns, while the stress in the rear layer requires 850 ns to reach its maximum value. Thus, the shock front is already significantly dispersed by the time it reaches the rear ferroelectric layer. Correspondingly, the charge density is fully released within 80 ns in the front layer, compared to 200 ns for the rear layer.

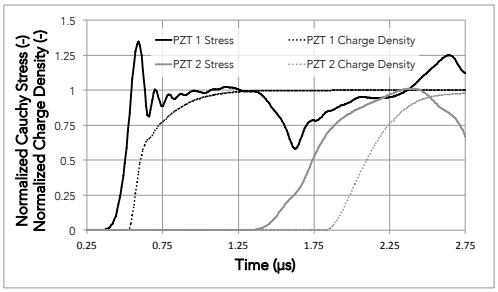

Figure 4.22: Normalized charge density release (dashed) and Cauchy stress (solid) histories within the front and rear ferroelectric layers. The front (grey) and rear (black) layers are denoted with labels '1' and '2', respectively. The rear layer releases its charge slower than the front layer due to an increase in stress wave rise time.

Finally, the effect of layer debonding was modeled by introducing a small (0.1 μm thick, 4 mm diameter) air gap at the location of the Kapton tape. A second tracer was placed 5 mm above the center tracer in order to compare velocity histories (fig. 4.23). The results of the

simulation show that the wave front arrives at the center of the composite approximately 200 ns after arriving at the side. The center wave profile also had a significantly increased rise time compared to the side wave profile.

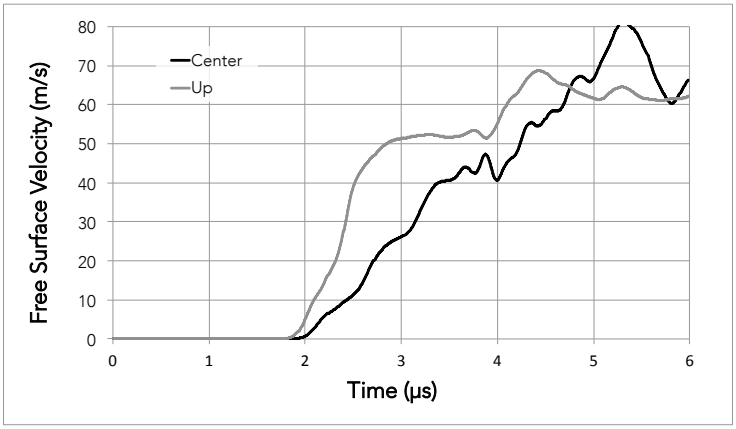

Figure 4.23: Free surface particle velocity histories for the simulated lower-pressure SC experiment assuming a small (0.1 μm thick, 2 mm radius) gap in the center of the composite between the Kapton and third brass layer. The wave travels along the sides of the composite (up) faster than the middle (center) due to the decreased mechanical impedance within the gap.

4.7 Discussion: ALEGRA-FE FE-AFE Module Simulation

The velocity histories computed for the higher and lower-pressure simulations shown in figure 4.20a & b are very similar is structure. Both waves have composite wave velocities around 4.6 km/s, and their shock rise times are around 670 n/s. For both simulations, the velocity peaks at 3 μs and then decays until it rises again around 3.7 μs, reaching a second peak at around 4.4 μs. This velocity dip can be attributed to the shock front reflecting off the low impedance Kapton layer. While the simulations under predicted the shock arrival time by around 0.5 μs, artificially shifting the arrival times resulted in better agreement. For the higher-pressure simulation, the calculated velocity of the first peak (93.4 m/s) was within 1% of the experimental value (92.5 m/s). However the calculated velocity of the second peak (101 m/s) over predicted the experimental velocity (87.1 m/s) by 16%. For the lower-pressure simulation, the calculated velocity of the first

peak (56.5 m/s) under predicted the experimental velocity (62.1 m/s) by 9%. However, the calculated velocity of the second peak (65.1 m/s) was within 2% of experimental value (64.0 m/s).

The particle velocity and stress state within a material are related through the shock jump relations. Since the calculated peak velocities match well with experimental values, the calculated peak stresses should have similar accuracy. Figure 4.21 shows the calculated stress histories within the ferroelectric layers. The peak stress within the layers was 1.5 GPa and 0.93 GPa for the higher and lower-pressure experiments, respectively. The dip in the front layer stress histories around 2.8 μs can be attributed to the wave reflecting off the impedance mismatched Kapton layer. This dip is missing from the rear layer stress history, as it does not see a rarefaction wave from the Kapton layer. The release wave from the composite free surface arrives at the rear layer around 3.5 μs, and later at the front ferroelectric layer around 4.2 μs. The release wave reflects off the Kapton interface as a compressive wave, seen at ~3.8 μs in the rear layer. The Kapton layer and free surface create interfaces with a high impedance mismatch. From the above analysis, it is clear that these interfaces are responsible for a significant portion of the wave scattering within the composite.

The stress and depolarization histories of the ferroelectric layers for the lower-pressure simulation are shown in figure 4.22. Both the stress and released charge density rise times are greater in the rear ferroelectric layer. Since the simulation does not account for effects of polarization orientation on depoling kinetics, we can conclude that the longer depoling times partially results from purely mechanical effects. Both an increased shock rise time and reduced wave speed would result in longer depoling times.

The different wave arrival times seen in figure 4.9a-d are counterintuitive. Ideally, the shock should arrive at the same time across the back of the composite, but the shock fronts recorded in the lower-pressure experiments appear to travel faster along the edges. The

composites were potted in an epoxy with significantly lower impedance than the composite constituents. The shock should then travel slower within the potting epoxy. Furthermore, release waves from the edges of the composite should act to reduce the shock front traveling along the edges, increasing the arrival time. One proposed explanation for this anomalous behavior is possible debonding between the interfaces. The piezoelectric response in shock-compressed piezoelectrics under SC boundary conditions causes the material to contract.[3] The FE-AFE phase transformation also results in a 0.9% volume reduction.[5,9,20] Both phenomena may create internal stresses that act to partially debond the layers and introduce air gaps within the composite. To investigate the effect of air gaps within the composite, the above simulations were altered by taking the center 4 mm diameter of the Kapton layer and replacing it with air. Figure 4.23 shows the particle velocity histories of the resulting simulation taken at two locations on the back surface, along the center (black line) and 5 mm above the center (grey line). The results show that the wave arrives at the center of the composite 200 ns later than compared to the side. This can be attributed to the wave having to travel around the air gap from the sides. The air gap has the additional effect of significantly increasing the rise time of the wave along the center.

4.8 Conclusion

The shock response of a layered composite incorporating ferroelectric layers has been investigated using planar impact experiments and multiphysics shock simulations. The ferroelectric layers were depoled to at least 80% of their remnant polarization values, generating significant pulsed power that propagated ahead of the shock front. The layered composite exhibited a reduced composite wave velocity compared to the predicted wave velocity of its constituents, and wave scattering was evident in the late-time particle velocity profiles. The amplitude of the late-time oscillations, as well as the rise time of the shock front, was found to be

dependent on the impact velocity. The amplitude decreased with increasing impact velocity for the higher-pressure experiments, while it decreased with increasing impact velocity for the lower-pressure experiments. The composite wave velocity and shock rise-time were also found to be dependent on the impact velocity. For the higher-pressure experiments, the wave velocity and rise-time increased with increasing impact velocity, but decreased for the lower pressure experiments. The depoling kinetics of the ferroelectric layers was found to be dependent on the peak electrical field within the layers. When the polarization orientation was anti-parallel to the shock propagation direction, the depoling process occurred more abruptly as a function of increased peak electric field. Simulations predicted the free surface particle velocity reasonably well.

The results of this work show that ferroelectric layers within a smart shock mitigation system can provide pulsed power and propagate this power ahead of the shock front. The composite geometry exhibited wave scattering at the layer interfaces, which can be attributed to the reduced wave speed. Varying the electrical boundary conditions across the ferroelectric layers resulted in altering the depolarization kinetics, but no clear trend could be observed for the shock propagation behavior. While shock propagation in ferroelectric material may be influenced by the electrical boundary conditions, more work is needed in understanding the extent of this behavior before they can be implemented as shock mitigation components.

4.9 References

1. W. Mock and W.H. Holt, "Pulse charging of nanofarad capacitors from the shock depoling of PZT 56/44 and PZT 95/5 ferroelectric ceramics," *J. Appl. Phys.,* vol. 49, no. 12, pp. 5846-5854, Dec. 1978.

2. D. A. Berlincourt, H. H. A. Krueger, and C. Near, "Properties of piezoelectric ceramics," MorganElectro Ceramics, Technical Publication 226, 1999.

3. O. M. Stuetzer, "Secondary stresses in a stress pulse activated piezoelectric element," *J. Appl. Phys*., vol. 38, pp. 3901-3904, May 1967.

4. M. D. Furnish *et al.*, "Dynamic electromechanical characterization of axially poled PZT 95/5," *AIP Conf. Proc.,* vol. 505, pp. 975, Jan. 2000.

5. L. C. Chhabildas, "Dynamic shock studies of PZT 95/5 ferroelectric ceramic," Sandia National Labs., Albuquerque, NM, SAND-84-1729, 1984.

6. J. C. Valadez Perez, "Characterization and modeling of ferroelectric materials for high pressure, high temperature applications," Ph.D. dissertation, Dept. Mech. Aerospace. Eng., Univ. Cal. Los Angeles, Los Angeles, CA, 2013.

7. J. J. Dick and J. E. Vorthman, "Effect of electrical state on mechanical and electrical response of a ferroelectric ceramic PZT 95/5 to impact loading," *J. Appl. Phys.,* vol. 49, pp. 2494, Aug. 1978.

8. L. Chao-Hui *et al.*, "Modeling of PZT ferroelectric ceramic depolarization driven by shock stress," *Chin. Phys. Lett*., vol. 28, pp. 088301, July 2011.

9. R. E. Setchell *et al.*, "The effects of shock stress and field strength on shock-induced depoling of normally poled PZT 95/5," AIP Conf. Proc., vol. 505, no. 1, pp. 979-982, 2000.

10. D. H. Zeuch, S. T. Montgomery, and D. J. Holcomb, "The effects of nonhydrostatic compression and applied electric field on the electromechanical behavior of poled lead zirconate titanate 95/5-2Nb ceramic during the ferroelectric to antiferroelectric polymorphic transformation," Journal of Materials Research, *J. Mater. Res.,* vol. 14, no. 5, pp. 1814-1827, May 1999.

11. D. Jiang *et al.*, "Self-generated electric field suppressing the ferroelectric to antiferroelectric phase transition in ferroelectric ceramics under shock wave compression," *J. Appl. Phys*., vol. 111, pp. 024103, Jan. 2012.

12. S. Zhuang, G, Ravichandran, and D. E. Grady, "An experimental investigation of shock wave propagation in periodically layered composites," *J. Mech. Phys. Solids,* vol. 51, pp. 245-265, 2003.

13. X. Chen, N. Chandra, and A. M. Rajendran, "Analytical solution to the plate impact problem of layered heterogeneous material systems," *Int. J. Solids Struct.*, vol. 41, pp. 4635-4659, April 2004.

14. X. Chen and N. Chandra, "The effect of heterogeneity on plane wave propagation through layered composites," *Compos. Sci. Technol.*, vol. 64, pp. 1477-1493, August 2004.

15. L. Tsai and V. Prakash, "Structure of weak shock waves in 2-D layered material systems," *Int. J. Solids Struct.*, vol. 42, pp. 727-750, August 2004.

16. Vishay Dale. *Power Metal Strip® Resistors, Low Value* [Online]. Available: www.vishay.com/docs/30100/wsl.pdf

17. Vishay Beyschlag. *High Pulse Load Carbon Film MELF Resistors,* [Online]. Available: www.vishay.com/docs/28755/cmb0207.pdf

18. Y. Jiang, *et al.* "Breakdown and critical field evaluation for porous PZT 955 ferroelectric ceramics under shock wave compression," *Smart Mater. Struct.*, vol. 23, no. 8, pp. 085020, July 2014.

19. S. P. Marsh, *LASL Shock Hugoniot Data,* University of California Press, 1980, pp. 658.

20. R. E. Setchell, "Shock wave compression of the ferroelectric ceramic $Pb_{0.99}(Zr_{0.95}Ti_{0.05})_{0.98}Nb_{0.02}O_3$: Hugoniot states and constitutive mechanical properties," *J. Appl. Phys.*, vol. 94, no. 1, pp. 573-588, March 2007.

21. A. C. Robinson *et al.* "ALEGRA: An Arbitrary Lagrangian-Eulerian Multimaterial, Multiphysics Code," in *AIAA Aerospace Science Meeting and Exhibit,* Reno, NV, 2008.

22. L. L. Altgilbers *et al.*, *Explosive Pulsed Power*, World Scientific, 2011.

23. W. S. Hackenberger and E. F. Alberta, "High energy density shock discharge materials," US Patent 8 821 748 B1, Nov. 12 ,2010.

24. P. A. Tipler, *College Physics*, Worth Pub, 1987, pp. 467.

25. M. D. Furnish *et al.*, "Gas gun impact testing of PZT 95/5, part 1: Unpoled state," Sandia National Labs., Albuquerque, NM, SAND-99-1630, 2000.

26. W. Mock Jr. and W. H. Holt, "Axial-current-mode shock depoling of PZT 56/44 ferroelectric ceramic disks," *J. Appl. Phys.*, vol. 50, pp. 2740-48, April 1979.

27. J. T. Cutchen, "Polarity effects and charge liberation in lead zirconate titanate ceramics under high dynamic stress," *J. Appl. Phys.,* vol. 37, no. 13, pp. 4745, Dec. 1966.

28. Y. Yamada *et al.*, "Nucleation, growth, and scaling in a pressure-induced first-order phase transformation: RbI," *Phys. Rev. Lett.*, vol. 53, pp/ 1665, Oct. 1984.

29. J. D. Axe and Y. Yamada, "Scaling relations for grain autocorrelation functions during nucleation and growth," *Phys. Rev. B*, vol. 34, pp. 1599, August 1986.

30. H. J. Jou and M. T. Lusk, "Comparison of Johnson-Mehl-Avrami-Kologoromov kinetics with a phase-field model for microstructural evolution driven by substructure energy," *Phys. Rev. B*, vol. 55, pp. 8114, April 1997.

31. Y. Ishibashi and Y. Takagi, "Note on Ferroelectric Domain Switching," *J. Phys. Soc. Jpn.,* Vol. 31, pp. 506 Dec. 1971.

32. P. Chandra, "Nucleation in the presence of long-range interactions," *Phys. Rev. A*, vol. 39, pp. 3672, April 1989.

33. H. Orihara, S. Hashimoto, and Y. Ishibashi, "A Theory of D-E Hysteresis Loop Based on the Avrami Model," *J. Phys. Soc. Jpn.*, vol. 63, pp. 1031, 1994.

34. D. Ricinschi *et al.*, "Analysis of ferroelectric switching in finite media as a Landau-type phase transition," *J. Phys.: Condens. Matter*, vol. 10, no. 2, pp. 477, 1998.

35. F.L. Cumbrera and F. Sánchez-Bajo, "The use of the JMAYK kinetic equation for the analysis of solid-state reactions: critical considerations and recent interpretations," *Thermochimica Acta,* vol. 266, pp. 315-330, 1995.

5 5. Reactive Multilayer Nanopillars Subjected to Shock Loading

5.1 Introduction

Reactive materials are a relatively new class of material systems currently under investigation for use in increasing the lethality of direct-hit or fragmentation warheads. The ideal material would be stable enough to act as a structural component while surviving handling, launch, and penetration of the target. On the other hand, the material would be sufficiently unstable to reliably ignite on impact. Bimetallic multilayer thin films form an exciting class of reactive materials. These materials can be ignited via a thermal pulse, electrical pulse, laser pulse, or compressive loading. The resulting gasless, self-propagating, high-temperature synthesis transforms the periodically layered bimetal into an intermetallic compound. The reaction can produce enough heat to cause self-propagation of the reaction front, which propagates with a velocity on the order of 0.1-10 m/s. Alternatively, these films may also undergo thermal explosion, where upon all of the constituents undergo a homogeneous, simultaneous reaction. These multilayer films have tunable microstructures that control reaction propagation velocity and temperature. They enjoy good corrosion resistance, high melting temperatures and high strengths of the intermetallic compound. Multilayers of aluminum (Al) and nickel (Ni) have been shown to undergo such a reaction. The temperature in the reaction front can reach 1500 °C, while the propagation velocity has been measured to be ~8 m/s. These multilayers can be sputtered from high quality metal targets. The resulting thin film can be analyzed with a variety of conventional materials characterization tools.

Reactive multilayered thin films have been fabricated using sputter deposition[1] and electron beam evaporation.[2] Sputter deposition has been the preferred method, in part due to the risk of hot particle ignition associated with electron beam evaporation, where particles are emitted from the e-beam evaporators that strike the film and produce a self-sustaining reaction prior to

completion of the film fabrication.[2] Due to the sputtering deposition process, a 0.1-10 nm interlayer of mixed reactants forms, which can reduce the available chemical energy and act as a diffusion barrier.[3] In addition, magnetron sputtering or substrate biasing is used in order control film stress and avoid cracking and delamination.[1]

Previous research has focused on ignition thresholds as a function of film thickness and ignition source. Ignition temperatures due to thermal loading can be as low at 500 K for Al/Ni nanolaminates (heating rate ~40 K/s).[4] Energies as low as 40 mJ has been reported for electric pulse ignition of Al/Ni alloy films, with thermomigration expected to play the dominant role.[7] Optical ignition using laser pulses has shown to be highly dependent on film thicknesses and capping layer.[8] Differences in ignition fluence due to capping layer were attributed to differences in reflectivity. Thinner layer thicknesses tended to lower the ignition fluence, with the exception of thicknesses approaching the interlayer mixing thickness. At such comparable thicknesses, a large percentage of the available chemical energy has been reduced due to mixing, thus increasing ignition fluence. In general, ignition fluence varied by two orders of magnitude for differing material systems. Platinum/aluminum (Pt/Al) films required ~3 J/cm^2, whereas nickel/titanium (Ni/Ti) required 100 J/cm^2. Beam parameters also play an important role in ignition thresholds, where beam spot size, wavelength, and pulse duration all playing a critical role. Post-analysis of dendrite microstructure enabled an estimation of cooling rate and time.[9]

Mechanical ignition has been demonstrated using frictional testers, swinging lever arm devices, and drop tubes.[6,9] Ignition energies ranging from 2.5-8 mJ were recorded for Al/Inconel 600 multilayer films using a drop tube. Recently, experimental[11] and modeling[10-11] efforts have resulted in extending ignition studies into the high strain rate (10^7 – 10^8 /s) regime. Laser-driven shock compression of Al/Ni films was obtained using a special set up incorporating a vacuum gap between the ablation material and the multilayer film in order to separate shock-driven reactions

from that of laser irradiation driven reactions. Direct laser-driven shock compression of Al/Ni films cannot sustain the high strain rates for longer than ~10 ns, and the irradiated surface often suffers from ablation and thermal damage, making post-shock analysis difficult. The applied laser energies (650 -1300 J) generated high strain rates (10^7 – 10^8 /s) and peak pressures of 30-120 GPa. The microlaminates displayed interdiffusion at the shocked surface, but no evidence for a self-propagating reaction, whereas the nanolaminates underwent a complete reaction to the intermetallic compound, which was thought to be a result of both shock loading and a self-propagating reaction. Molecular dynamics (MD) simulations suggest that the microstructure can have unusual effects at such high strain rates, where porous materials undergo higher heat release rates due to increased mechanical mixing via pore collapse. Wave front speeds are expected to be one to two orders of magnitude faster than that of thermally ignited reactions.

Reactive materials have been shown to undergo different reaction and ignition physics at high strain rates. Beyond the elastic regime, material deformation at high strain rates (10^6–10^8 s^{-1}) is fundamentally different from the behavior at conventional rates attained through standard mechanical testing. Understanding material deformation at such high rates is of practical relevance, particularly in applications involving reactive materials, whose characteristic reaction typically occur in the high strain rate regime. Subjecting materials to extreme rates of strain opens the possibilities of exploring new regimes of deformation not seen before. For example, in FCC materials of low stacking fault energy (such as aluminum and nickel), shock compression can greatly influence the twinning-slip transition during plastic deformation at sub-nanosecond time scales.[12]

Most of the current understanding of plastic deformation of metals at high strain rates is based on dislocation models incorporating MD modeling to match experimental results. However, strain rates obtained by split Hopkinson pressure bar experiments are limited to < 10^4 s^{-}

[1], while MD simulation strain rates are typically performed above 10^9 s^{-1}. The dislocation models assume that the dislocations already exist in the material and are initially pinned. It is further assumed that their motion due to the applied strain rate is controlled by two factors, overcoming the energy barrier for unpinning, and the phonon drag associated with dislocation movenment. Many phenomenological models are used to fit shock compression data, all based on dislocation theory (e.g. Johnson–Cook,[13] Zerilli–Armstrong,[14] the mechanical threshold stress (MTS),[15] thermal activation phonon drag,[16] and Steinberg–Lund[17] models).

Under extreme strain rate conditions, the deformation of metals can have significant inconsistencies with the traditional dislocation-barrier models. In metals of low stacking fault energy, the energy differential between twinning deformations and slip dislocation motion is small, and the deformation processes can transition easily.[18] Thin face-centered cubic (FCC) metals can undergo deformation while being free of dislocations.[17,19] This sort of deformation may be utilized to create structures that undergo superplasticity. Possible defect structures associated with dislocation frere deformation in FCC metal samples may include nano-voids and stacking fault tetrahedra.[18,19] Large-scale MD simulations of shocked FCC single crystals[20] that include preexisiting prismatic loop dislocations indicate that the pressure wave activates the homogeneous nucleation of dislocations and results in a high density of dislocations and stacking faults. This results is plastic relaxation behind the shock front,[20] where the dislocation density greatly decreases.

The aformetioned deformation mechanics complicate the layer interdiffusion in multilayered reactive materials under high strain rate compression. The use of flyer plate impact or high explosive detonation to probe the high strain rate regime does not offer detailed information on the role of microstructure. The sustained shock pressure often initiates a self-propagating reaction across the entirety of the sample, making multiphase flow difficult to

analyze.[6] The large compressive stresses supply the activation energy for dislocation depinning and motion throughout the entirety of the sample, activating numerous slip planes at once. It is therefore difficult to assess the role of individual deformation events in ignition when so many are simultaneously active and only the volume average effect can be observed. Additional difficulties arise due to the bulk nature of the material sample in this experimental configuration; pre- and post-shock characterization is rarely ever performed on the same region of the specimen, making any comparison of the microstructure statistical. The above considerations limit the relevance of plate impact and explosive loading.

Previous research on reactive intermetallic multilayers has demonstrated that the reaction may be initiated due to elevated temperatures that arise from high amplitude shock loading.[21] At lower pressures, elevated temperatures may arise from the shear localization due to large plastic flow.[21] These shear-localized areas are thought to act as hot spots, promoting the ignition of the self-propagating reaction. It is expected that the reactive material microstructure plays an important role in hot spot generation under these conditions, however the exact mechanisms are poorly understood. In order to investigate these mechanisms, Al/Ni reactive multilayers were deposited onto copper (Cu) nanopillars and shocked using a laser-driven shock compression system. The single crystal copper substrate efficiently injects dislocations from the pillar into the first layers of the reactive material system. The pillars also act was waveguides for the shock wave, and allow for identification of the same region pre- and post-shock. After shock loading, transmission electron microscopy (TEM) was used to investigate the layer interdiffusion within the reactive material. The finding, while pliminary, indicate that the laser-driven shock wave induces substantial layer interdiffusion while remaining under the threshold of reactive material ignition. Thus, the interdiffusion kinetics under shock loading can be explored on a microstructural level.

5.2 Procedure: Laser-driven Shock Compression Experiments

All of our experiments were carried out using single-crystalline copper (001) pillars in the Laser Spallation Facility, developed previously to measure tensile strengths of interfaces (Yuan and Gupta[22]). The copper pillars (~1.20 μm tall and 0.5 μm in diameter) were prepared out of copper (001) substrates. Pillar dimensions were chosen so that the morphologies of the as-prepared and shock-loaded pillars could be determined using electron and transmission electron microscopy. Four groups of 4 identical pillars were prepared in each corner of the copper substrate using a Nova 600 Dual Beam focused-ion-beam/scanning electron microscope (FIB/SEM) system, which utilizes gallium ions at 0.5 nA current and an accelerating voltage of 30 kV. Each of the four groups was separated from its neighbors by at least 5 mm so that each group of pillars could be independently loaded by the shock wave. This enabled us to carry out multiple tests on the same substrate. Next, multiple layers of nickel and aluminum were deposited via sputter deposition in a 1:1 atomic ratio, verified with energy dispersive x-ray spectroscopy (EDX) (fig. 5.1). The bilayer thickness was chosen to be 50 nm to facilitate a maximum number of layers within the localized nanopillar area, where the number of bilayers ranged from 5 to 8. A 50 nm aluminum layer was deposited between the copper substrate and bilayers. Another 50 nm aluminum layer was deposited after the bilayer deposition as a capping layer. Actual deposited bilayer thicknesses were slightly larger than this due to the nanopillar shape and sputtering process.

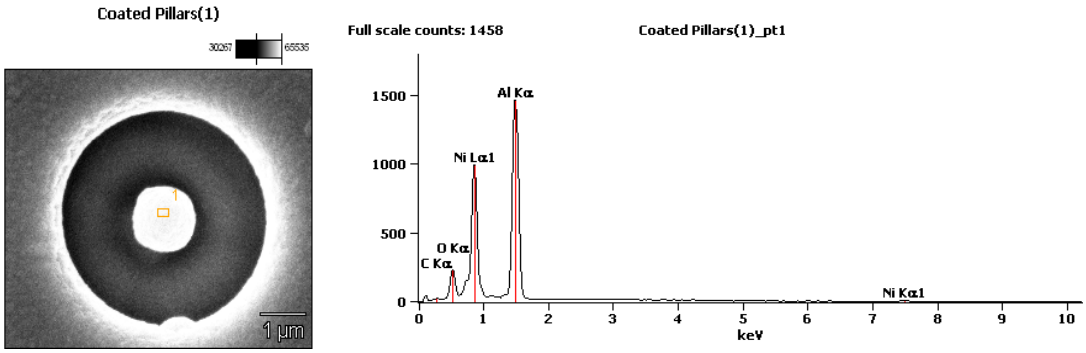

Figure 5.1: EDX of coated nanopillars indicating an atomic ratio of ~1:1 Al:Ni.

In a typical experiment, the copper substrate with multilayer film was sandwiched between a 1-mm-thick glass substrate and a 9-mm-thick brass plate as shown in Figure 5.2. The back surface of the glass substrate was coated with a 0.5-µm-thick, laser absorbing aluminum film, which was constrained from the top by a transparent 20-50 µm thick layer of waterglass. The thicknesses of the aluminum and the waterglass layers were optimized by Yuan *et al.*[23] and Gupta *et al.*[24] to generate stress waves with the fastest rise times (< 1 ns) and short duration so that copper pillars could be loaded under extreme conditions. Brass was chosen to minimize the wave reflection effects and maintain a uniaxial compressive state of stress in the copper nanopillars since it has a low acoustic impedance mismatch with the copper substrate (3.7×10^7 Ns/m^3 for brass vs. 4.1×10^7 Ns/m^3 for copper). Moreover, in order to preserve the deformation caused by the incoming stress wave, the brass plate was made very thick to geometrically disperse the waves and therefore decrease the possibility of any reloading of the pillars by the reflected waves. The glass substrate, copper sample, and the brass plate assembly was mechanically joined and sandwiched between two plexiglass plates and submerged in an oil bath to ensure proper coupling and continuity between all the interfaces so that stress waves could transmit across

them. A window was cut in the plexiglass plate to allow the YAG laser pulse to access the sample. The aforementioned system is shown in figure 5.2.

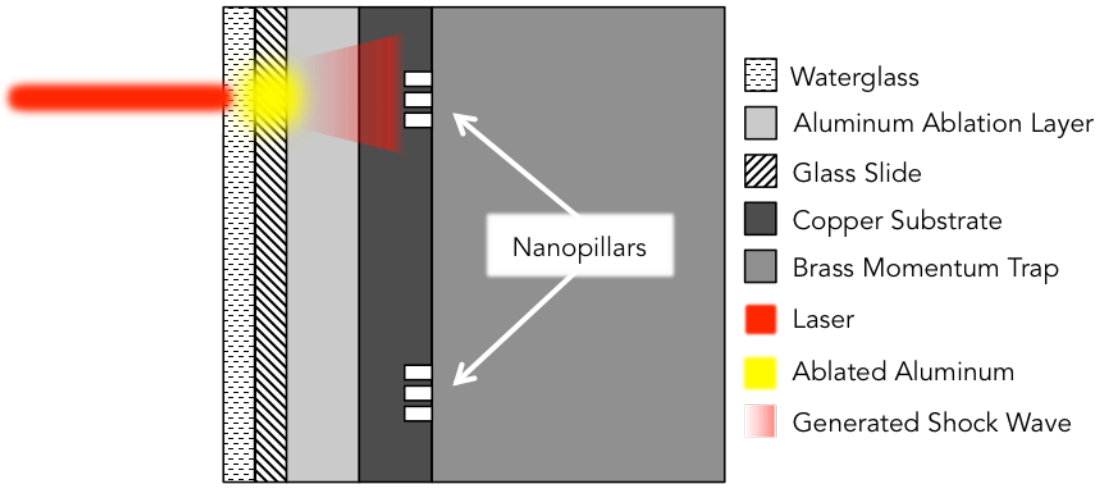

Figure 5.2: Schematic of the laser-driven shock compression experiment. The Nd: YAG laser ablates the aluminum thin film, resulting in a shock wave, which propagates into the copper substrate and nanopillars. The brass momentum trap absorbs the shock wave to decrease reloading of the multilayer reactive film.

The experimental procedure involved focusing a nominal 8 ns long Nd:YAG laser pulse over a 3.8 mm^2 area of the aluminum film. The laser fluence used were 0 (reference), 38, 275, 280, 530, and 560 kJ/m^2. Upon absorption of the laser energy, the aluminum film melts and exfoliates. This process results in the launch of a pressure wave with a 1-2 ns rise-time and 16-20 ns duration towards the sample mounted on the back surface of the substrate.[25-27] Prior to the laser shot, the axis of laser beam was aligned with the center of one of the pillar groups. This configuration allowed for the stress wave to propagate along the axes of each of the nanopillars and transmit into the brass plate. After shock loading, the pillars were imaged with SEM. The pillar wells were then filled with platinum for mechanical support, and then cross section TEM samples were obtained using a FIB. The TEM sample preparation can be seen in figure 5.3.

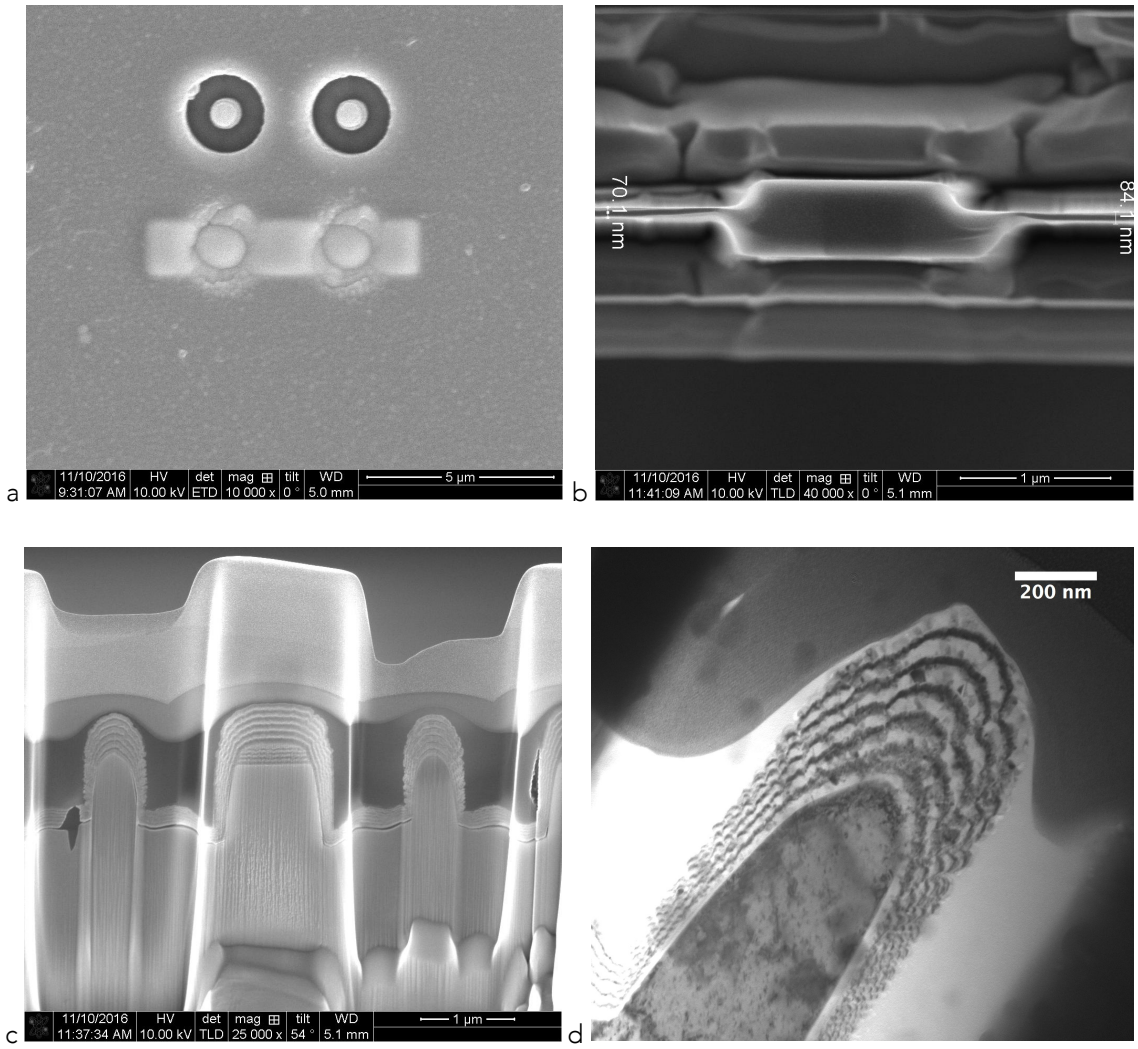

Figure 5.3: TEM sample preparation. Shocked nanopillars are filed with platinum prior to FIB milling for mechanical support (a). FIB milled TEM samples are thinned to be transparent to the TEM electron beam (b). SEM images show conformal deposition of the multilayers around the pillars (c). TEM bright field images show areas of reduced contrast definition, inferring interdiffusion of the multilayers after shock loading (d).

5.3 Results: Laser-driven Shock Compression Experiments

Prior to performing the laser-driven shock compression experiments, reference reactive multilayer nanopillar TEM samples were analyzed. Figure 5.4 shows the plan view SEM images of the group of 4 nanopillars (a). Each nanopillar is uniformly coated with the reactive multilayers and oriented upright, perpendicular from the substrate (b). Figure 5.5 shows the bright field TEM

images for two pillars. The aluminum and nickel layers are clearly defined as the light and dark layers, respectively. The layer interfaces are well defined along the axial portion of the pillar, but becomes less defined along the sides where sputter deposition resulted in decreased uniformity.

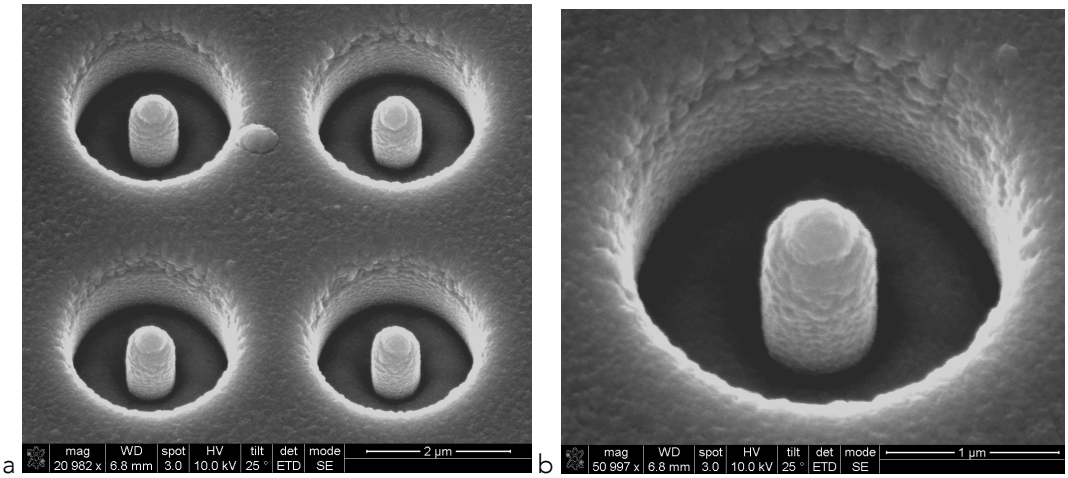

Figure 5.4: Plan view SEM images of the reference nanopillars (a) and magnified view of the upper left pillar (b).

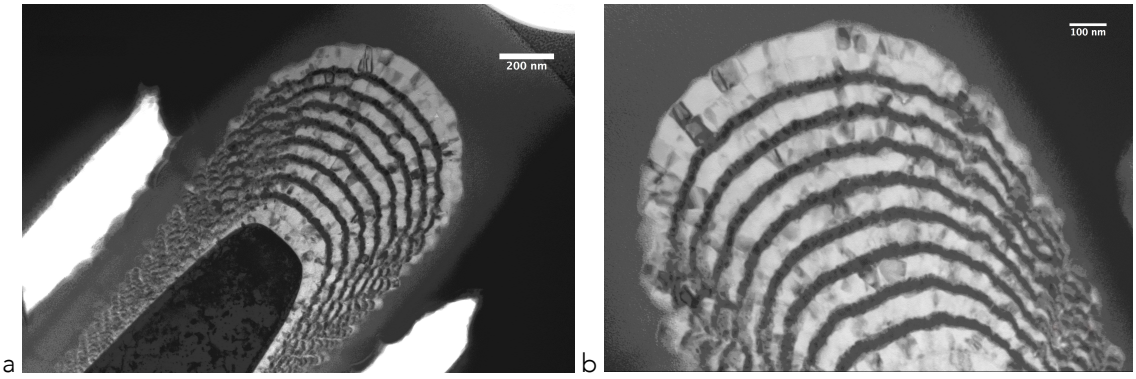

Figure 5.5: Bright field TEM images of the left (a) and right (b) reference nanopillars.

Figure 5.6 shows the selected area electron diffraction (SAED) patterns from the reference nanopillars. The identified rings and intensity match well with literature.[28] Table 5.1 lists the lattice

parameters for aluminum, nickel and the most likely intermetallic formed from interdiffusion, AlNi. Table 5.2 lists the reciprocal lattice spacing for various diffraction rings.

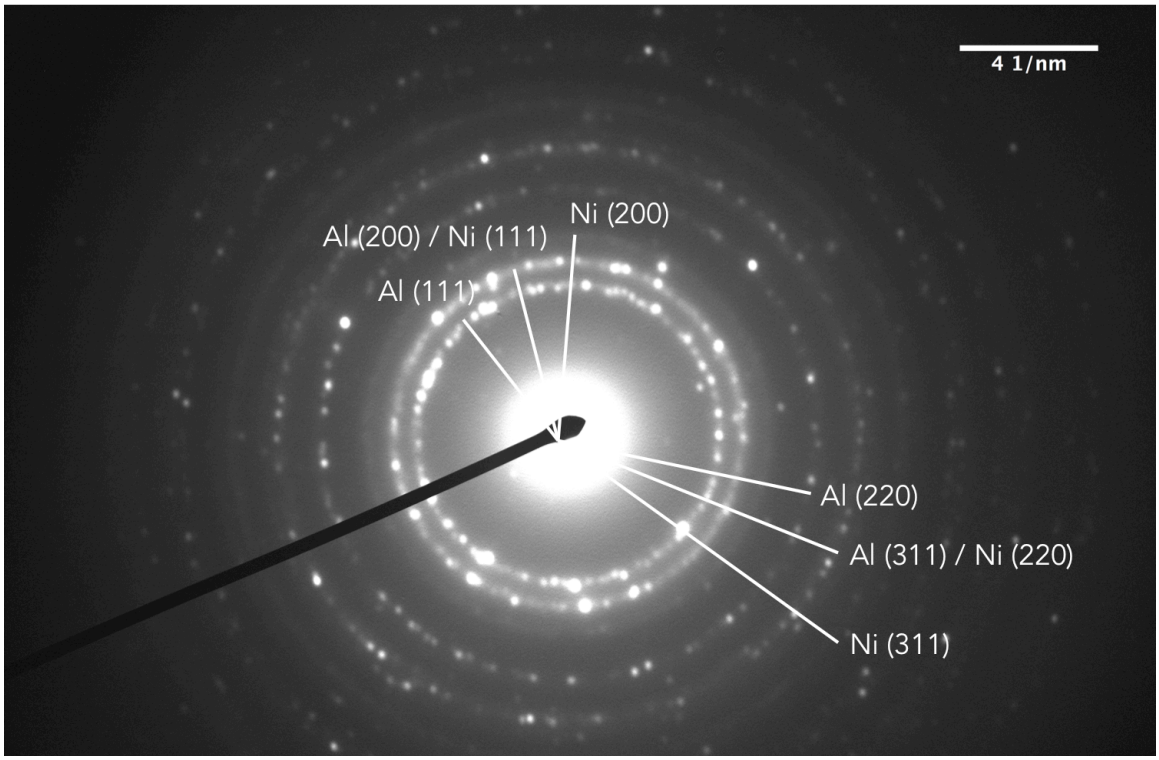

Figure 5.6: SAED patterns for the reference Al/Ni multilayers deposited on copper nanopillars.

Table 5.1: Lattice parameter spacing used in SAED analysis.[29]

Element	Lattice Parameter (Å)
Al	4.048
Ni	3.529
AlNi	2.868

Table 5.2: Reciprocal lattice spacing for various diffraction rings.

Diffraction (FCC)	Al	Ni	Diffraction (SC)	NiAl
(111)	4.28	4.91	(100)	3.49
(200)	4.94	5.67	(110)	4.93
(220)	6.99	8.02	(111)	6.04
(311)	8.19	9.40	(200)	6.97
(222)	8.56	9.82	(210)	7.80

Figure 5.7 shows the SEM plan view images of the four nanopillars (a) and a magnified view of the lower left pillar (b) subjected to shock loading at 38 kJ/m^2 laser fluence. The pillar remains perpendicular to the substrate and no film spallation is evident. Figure 5.8 shows the bright field TEM image (a) and corresponding diffraction pattern (b) for one of the shocked pillars. The two bilayers at the tip of the copper nanopillar were left over from a previous attempt at depositing the reactive multilayers. Initially, the layers were deposited prior to etching the nanopillars, but this resulted in substantial loss of reactive material. Therefore, the reactive multilayers were deposited after the nanopillars were etched. The interface of the layers in figure 8a is not as defined as the reference pillars, suggesting some layer interdiffusion. The diffraction pattern is identical to the reference pillars with the exception of diffraction spots from the copper substrate. The lack of characteristic diffraction patterns from any intermetallic grains could be due to both the low volume of intermetallic and the limits of diffraction resolution in the TEM used.

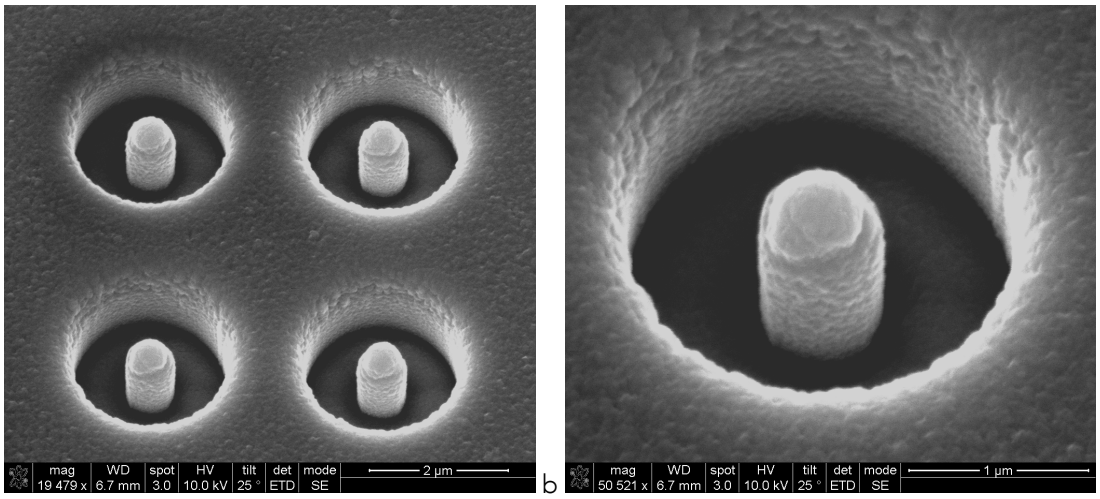

Figure 5.7: Post-shock plan view SEM images of the 4 nanopillars (a) and magnified view of the lower left pillar (b) in the 38 kJ/m^2 experiment.

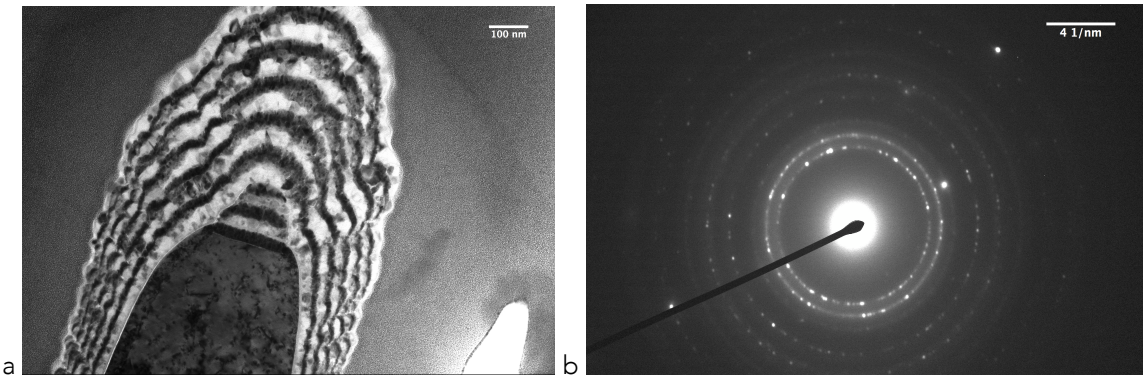

Figure 5.8: Post-shock bright field TEM image (a) and corresponding electron diffraction pattern (b) in the 38 kJ/m^2 experiment.

Figure 5.9 shows the SEM plan view images of the four nanopillars (a) and a magnified view of the lower right pillar (b) subjected to shock loading at 275 kJ/m^2 laser fluence. The pillar suffered damage from debris, however no significant film spallation is evident. Figure 5.10 shows the bright field TEM image (a) and corresponding diffraction pattern (b) for one of the shocked pillars. The interface of the layers in figure 5.10a is as defined as the reference pillars, suggesting that layer interdiffusion did not take place to a significant extent. The diffraction pattern is again identical to the reference pillars.

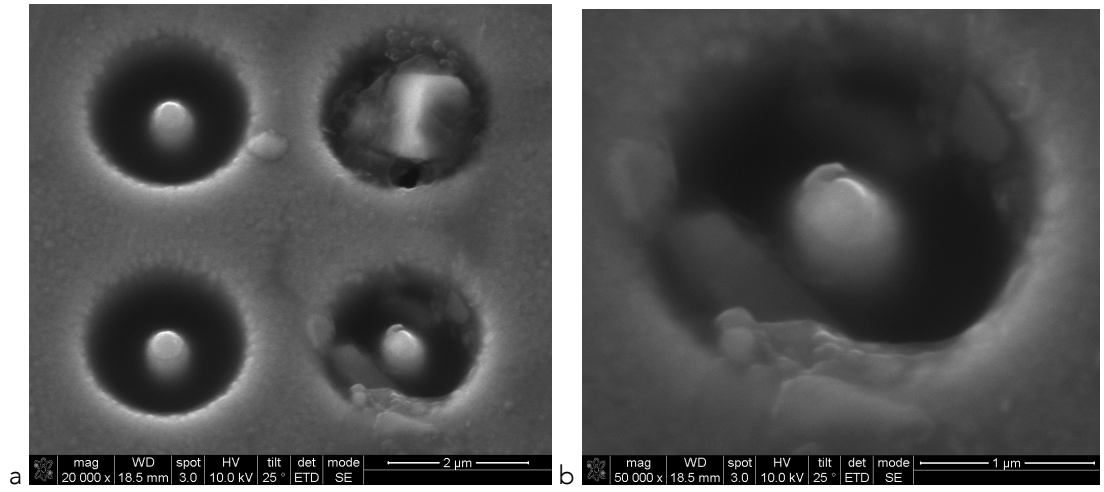

Figure 5.9: Post-shock plan view SEM images of the 4 nanopillars (a) and magnified view of the lower right pillar (b) in the 275 kJ/m^2 experiment.

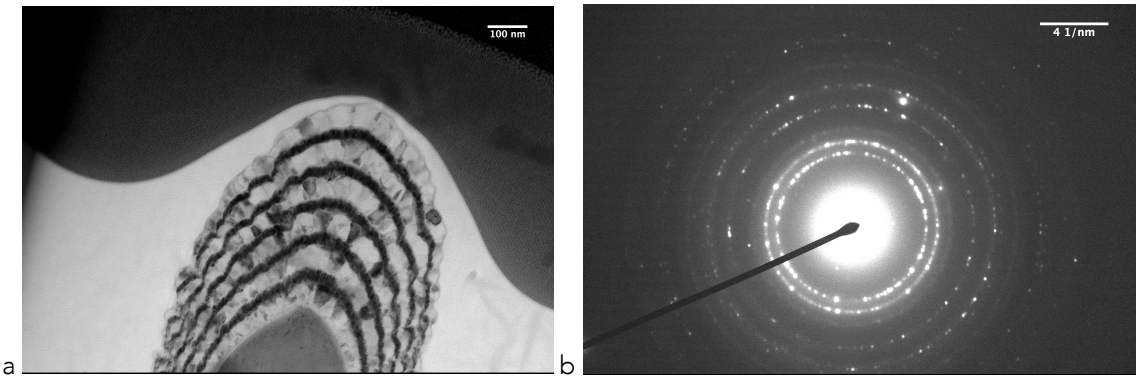

Figure 5.10: Post-shock bright field TEM image (a) and corresponding electron diffraction pattern (b) in the 275 kJ/m^2 experiment.

Figure 5.11 shows the SEM plan view images of the four nanopillars (a) and a magnified view of the lower right pillar (b) subjected to shock loading at 280 kJ/m^2 laser fluence. The pillars are slightly bent, but the reactive film on the pillars and in the wells remains mostly intact. The reactive film away from the pillars is absent due to spallation. Figure 5.12 shows the bright field TEM image of the left (a) and right (b) pillars. Figure 5.13 shows a magnified bright field image (a) and corresponding diffraction pattern (b) for one of the shocked pillars. The interface of the layers in figure 5.13a has significantly decreased in definition, suggesting that substantial layer interdiffusion took place. Despite this, the diffraction pattern is identical to the reference pillars.

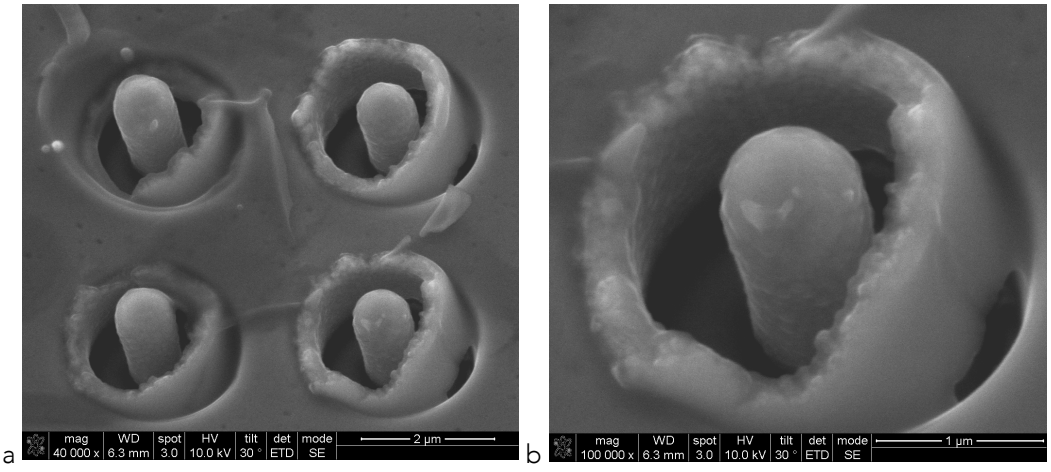

Figure 5.11: Post-shock plan view SEM images of the 4 pillars (a) and magnified view of the lower right pillar (b) in the 280 kJ/m^2 experiment.

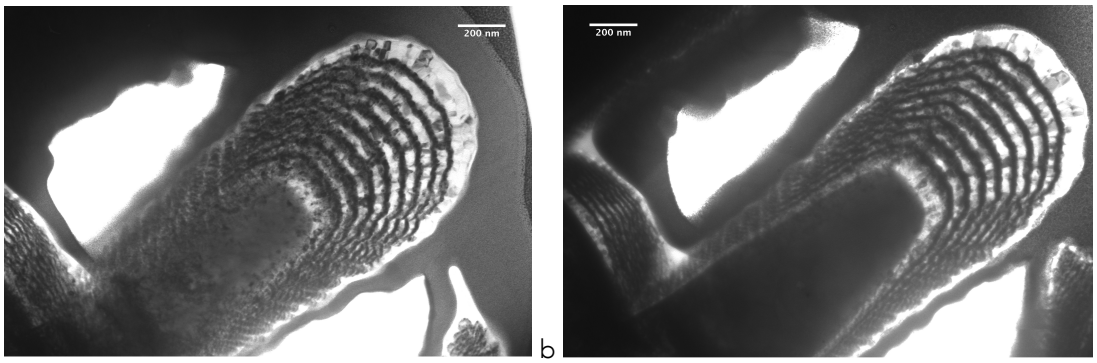

a b

Figure 5.12: Post-shock bright field TEM images of the left (a) and right (b) pillars in the 280 kJ/m^2 experiment.

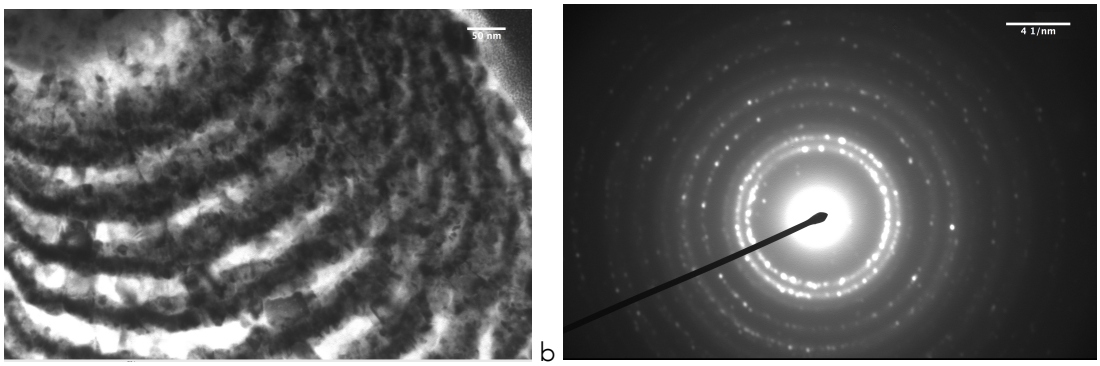

a b

Figure 5.13: Post-shock bright field TEM image (a) and corresponding electron diffraction pattern (b) of the 280 kJ/m^2 experiment.

Figure 5.14 shows the SEM plan view images of the four nanopillars (a) and a magnified view of the lower right pillar (b) subjected to shock loading at 530 kJ/m^2 laser fluence. Again, the pillars are bent, but the reactive film remains intact on the pillars. Some of the film in the wells, as well as the film away from the wells, is absent due to the spallation via the shock wave. Figure 5.15 shows the bright field TEM image of the left (a) and right (b) pillars. Figure 5.16 shows a magnified bright field image (a) and corresponding diffraction pattern (b) for one of the shocked pillars. The interface of the layers in figure 5.16a has some areas of reduced definition, suggesting that layer interdiffusion took place in limited regions. The diffraction pattern is again identical to the reference pillars.

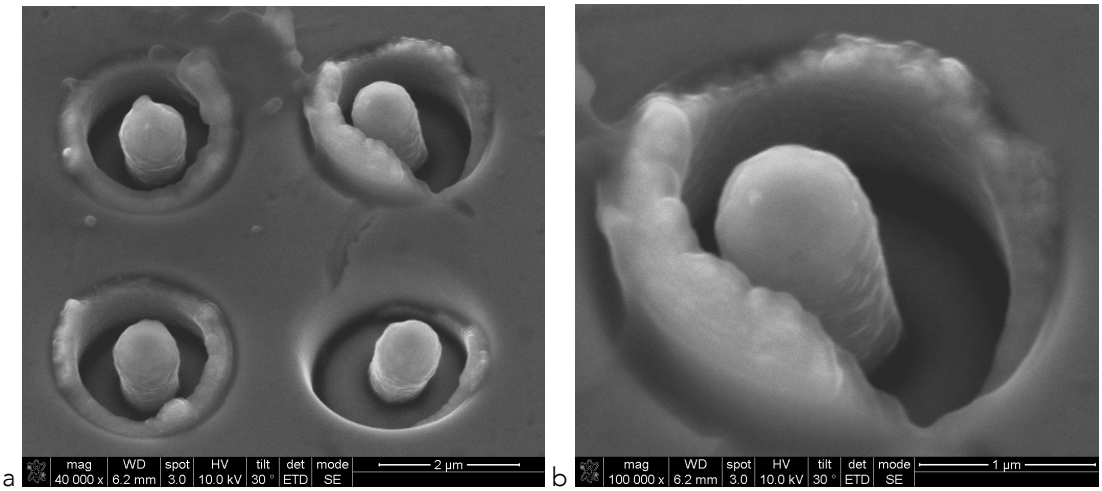

Figure 5.14: Post-shock plan view SEM images of the 4 nanopillars (a) and magnified view of the upper right pillar (b) in the 530 kJ/m^2 experiment.

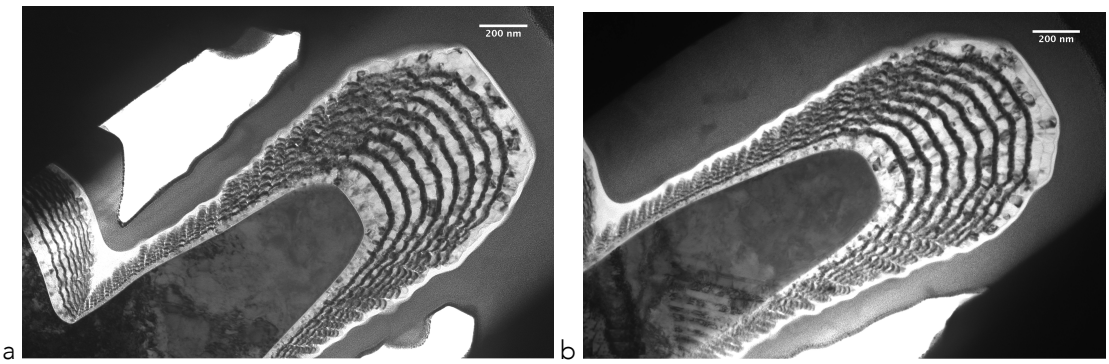

Figure 5.15: Post-shock bright field TEM image of the left (a) and right (b) pillars in the 530 kJ/m^2 experiment.

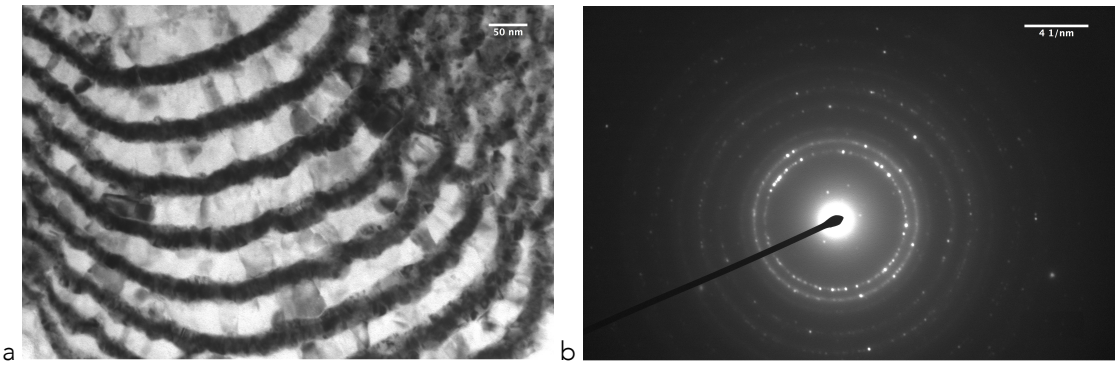

Figure 5.16: Post-shock bright field TEM image (a) and corresponding electron diffraction pattern (b) in the 530 kJ/m^2 experiment.

Figure 5.17 shows the SEM plan view images of the four nanopillars (a & b) subjected to shock loading at 560 kJ/m^2 laser fluence. The images have reduced contrast most probably due to trapped oil in the wells interfering with the electron beam of the SEM. Figure 5.18 shows the bright field TEM image of the left (a) and right (b) pillars. The interfaces are defined except at the tip of the nanopillar where significant interdiffusion appears to have taken place. Figure 5.19 shows a dark field image (a) and corresponding diffraction pattern (b) for one of the shocked pillars. A section of the ring of the Al (200) / Ni (111) diffractions was used, illuminating grains primarily in the aluminum layers. The diffraction pattern is again identical to the reference pillars.

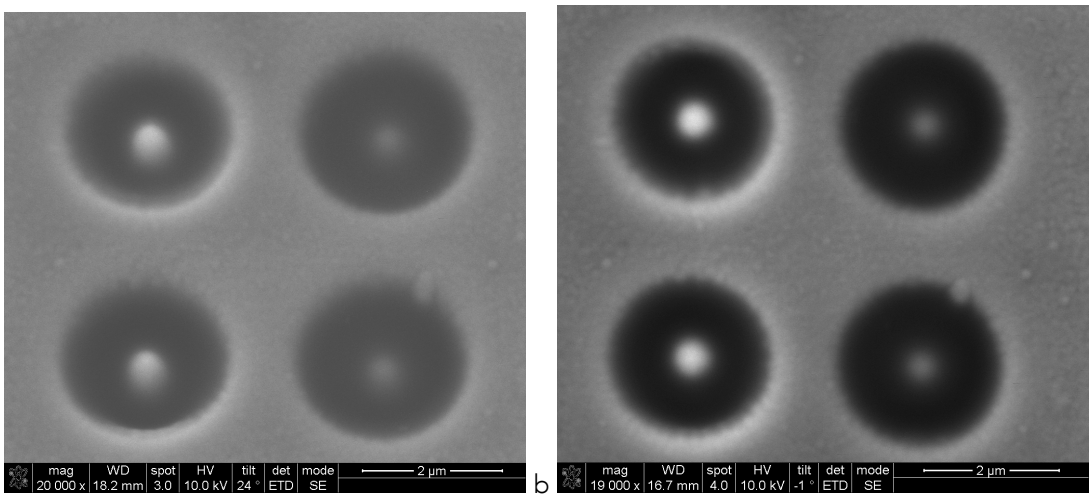

Figure 5.17: Post-shock plan view SEM images of the 4 nanopillars (a & b) in the 560 kJ/m^2 experiment.

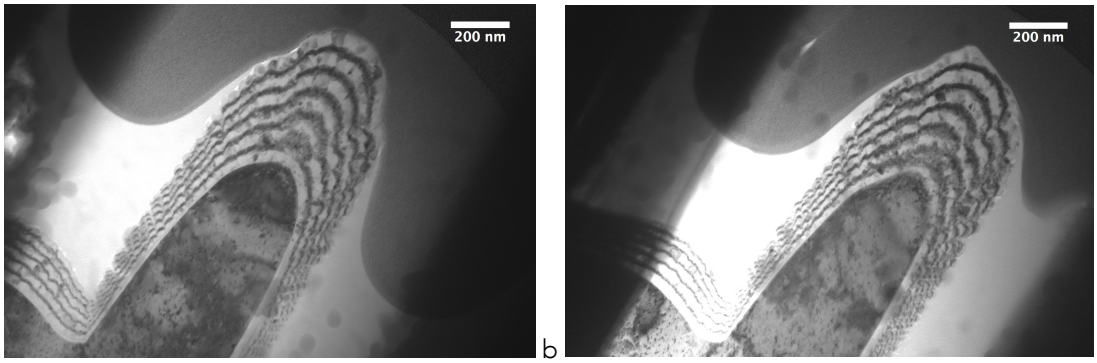

Figure 5.18: Post-shock bright field TEM images of the left (a) and right (b) nanopillars in the 560 kJ/m^2 experiment.

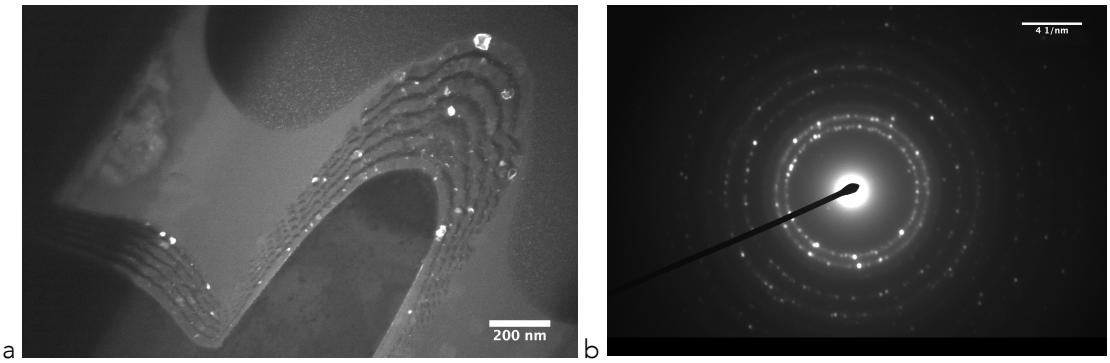

Figure 5.19: Post-shock dark field (Al (200) / Ni (111)) TEM image (a) and corresponding diffraction pattern (b) for the 560 kJ/m^2 experiment.

5.4 Discussion: Laser-driven Shock Compression Experiments

The bright field TEM images exhibit a reduction of definition at the interface between layers for some of the shocked multilayer nanopillars. This reduction of definition has been identified in previous work[30] to correspond with layer interdiffusion. Figure 5.20 shows the bright field TEM images for the unshocked reference pillar (a) and the shocked pillar from the 280 kJ/m^2 experiment (b). The difference in interface definition is substantial, and indicated that layer interdiffusion did take place as a result of shock loading. There does not appear to be a direct relationship between the amount of interdiffusion and laser fluence. This may be due to either an ideal range of shock pressure to induce interdiffusion, or limits in reproducing the shock conditions within the pillars using the laser-driven shock system. Still, significant interdiffusion is seen in the 280 kJ/m^2 experiment, as well as in the 38, 530 and 560 kJ/m^2 experiments, although to a lesser degree.

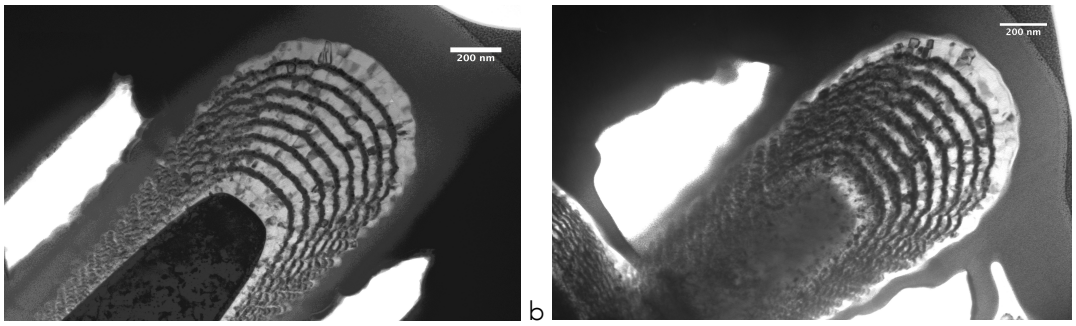

Figure 5.20: TEM bright field image of unshocked (a) and shocked (b) multilayer nanopillars. Laser fluence of 280 kJ/m^2 resulted in a marked change in contrast between layers, inferring layer interdiffusion.

The SAED patterns were identical in each of the experiments. Figure 5.21 shows the diffraction patterns for the unshocked reference pillar (a) and the shocked pillar from the 280 kJ/m^2 experiment (b). The only discernable difference is a slight increase in the width of the Al (311) / Ni (220) ring, which could be a result of the Al (222) or AlNi (112) diffraction rings. The issue with using diffraction patterns for identification of the intermetallic results from the lack of resolution of the TEM. The minimum selected area aperture in the TEM encompasses the majority of the multilayers on the nanopillar structure, and most of the diffraction pattern would have resulted from the unreacted volume. Furthermore, the resulting intermetallic has diffraction pattern peaks that coincide with the constituent metals' peaks, making identification of the intermetallic difficult with the unreacted volume present. Figure 5.22 shows the bright field (a) and dark field (b) TEM images for the 38 kJ/m^2 experiment, where the dark fiend images utilizes the Al (200) / Ni (111) ring. This is also the location of the most prominent diffraction peak from the AlNi intermetallic, namely the (110) diffraction peak. Therefore, the resulting illuminated grains could be the intermetallic or any of the parent metals. For this reason, dark field TEM analysis also lacks the resolution to separate intermetallic grains from the constituent metals.

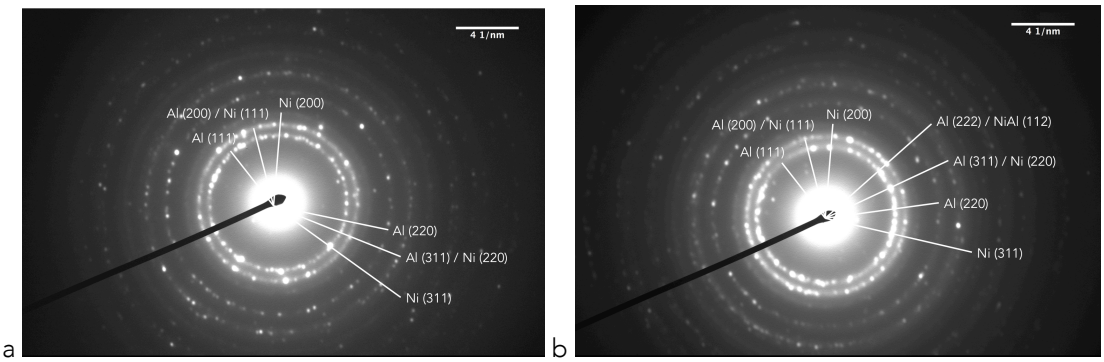

Figure 5.21: TEM diffraction patterns for the unshocked (a) and shocked (b) multilayer nanopillars. The width of the fifth ring slightly increases, possibly due to the appearance of the AlNi (112) diffraction.

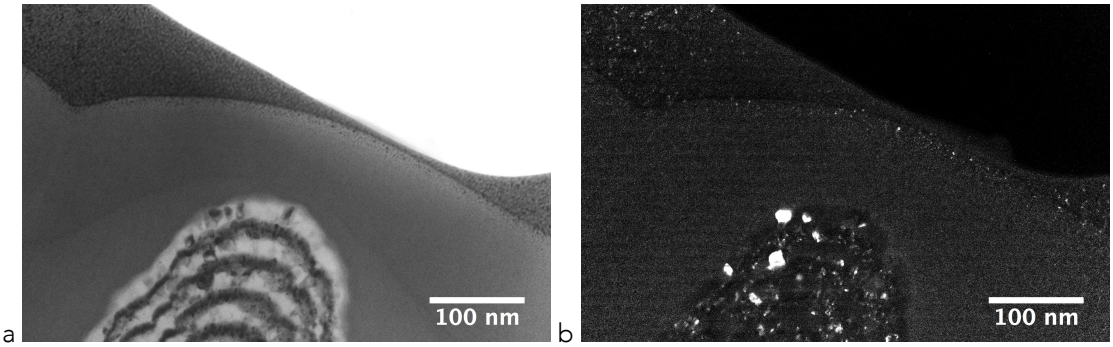

Figure 5.22: Post-shock bright field image (a) and dark field (Al (200), Ni (111)) TEM image (b) of the 38 kJ/m^2 experiment.

The inability to identify intermetallic compounds within the shocked nanopillars can be overcome a number of ways. By utilizing high resolution TEM, individual grains can be targeted for SAED. Furthermore, the resulting diffraction pattern would have higher resolution, and identification of characteristic diffraction rings could be achieved. Another interesting technique would be utilizing a scanning tunneling electron microscope to identify the concentration of constituent metals across each interface. In either case, mechanisms to quantify the amount of layer interdiffusion exist, and can be utilized to understand the role of laser fluence and geometric considerations on layer interdiffusion.

5.5 Conclusion

Reactive multilayers of Al/Ni were deposited on copper nanopillars and shock loaded utilizing a laser-driven shock compression system. The resulting structures were analyzed using SEM and TEM. The SEM images exhibited substantial structural deformations, while the TEM images exhibited characteristics of layer interdiffusion. The SAED patterns lacked the resolution to quantify the amount of layer interdiffusion or to identify the resulting intermetallic compounds, however it is expected that these limitations can be overcome using a high resolution TEM and/or a scanning tunneling electron microscope. Regardless, this system has demonstrated the ability to shock load reactive materials at a high throughput while allowing for the characterization of the resulting microstructure using advanced microscopy techniques. This system should be useful in investigating other reactive multilayer material combinations, and possibly other reactive materials such as nanothermites.

5.6 References

1. A.J. Gavens *et al.*, "Effect of interdiffusion on self-propagating exothermic reactions in Al/Ni nanolaminate foils," *J. Appl. Phys.*, vol. 87 pp.1255, 2000.

2. J.A. Floro, "Propagation of explosive crystallization in thin Rh–Si multilayer films," *J. Vac. Sci. Technol. A*, vol. 4, pp. 631, 1986.

3. M. Petrantoni *et al.*, "Asymmetric diffusion as a key mechanism in Ni/Al energetic multilayer processing: a first principles study," *J. Vac. Sci. Technol. A*, vol. 28, pp. L15, 2010.

4. K.V. Manukyan *et al.*, "Tailored reactivity of Ni + Al nanocomposites: micro-structural correlations," *J. Phys. Chem. C*, vol. 116, pp. 21027, 2012.

5. A.E. Gash, T.W. Barbee Jr., and O. Cervantes, "Stab sensitivity of energetic nanolaminates," *Proc. 33rd International Pyrotech. Sem,* ISBN: 0975527428, 2006, p. 59.

6. Y.N. Picard *et al.*, "Pulsed laser ignition of reactive multilayer films," *Appl. Phys. Lett.*, vol. 88, pp. 144102, 2006.

7. Y.N. Picard *et al.*, "Nanosecond laser induced ignition thresholds and reaction velocities of energetic bimetallic nanolaminates," *Appl. Phys. Lett.*, vol. 103, pp. 104103, 2008.

8. G.M. Fritz *et al.* "Thresholds for igniting exothermic reactions in Al/Ni multilayers using pulses of electrical, mechanical, and thermal energy," *J. Appl. Phys.*, vol. 113, pp. 014901, 2013.

9. C.T. Wei *et al.*, "Response of Ni/Al laminates to laser-driven compression," *Acta Mater.*, vol. 60 pp. 3929, 2012.

10. S. Zhao, T.C. Germann, and A. Strachan, "Atomistic simulations of shock-induced alloying reactions in Ni/Al nanolaminates," *J. Chem. Phys.*, vol. 125 pp. 164707, 2006.

11. S. Zhao, T.C. Germann, and A. Strachan, "Molecular dynamics simulation of dynamical response of perfect and porous Ni/Al nanolaminates under shock loading," *Phys. Rev. B*, vol. 76, pp. 014103, 2007.

12. B. A. Remington *et. al.*, "Material dynamics under extreme conditions of pressure and strain rate." *Mat. Sci. and Tech.*, vol. 22, pp. 474-488, 2006.

13. G.R. Johnson *et al.*, "Response of various metals to large torsional strains over a large range of strain rates - Part 1: Ductile metals, Part 2: Less ductile metals," *ASME J. Eng. Mater. Tech.*, vol. 105, pp. 42, 1983.

14. E. M. Bringa *et al.*, "Ultrahigh strength in nanocrystalline materials under shock loading," *Science*, vol. 309, pp. 1838, 2005.

15. P. S. Follansbee and U. F. Kocks, "A constitutive description of the deformation of copper based on the use of the mechanical threshold stress as an internal state variable," *Acta Metall.*, vol. 36, pp. 81, 1988.

16. F. J. Zerilli and R. W. Armstrong, "The effect of dislocation drag on the stress-strain behavior of F.C.C. metals," *Acta Metall. Mater.*, vol. 40, pp. 1803, 1992.

17. M. Kiritani *et al.*, "Plastic deformation of thin metal foils without dislocations and formation of point defects and point defect clusters," *Proc. MRS, Sym. P*, vol. 673, pp. P71.1, Jan. 2001.

18. L. Li and N. M. Ghoniem, "Twin-size effects on the deformation of nanotwinned copper," *Phys. Rev. B, Condens. Matter*, vol. 79, pp. 075444, Feb. 2009.

19. M. Kiritani, "Analysis of high-speed-deformation-induced defect structures using heterogeneity parameter of dislocation distribution," *Mat. Sci. Eng.*, vol. 350, pp. 63-69, 2003.

20. Eduardo M. Bringa, Alfredo Caro, Yinmin Wang Maximo Victoria, James M. McNaney, Bruce A. Remington, Raymond F. Smith, Ben R. Torralva, and Helena Van Swygenhoven, "Ultrahigh Strength in Nanocrystalline Materials Under Shock Loading," Science, 2005, 309, p. 1838.

21. P. H. Chiu, K. L. Olney, A. Higgins, M. Serge, D. J. Benson and V. F. Nesterenko, Appl. Phys. Lett., 102 (2013) 241912

22. V. Gupta, J. Yuan, A. Pronin, "Recent developments in the laser spallation technique to measure the interface strength and its relationship to interface toughness with applications to metal/ceramic, ceramic/ceramic and ceramic/polymer interfaces," Journal of Adhesion Science and Technology, 1994, 8 (6), p. 713

23. J. Yuan, V. Gupta, and A. Pronin, "Measurement of interface strength by the modified laser spallation technique. III. Experimental optimization of the stress pulse," *J. Appl. Phys.* vol. 74 pp. 2405–2410, 1993.

24. V. Gupta, J. Yuan, and A. N. Pronin, "Nanosecond rise-time laser-produced stress pulses with no asymptotic decay," *Rev. Sci. Instr.*, vol. 64, pp. 1611-14, 1993.

25. G. Youssef and V. Gupta, "Dynamic response of polyurea subjected to nanosecond rise-time stress waves," *Mech. Time-Depend. Mater.*, vol. 16, pp. 1-12, 2011.

26. G. Youssef and V. Gupta, "Dynamic tensile strength of polyuria," *J. Mater. Res.*, vol. 27, pp. 494-499, 2012.

27. G. Youssef, C. Moulet, M. S. Goorsky, and V. Gupta, "Inter-wafer bonding strength characterization by laser-induced shock waves," *J. Appl. Phys.*, vol. 111, pp. 094902, 2012.

28. J. S. Kim *et al.*, "Imaging of transient structures using nanosecond in situ TEM," *Science,* vol. 321, no. 5895, pp. 1472-75, Sept. 2008.

29. Y. Zhou *et al.*, "First-principles studies of Al–Ni intermetallic compounds," *J. Solid State Chem.*, vol. 187, pp. 211-218, March 2012.

30. A. S. Rogachev *et al.*, "Structure evolution and reaction mechanism in the Ni/Al reactive multilayer nanofoils," *Acta Materialia*, vol. 66, pp. 86-96, March 2014.

6 Summary

Incorporating active materials such as ferroelectric ceramics into shock mitigation systems can provide additional functionality not available to passive systems. This dissertation explores some of these possibilities. Chapter 2 presented the computational results demonstrating how the piezoelectric effect can transfer energy out of the shock wave and propagate it ahead of the front in order to modify the stress and momentum state of the material prior to the shock arriving. The mechanism involved the following processes:

1) The compressive shock stress induces an electric field within the shocked region of the ferroelectric due to the direct piezoelectric effect.
2) An electrical shunt allows the potential between the front and rear electrodes to equilibrate, resulting in an opposite polarity electric field within the yet-unshocked region of the ferroelectric.
3) The opposite polarity field in the yet-unshocked region of the ferroelectric induces a state of tensile stress due to the converse piezoelectric effect.

An expression for the percentage of tensile stress generated ahead of the shock relative to the initial compressive stress was derived and compared to the simulation results, both suggesting a value greater than 20%. The simulations demonstrated that this effect could be tuned using various load resistances in series with the ferroelectric circuit. By modeling time-dependent varistors, the simulation demonstrated how this effect could be switched on or off mid shock transit. Spatially varying the electrical boundary conditions across a ferroelectric plate produced a spatially varying stress profile. If the back of the shunted ferroelectric was left unconstrained, the tensile stress would relax via contraction, imparting a negative particle

velocity within the yet-unshocked region of the ferroelectric. The electrical boundary conditions also influenced the shock wave structure in an impedance-mismatched, ferroelectric composite by attenuating the wave scattering and delaying the shock front arrival. Finally, a discussion on limiting material properties was given.

The results presented in Chapter 2 illustrate how the electrical boundary conditions can alter the shock response of ferroelectric via the piezoelectric effect. While this effect was limited to the piezoelectric regime in the simulations, the same mechanism would be present in ferroelectrics that undergo mechanical depolarization, where the released charge would still result in a tensile stress state ahead of the shock front. Alternatively, by flipping the polarization of the latter half of the piezoelectric, a compressive stress can be generated ahead of the shock front. In either can, mechanical energy is transferred out of the shock and transferred ahead via the piezoelectric effect, spreading the shock front. Currently, the strength of the ferroelectric material limits the amount of tensile stress it would be capable of producing. However, with advances in ferroelectric material systems, these effects may one day be a substantial enough to find use in practical applications. For example, wave-shaping using an array of ferroelectric elements may find use in shock experiments. Altering the wave profile by utilizing ferroelectric composites could enable tailoring incoming waves, or even disperse and attenuate it completely. Careful experimental research is needed to validate these results.

Chapter 3 presented the mechanical loading rate dependence on depolarization for PZT 52/48 and PZT 95/5. Within the loading rate range of 0.1-100 MPa/ms, neither composition exhibited a strong rate dependence of depolarization. One noticeable difference between the compositions was the pressure at which the released charge density saturated. The released charge density for PZT 52/48 saturated at ~500 GPa, while PZT 95/5 required twice the pressure for the saturation of polarization. Within the loading range of 7.2 to 92.5 MPa/μs, PZT 52/48

showed significant rate sensitivity, while PZT 95/5 was relatively rate insensitive. There was, however, a jump in depolarization stress within the PZT 95/5 composition for loading rates above 50–60MPa/μs.

The results presented in Chapter 3 illustrate the importance of material selection when designing shock experiments. For plate impact experiments, the impact velocity is notoriously difficult to reproduce shot-by-shot. This introduces a spread in impact velocity and thus loading rate. For rate-sensitive materials, the depoling currents are dependent on not only the electrical boundary conditions, but also the loading rate. The two effects may become difficult to separate without statistical analysis, which could require a prohibitive amount of plate impact experiments.

Chapter 4 presented the experimental and computational results of the electromechanical response of ferroelectric composites subjected to shock loading via plate impact. Two pressure regimes were explored (1.4 & 0.9 GPa) while varying the electrical boundary conditions across the ferroelectric layers. The composites produced electrical energy that was transferred ahead of the shock front to the current viewing resistors, and the depoling currents recorded. The velocity profiles exhibited a late-time oscillatory structure that is indicative of wave scattering within the composite. The composite wave speed was found to be lower than that predicted for the individual constituents.

The free surface particle velocity histories obtained by VISAR and PDV exhibited varying arrival times, shock font rise times, composite wave speeds, and late-time profiles. The composite wave speed and rise time appeared to increase with increasing impact velocity for the higher-pressure (1.4 GPa) experiments and decrease with increasing impact velocity for the lower-pressure (0.9 GPa) experiments. The relative amplitude of the late-time velocity oscillations was obtained by using fast Fourier Transforms, and appeared to decrease with increasing impact velocity for the higher-pressure (1.4 GPa) experiments and increase with increasing impact

velocity for the lower-pressure (0.9 GPa) experiments. The difference in trends between the higher- and lower-pressure experiments may be partly explained by the difference in impactor material (brass for the higher-pressure and PMMA for the lower pressure experiments). The PMMA impactor results in an additional impedance-mismatched interface that would increase the amount of scattering events.

The released charge density from the shock compressed ferroelectric layers was computed by integrating the depoling currents over time and dividing by the electrode area. The final charge density values indicated that each of the ferroelectric layers released at least 80% of their remnant polarization, with the exception of the two layers that suffered electrical breakdown. Some of the charge density plots suffered from an overshoot, most likely caused by stray inductance. The other plots were fit to the Avrami equation and the fitting parameters were found to be dependent on the peak electric field within the layers. Contrary to the results of Chapter II, no relation between the shock response and the electrical boundary conditions could be found. It is assumed that the mechanical effects of the shock response surpass the mechanical effects due to piezoelectricity within this pressure regime.

The ALEGRA-FE simulation utilized the nonlinear ferroelectric-antiferroelectric material module, and the results provided insight into the stress state within the ferroelectric layers as well as the sources of some of the wave reflections. The highly impedance-mismatched brass/Kapton and brass/air interfaces resulted in large rarefaction and compression waves that propagated within the composite, while the smaller impedance mismatch of the ferroelectric/brass interfaces resulted in smaller wave reflections. The simulations also examined the effect of a small air gap within the composite and found that such a gap reduces the wave arrival time and increases the front rise time. It was suggested that this might be a partial reason for the varied shock arrival times seen in both the higher-pressure and lower-pressure experiments. If the secondary tensile

stresses produced by the converse piezoelectric effect discussed in Chapter II were present in the layers, they may have caused partial debonding in the layers resulting in air such gaps.

The results presented in Chapter 4 suggest that the impact velocity influence the mechanical response of the ferroelectric composites more than the electrical boundary conditions, while the electrical boundary conditions influence the electrical response more than the impact velocities. Future work would benefit from impact experiments with highly repeatable impact velocities, in order to elucidate what effects, if any, the electrical boundary conditions have on the shock response. The ferroelectric layers excelled at producing electrical energy that could be used for subsequent layers in shock mitigating systems. Layers of reactive or energetic materials could be incorporated after the ferroelectric layer. These thin energetic layers could be detonated by the electrical energy in order to rapidly create highly impedance-mismatched gas/solid interfaces, which may scatter the shock front more efficiently.

Chapter 5 introduced initial research performed on a novel high throughput materials characterization system designed to study the microstructure of shock loaded reactive materials. Al/Ni multilayer reactive materials were deposited on top of copper nanopillars and shock loaded with a laser-driven shock compression system. The resulting structure was analyzed using SEM and TEM to study the layer interdiffusion driven by the shock loading of the nanopillars. The results indicated that the laser system can drive layer interdiffusion while remaining below the threshold for ignition. The post-shock characterization would benefit from utilizing high resolution TEM and/or scanning tunneling microscopy. Multiple reactive multilayer combinations can be deposited and their microstructural changes under shock loading examined with high throughput and low experimental cost.